UNIVERSIDADE DE SÃO PAULO
Escola de Engenharia de São Carlos

The fracture failure modelling of three-dimensional structures composed of quasi-brittle materials subjected to different loading velocities rates by the dipole-based BEM approach and Bayes updating

Representação da falha por fratura de estruturas tridimensionais compostas por materiais quase frágeis submetidas a diferentes taxas de velocidade de carregamento pela abordagem do MEC dipolos e atualização Bayesiana

Luís Philipe Ribeiro Almeida

PhD Thesis - Postgraduate Program in Civil Engineering (Structural Engineering) at the São Carlos School of Engineering, University of São Paulo

EESC · USP

Luís Philipe Ribeiro Almeida

The fracture failure modelling of three-dimensional structures composed of quasi-brittle materials subjected to different loading velocities rates by the dipole-based BEM approach and Bayes updating

Representação da falha por fratura de estruturas tridimensionais compostas por materiais quase frágeis submetidas a diferentes taxas de velocidade de carregamento pela abordagem do MEC dipolos e atualização Bayesiana

CORRECTED VERSION

(The original version is available at São Carlos School of Engineering)

PhD Thesis presented to the Graduate Program in Structural Engineering at the São Carlos School of Engineering, University of São Paulo, Brazil to obtain the degree of Doctor of Science.

Concentration Area: Structural Engineering

Supervisor: Prof. Dr. Edson Denner Leonel

São Carlos

2025

Ficha catalográfica elaborada pela Biblioteca Prof. Dr. Sérgio Rodrigues Fontes da EESC/USP com os dados inseridos pelo(a) autor(a).

Almeida, Luís Philipe Ribeiro
At The fracture failure modelling of three-dimensional structures composed of quasi-brittle materials subjected to different loading velocities rates by the dipole-based BEM approach and Bayes updating / Luís Philipe Ribeiro Almeida; orientador Edson Denner Leonel. São Carlos, 2025.

Tese (Doutorado) - Programa de Pós-Graduação em Engenharia Civil (Engenharia de Estruturas) e Área de Concentração em Estruturas -- Escola de Engenharia de São Carlos da Universidade de São Paulo, 2025.

1. 3D dipole-based BEM formulation. 2. Viscous-cohesive fracture problems. 3. Bayesian updating with structural reliability method. 4. Park-Paulino-Roesler cohesive zone model. I. Título.

Eduardo Graziosi Silva - CRB - 8/8907

FOLHA DE JULGAMENTO

Candidato: Bacharel **LUÍS PHILIPE RIBEIRO ALMEIDA**.

Título da tese: "Representação da falha por fratura de estruturas tridimensionais compostas por materiais quase frágeis submetidas a diferentes taxas de velocidade de carregamento pela abordagem do MEC dipolos e atualização Bayesiana".

Data da defesa: 15/05/2025.

Comissão Julgadora	**Resultado**
Prof. Titular Edson Denner Leonel (Orientador) (Escola de Engenharia de São Carlos/EESC-USP)	APROVADO
Prof. Dr. Ayrton Ribeiro Ferreira (Escola de Engenharia de São Carlos/EESC-USP)	Aprovado
Prof. Dr. Rodrigo Guerra Peixoto (Universidade Federal de Minas Gerais/UFMG)	APROVADO
Prof. Dr. Francisco Evangelista Junior (Universidade de Brasilia/UnB)	APROVADO
Prof. Dr. Eduardo Toledo de Lima Junior (Universidade Federal de Alagoas/UFAL)	APROVADO

Coordenador do Programa de Pós-Graduação em Engenharia Civil (Engenharia de Estruturas):
Prof Associado **Ricardo Carrazedo**

Presidente da Comissão de Pós-Graduação:
Prof. Titular **Carlos De Marqui Junior**

ABSTRACT

ALMEIDA, L.P.R. **The fracture failure modelling of three-dimensional structures composed of quasi-brittle materials subjected to different loading velocities rates by the dipole-based BEM approach and Bayes updating**. 2025. 158p. Phd Thesis - São Carlos School of Engineering, São Carlos, 2025.

The main objective of this doctoral thesis is the development of an alternative Boundary Element Method (BEM) formulation to model cohesive crack propagation in three-dimensional components, including loading rate effects. In addition, a new framework to quantify viscous-cohesive parameters in Nonlinear Fracture Mechanics (NFM) problems is proposed. The developed methodology couples the viscous-cohesive dipole-based BEM approach to the Bayesian Updating with Structural reliability method (BUS). The BEM formulation used is based on the introduction of an initial stress field to represent the mechanical behavior within the Fracture Process Zone (FPZ). The degeneration of this stress field along the crack boundaries results in the quantity dipole, which captures the nonlinear fracture effects. The influence of the loading rate on the material strength within the FPZ is properly handled by a viscous function, which updates the cohesive crack model. The Park–Paulino–Roesler (PPR) cohesive zone model governs the nonlinear mechanical behavior within the FPZ. Then, an update to the PPR cohesive model, to incorporate the effects of the loading rate during the cohesive crack propagation, is also proposed. The results obtained, including mixed-mode crack propagation, through this formulation are compared with reference solutions from experimental, analytical, and numerical approaches.

Keywords: 3D dipole-based BEM formulation. Viscous-cohesive fracture problems. Bayesian updating with structural reliability method. Park-Paulino-Roesler cohesive zone model.

RESUMO

ALMEIDA, L.P.R. **Representação da falha por fratura de estruturas tridimensionais compostas por materiais quase frágeis submetidas a diferentes taxas de velocidade de carregamento pela abordagem do MEC dipolos e atualização Bayesiana**. 2025. 158p. Tese (Doutorado)- Escola de Engenharia de São Carlos, Universidade de São Paulo, São Carlos, 2025.

O principal objetivo desta tese de doutorado é o desenvolvimento de uma formulação alternativa do Método dos Elementos de Contorno (MEC) para modelar a propagação de fissuras coesivas em componentes tridimensionais incluindo os efeitos da taxa de carregamento. Além disso, é proposta uma nova metodologia para a calibração de parâmetros visco-coesivos em problemas de Mecânica da Fratura Não Linear (MFLN). A estrutura desenvolvida acopla o MEC dipolos visco-coesivo a um método de atualização bayesiana com confiabilidade estrutural. A formulação do MEC empregada baseia-se na introdução de um campo de tensões iniciais para representar o comportamento mecânico dentro da Zona de Processos Inelásticos (ZPI). A degeneração deste campo de tensões ao longo das bordas da fissura resulta na variável dipolo, que captura os efeitos não lineares de fratura. A influência da taxa de carregamento sobre a resistência do material na ZPI é adequadamente tratada por uma função viscosa, que atualiza o modelo de fratura coesiva. O modelo de zona coesiva Park–Paulino–Roesler (PPR) rege o comportamento mecânico não linear na ZPI. Assim, uma atualização do modelo coesivo PPR, para incorporar os efeitos da taxa de carregamento durante a propagação coesiva das fissuras, também é proposta. Os resultados obtidos por meio dessa formulação, incluindo modo misto de propagação, são comparados com soluções de referência experimentais, analíticas e numéricas.

Palavras-chave: Método dos Elementos de Contorno 3D baseado em dipolos. Propagação de fissuras visco-coesivas. Atualização bayesiana com confiabilidade estrutural. Modelo de zona coesiva Park-Paulino-Roesler (PPR).

ACKNOWLEDGEMENTS

The following research project would not be possible without the unconditional support of my family and incentive over the course of these intense years, specially my mother Elisângela Ribeiro Bastos and father Rivaldo Almeida Luiz. Special thanks go to my lovely girlfriend Ana Mozzer, who has been by my side during this journey.

I gratefully acknowledge my advisor Prof. Edson Denner Leonel for the supervision, guidance, partnership and friendship built over these years. Our partnership has great impact in my personal and professional achievements. Special thanks are extended to Senior Lecture Elena Atroshchenko at UNSW (Sydney/Australia), whose valuable guidance and assistance were essential for the developments of this thesis.

I would like to express my gratitude to the professors who have provided valuable lessons and served as sources of inspiration throughout my academic and professional journey. I would especially like to thank my supervisors, Eduardo Toledo de Lima Junior (UFAL), João Carlos Cordeiro Barbirato (UFAL) and Fábio Carlos da Rocha (UFS), for their guidance and support.

I would like to thank all my friends from São Carlos for the enjoyable times spent together. Special thanks for my colleagues: Matheus Rocha, Isabela Durci, Ray Calazans, Daniel Teles, Welington Vieira, Delfino, Sérgio Cordeiro, Caio Ramos, Herbert.

I acknowledge the staff at the Department of Structural Engineering (SET) for their support, cordiality and solicitude throughout my doctoral years.

I would also like to thank the Laboratory of Scientific Computing and Visualization (LCCV), especially for the new friendships that I made during this final stage of my PhD.

The following research project would not be possible without the sponsorship from Coordenação de Aperfeiçoamento de Pessoal de Nível Superior - Brasil (CAPES) - Finance Code 001.

LIST OF FIGURES

LIST OF TABLES

CONTENTS

1 INTRODUCTION

The effective structural design requires accurate approaches for assessing stresses and displacements fields, which enable the proper prevention of material collapses. Because many of these collapses type can be explained consistently by the presence of internal flaws, fracture mechanics theories stand out as a robust tool for predicting the material and structure failures. Therefore, collapses configurations caused by crack propagation can be predicted properly within realistic descriptions of the material failure mechanisms. In cracked materials, the energy dissipation phenomena and the material damage evolution occur at the crack tip region called fracture process zone (FPZ). When the FPZ is small in comparison to the structural dimensions, linear elastic fracture mechanics (LEFM) can be applied. On the other hand, nonlinear fracture mechanics (NLFM) describes properly the mechanical behaviour of large FPZ, which triggers nonlinear effects that cannot be disregarded.

In spite of the robustness of fracture mechanics theories, the analytical predictions available in this domain are restricted to a small number of problems, in which simplified boundary conditions, geometry and constitutive laws have been assumed. Therefore, the application of fracture mechanics theories in complex and real world problems requires numerical approaches. The finite element method (FEM) has been applied largely in fracture mechanics (BITTENCOURT; WAWRZYNEK; INGRAFFEA, 1996; BELYTSCHKO; BLACK, 1999), including its extended version (UNGER; ECKARDT; KONKE, 2007; MOHAMMADI, 2008; WANG; BACKER; CHEN, 2016; LI; LI; YUAN, 2018; AGATHOS; BORDAS; CHATZI, 2019; TIAN; WEN; WANG, 2019; WANG; BACKER; CHEN, 2016; BENTO; PROENÇA; DUARTE, 2023) and the stable generalized finite element method (FONSECA *et al.*, 2020), despite the inherent mesh dependency and exhaustive processes associated to the crack propagation in domain methods. The mesh dependency issues have been minimised within element-free and meshfree methods (GARG; PANT, 2018). In this domain, it is worth mentioning the advances in element-free Galerkin method (EFG) (LU; BELYTSCHKO; GU, 1994), radial reproducing kernel particle methods (RKPM) (LIU; JUN; ZHANG, 1995), meshless local Petrov-Galerkin method (MLPG) (CHING; YEN, 2005), cracking particles method (CPM) (RABCZUK; BELYTSCHKO, 2004), radial point interpolation method (RPIM) (GU *et al.*, 2011), particle difference method (LEE;

KIM; YOON, 2016) and hybrid meshless displacement discontinuity method (MDDM) (ZHENG *et al.*, 2021). Some additional contributions to the fracture mechanics field can also be highlighted such as the phase-field numerical manifold method (PFNMM) (YANG; YANG; ZHENG, 2021) and the thermo-mechanical peridynamic model (TMPM) (BAZAZZADEH; MOSSAIBY; SHOJAEI, 2020). It is worth emphasizing that many of these recent advances encompass two-dimensional case within LEFM framework. Besides, the developments on the NLFM formulations in the three-dimensional context are in lower number in comparison to the achievements in the LEFM within two-dimensional description. Nevertheless, the domain methods, FEM especially, predominate in this field.

Cohesive zone models (CZM) have been widely used to simulate nonlinear fracture problems. The idea of creating a fictitious crack in front of the real crack tip and enforcing it to be closed by means of cohesive tractions makes possible to phenomenologically reproduce the fracture phenomena. Usually, the CZM relates the cohesive stresses, σ, to the crack opening displacement values, w, by introducing a constitutive law, which enables the FPZ representation. Some works using FEM and constitutive laws have been proposed, which include bilinear (MORAIS *et al.*, 2015), polynomial (FREED; BANKS-SILLS, 2008), and exponential laws (LIU; ISLAM, 2013). Despite being widely used, the models previously mentioned have their accuracy linked to the type of material to be modelled (quasi-brittle and ductile), which is an important drawback. In this regard, Park, Paulino and Roesler (2009), Cerrone *et al.* (2014) proposed an unified potential-based cohesive model capable of representing a wide variety of materials, and also different fracture energies, by choosing appropriate parameters. As for the CZM, there are two kinds of formulations in terms of traction-separation law, the intrinsic (QIN; CHEN; ASAI, 2023) and extrinsic (NGUYEN, 2014; CHEN *et al.*, 2019) models. The main difference between them is the presence of the initial slope in the traction-separation curve. Thus, in the extrinsic models, the crack opening displacements only start after the traction reaches the cohesive material strength. The intrinsic PPR CZM is used in this work, enabling the adjust of pre-peak curve inclination by introducing initial slope parameters

On the side of boundary mesh methods, the boundary element method (BEM) enables effective solutions for fracture mechanics problems. Because of the non-requirement of domain mesh and consequently domain approximations, the remeshing procedures during crack propagation are less complex and the stresses concentrations at the FPZ can be described naturally. The BEM has been applied extensively in two-dimensional fracture analyses. These efforts triggered several BEM formulations such as: the displacement discontinuity method (CROUCH, 1976; GOSPODINOV, 2003; CHEN *et al.*, 2018), the symmetric Galerkin method (MAIER; G.; CEN, 1993), the multi-zone BEM (CHEN; WANG; CEN, 1999) and the continuum strong discontinuity approach (CSDA) (PEIXOTO; RIBEIRO; PITANGUEIRA, 2018). In addition, Gulizzi, Benedetti and Milazzo (2019)

presented a novel BEM formulation based on the derivation of a supplementary boundary integral equation to model anisotropic cracked materials. However, until the present, the versatile BEM approach in fracture field is the dual boundary element method (DBEM) (PORTELA; ALIABADI; ROOKE, 1992; SOLLERO; ALIABADI, 1994; SALEH; ALIABADI, 1995), which requires singular and hypersingular integral equations. The singular integral equation governs the collocation point at one crack surface whereas the hypersingular integral equation governs the coincident symmetrically positioned collocation point (CHEN; WANG; CEN, 1999). Some remarkable developments in both single and multiple crack growth analyses via DBEM are available in the literature: Cordeiro and Leonel (2016), Leonel and Venturini (2010), Price and Trevelyan (2014), Xiao, Yue and Xiao (2019), Andrade and Leonel (2020), for instance.

The BEM demonstrates robustness and accurate performance in the three-dimensional fracture mechanics context. Mi and Aliabadi (1992) extended the DBEM formulation to the three-dimensional analyses within LEFM and Cisilino, Aliabadi and Otegui (1998) utilised the DBEM to the elastoplastic modelling of cracked bodies. Alternative BEM formulations, such as the displacement discontinuity method (XIAO; YUE, 2011), have also been applied in the three-dimensional fracture mechanics. Furthermore, the combination of FEM and BEM, in which the FEM assesses the internal fields values without any crack and the BEM simulates the material discontinuity can also be encountered in the literature (GIANNELLA *et al.*, 2017; CITARELLA *et al.*, 2016; GIANNELLA; PERRELLA; CITARELLA, 2017; GIANNELLA *et al.*, 2018). Besides, Gulizzi, Rycroft and Benedetti (2018) and Benedetti, Gulizzi and Milazzo (2019) coupled BEM formulations to suitably defined cohesive laws (with multi-physics coupling) for modelling fracture mechanics problems in polycrystalline materials. However, the DBEM formulation is, until the present, the versatile BEM approach in this domain (CITARELLA; BUCHHOLZ, 2008; CARLONE *et al.*, 2016; CITARELLA *et al.*, 2016). Moreover, the DBEM formulation also leads to the accurate modelling into the Isogeometric form (IGABEM) (PENG *et al.*, 2017; CORDEIRO; LEONEL, 2018). Cordeiro and Leonel (2019) proposed an improved framework based on the DBEM approach for mixed-mode crack propagation modelling in three-dimensional components within LEFM. Sun and Dong (2021) analysed the crack propagation phenomenon in infinite media using the IGABEM, in which crossings among crack surfaces and external boundaries have not been accounted. This brief literature review indicates higher number of developments in two-dimensions description in comparison to the three-dimensional case. Besides, the BEM advances in three-dimensions involve predominantly DBEM and LEFM domain. It is important to mention that NLFM and cohesive crack growth modelling have not been explored totally in the three dimensional case within BEM (ROCHA; LEONEL, 2022; CHAVES; PEIXOTO; SILVA, 2021; CHAVES; PEIXOTO; SILVA, 2023), which inspired the developments proposed herein. Rocha and Leonel (2022) analysed the three-dimensional cohesive crack propagation using the subre-

gion BEM technique whereas Chaves, Peixoto and Silva (2021) used the continuum strong discontinuity approach (CSDA) for the same purpose. It is worth citing that (ROCHA; LEONEL, 2022; CHAVES; PEIXOTO; SILVA, 2021; CHAVES; PEIXOTO; SILVA, 2023) assumed predefined crack paths based on experimental responses. Differently, the DBEM and the herein proposed dipole-based formulation enables the cohesive crack propagation modelling, in which the crack surfaces geometry evolves as a function of loading and stresses values, i.e. without any assumption of predefined crack paths.

The dipole-based approach introduces an initial stress field to model the separation effects between the crack's surfaces (OLIVEIRA; LEONEL, 2013; ALMEIDA; LIMA JUNIOR; BARBIRATO, 2020a; ALMEIDA; LIMA JUNIOR; BARBIRATO, 2022; ALMEIDA; LEONEL, 2024b; ALMEIDA; LEONEL, 2024a; ALMEIDA; ATROSHCHENKO; LEONEL, 2025). Initially, the displacements and stresses from the solid without discontinuities are modelled using the traditional elastic 3D BEM formulation. Next, the mechanical field is corrected by introducing virtual forces, the so-called dipoles. Then, virtual forces are responsible to represent the discontinuities inside the solid's domain, enabling the proper description of boundary conditions at the crack's surfaces. Further, this alternative formulation can represent the nonlinear fracture problem with less algebraic equations than other classic formulations. For instance, the DBEM solves the 3D fracture problem with six algebraic equations (three traction and three displacement equations per couple of points in each crack's surface). In opposite, the dipole-based formulation solves the same problem with only three algebraic equations. Thus, this alternative formulation provides an effective and suitable tool to solve three-dimensional cracked problems with less computational effort, which is a bottle neck in three-dimensional problems. In spite of its accuracy and effectivity, the dipole-based BEM formulation has been limited to two-dimensional crack propagation problems, until the present. The present study extends the dipole-based approach (OLIVEIRA; LEONEL, 2013; ALMEIDA; LIMA JUNIOR; BARBIRATO, 2020a) to the three dimensional context, which is the novelty herein. Besides, until the present, the BEM formulations have been extensively coupled to the traditional, linear, bilinear, exponential cohesive laws (or even laws derived from them), to model cohesive cracks. Therefore, in this study, for the first time, the PPR cohesive zone model (PARK; PAULINO; ROESLER, 2009; PARK; PAULINO, 2012; CERRONE *et al.*, 2014; CORDEIRO; DAUMAS; MONTEIRO, 2024) is coupled to a 3D BEM formulation, enabling proper representation of the cohesive crack propagation process by introducing shape parameters from the PPR model.

In the above-mentioned works, the nonlinear fracture of quasi-brittle materials has often been modelled by the cohesive fracture mechanics approach, in which cohesive stresses represent the residual material strength in the FPZ. Then, the virtual crack replaces both FPZ and stresses, and cohesive forces close the surfaces of the virtual crack

surfaces. Despite being successful in quasi-static modelling, the classic approach may not be realistic in some engineering problems. In fact, some experimental results demonstrate that the loading velocity rate largely modifies the resistance behaviour of the material in the FPZ (RUSH, 1960; RUIZ *et al.*, 2010; WITTMAN *et al.*, 1987), see Fig. 1. The resistant load (load peak) increases monotonically with an increasing loading velocity rate, while the displacement associated to the peak load remains virtually the same (WITTMAN *et al.*, 1987).

Figure 1 – Force *versus* displacement curves considering different loading rates

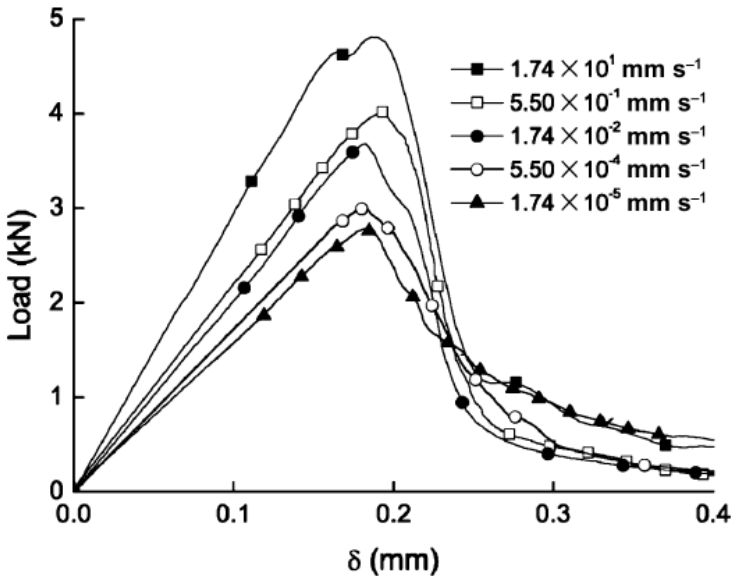

Fonte: (RUIZ *et al.*, 2010)

Some works with important contributions can be mentioned: Zhang *et al.* (2010) tested specimens of high-strength concrete beams in different loading velocity rates, ranging from $10^{-4}\,mm/s$ to $10^{3}\,mm/s$, while Rosa *et al.* (2012) introduced a time-dependent function ψ, to enable the viscous-effects modelling at FPZ. ψ is a weighting function that modifies the cohesive zone model. Further, Stephen and Gettu (2019) analysed reinforced concrete structures, whereas Xing *et al.* (2020) tested specimens with different materials (rock types). Based on the previous works, the conventional classic cohesive models are not capable of capturing the effect of increasing loading velocity rates. Hence, Santos and Sousa (2020) proposed an alternative strategy to account viscous-cohesive effects in crack propagation process. This strategy enables the decrease in the threshold crack opening, w_c, with increasing loading velocity rates. This improvement represents properly the experimental observations (WITTMAN *et al.*, 1987; BAZANT; GETTU, 1992; REINHARDT, 1990) available in the literature. However, the approach proposed by Santos and Sousa (2020) have not been totally explored numerically. Thus, the coupling of the viscous-cohesive nonlinear fracture model proposed by Santos and Sousa (2020)

with a three-dimensional formulation is another contribution of the present study. Despite being an alternative in modelling viscous-cohesive problems, the efficiency of the classic cohesive laws is linked to the type of material modelled. Alternatively, the PPR cohesive model can be utilised, enabling the representation of a wide variety of materials. Therefore, this study proposes a modification in the PPR model to account the viscous effects from Santos and Sousa (2020) nonlinear fracture model, which leads to a robust and general fracture mechanics approach. This new coupled methodology is another novelty herein.

Despite the robustness of this coupled formulation, the determination of viscous-cohesive parameters is still a complex task in the analysis. All models discussed in the previous paragraph offer deterministic predictions of these parameters without accounting for the uncertainties related to the lack of information about the exact/experimental value of the process (PERALTA; RUIZ; TAFLANIDIS, 2020). A large scatter can be found in experimental results leading from the process randomness (CORDEIRO; LEONEL; BEAUREPAIRE, 2017). Therefore, the use of deterministic approaches to quantify such parameters can compromise the numerical predictions accuracy once the knowledge about the model characteristics is not complete. According to Straub and Papaioannou (2015), a consistent and effective framework for combining new information with existing models is provided by Bayesian analysis, in which prior distributions are updated taking into account the experimental results and the error from the numerical model. Although deterministic strategies to infer parameters of a model by minimising the error between experimental and numerical data can be used, the Bayesian inference is particularly attractive as it enables the combination of uncertain and incomplete data from experimental and numerical curves, allowing the probabilistic information of the updated model.

In this context, among all the works in this field of research, some can be highlighted: Benjamin and Cornell (1970) used the Bayesian updated approach to quantify parameters through geotechnical site investigation. Regarding studies in dynamics, Natke (1988) and Beck and Katafygiotis (1998) applied the Bayesian analysis to identifying parameters through vibration measurements. Recently, Beven (2008) applied the Bayesian model to rainfall and discharge measurements. In all previous studies, the Bayesian inference starts with the initial knowledge about parameters involved in the analysis, which is called the prior distribution. Using the experimental data available, the prior distribution is updated to obtain a posterior distribution, which is achieved by using Bayes's theorem and the likelihood of the experimental data (PERALTA; RUIZ; TAFLANIDIS, 2020). However, the posterior distribution estimation may be a changeling task, involving the evaluation of highly dimensional integrals. Nonetheless, this task can be circumvented using the Markov Chain Monte Carlo (MCMC) method (BECK, 2010) or even by approximating the peak of the posterior probability density function (PDF), referenced as maximum a posteriori (MAP) (BECK; TAFLANIDIS, 2013). Other alternatives can also be mentioned, including

subspace identification techniques (WENG; LOH; YANG, 2009) and Kalman-filtering-based approaches (ASTROZA *et al.*, 2019).

In addition, the challenging task of evaluating highly dimensional integrals can be circumvented by using a coupling of Bayesian approaches and structural reliability methods, the so-called BUS approaches (Bayesian Updating with Structural reliability methods). Some of the advantages of the method are reflected in its simplicity of implementation and the possibility of using structural reliability methods associated to software for Bayesian updating (STRAUB; PAPAIOANNOU, 2015). In this context, Straub and Papaioannou (2015) introduced the BUS model, in which the posterior data was obtained by using subset simulation (AU; WANG, 2008). Diaz *et al.* (2017), Betz *et al.* (2018), and Tian *et al.* (2021) presented further developments regarding the subset simulation and the BUS models. In these works, the posterior distribution was achieved by means of a rejection sampling algorithm combined with structural reliability methods and the BUS framework. Regarding fracture mechanics, Cordeiro, Leonel and Beaurepaire (2017) proposed a stochastic procedure to quantify cohesive parameters by coupling the DBEM approach and BUS procedure. In spite of its robustness, this last contribution has been limited to two-dimensional domain and time-independent problems. Thus, the development of models capable of adequately quantifying parameters that govern the viscous-cohesive crack propagation process is still a major task in the engineering field, which inspired the developments herein.

1.1 Objectives and innovative aspects

The objective of this study, and the main contribution, is the extension of the dipole-based BEM formulation, originally presented in the two-dimensional crack propagation context, to three-dimensional viscous-cohesive analysis. In addition, a new framework to quantify viscous-cohesive material parameters considering loading rate-dependent applications is presented.

Initially, a 3D dipole-based BEM formulation is developed to simulate cohesive crack growth. The main features of the proposed method are:

- Extension of the dipole-based approach to three dimensional context with the integral kernels associated to degeneration of the stress field along the FPZ surface.
- Definition of the dipole kernels integration along the singular elements using Guiggiani strategy.
- Three dimensional fracture modelling including mixed-mode crack propagation.

Then, the present study couples the 3D dipole-based BEM formulation to a viscous-cohesive approach. The developments herein lead to an approach capable of modelling the fracture of three-dimensional structures composed of quasi-brittle materials by a nonlinear viscous-cohesive description. The novel aspects of the novel formulation are:

- A new methodology for viscous-cohesive crack growth modelling considering different loading velocities rates adequately represented by a time-dependent function, which updates the cohesive model.
- A new framework that couples the PPR cohesive zone model to the 3D dipole-based BEM formulation.
- A modification in the PPR polynomial potential method is proposed, enabling the modelling of the quasi-brittle fracture responses and time-dependent effects.

Finally, new framework to quantify viscous-cohesive material parameters considering loading rate-dependent applications is proposed. Its originality is on the spot when viscous-cohesive BEM and BUS procedures are coupled. Among the novelties of this numerical method are:

- The coupling of the 3D dipole-based formulation to the BUS approach, allowing an effective procedure capable of handling the inherent randomness of the viscous-cohesive process.
- Development of a stochastic inverse procedure that provides the most representative viscous-cohesive parameter values that minimise the error between experimental and numerical solutions.
- Development of a surrogate model based on Artificial neural networks (ANN) to simplified the representation of the numerical model and reduce computational costs.

Several numerical applications are presented to demonstrate the accuracy of all formulations herein proposed. The results are compared with analytical, experimental and numerical solutions available in the literature

1.2 Methodology

This doctoral thesis is inserted in the developments of the research group on fracture problems using BEM of the Department of Structural Engineering from the São Carlos School of Engineering at the University of São Paulo, under supervision of Prof. Edson Denner Leonel. The first part of this thesis can be seen as a continuation of the author's

master's degree (ALMEIDA; LIMA JUNIOR; BARBIRATO, 2020a), in which the dipole-based formulation has been extended for the analysis of three-dimensional components. Notably, the contributions from Barbirato (1999) are essential. In his work, the author introduced a 3D dipole-based BEM approach for fracture problems, employing constant elements for domain discretization and a predefined crack path. However, it is important to highlight that the use of the 3D dipole-based formulation was not fully explored in Barbirato (1999), which inspired the advancements proposed in this thesis. It is important to highlight that chapter 6 of this thesis was carried out in collaboration with Senior Lecturer Elena Atroshchenko at UNSW-Sydney Australia.

Following, the 3D dipole-based BEM code was integrated with a viscous-cohesive methodology to model loading rate-dependent fracture problems. The viscous-cohesive approach proposed by Santos and Sousa (2020) has been adopted for this purpose. Besides, the PPR CZM proposed by Park, Paulino and Roesler (2009) has been used in this study, enabling accurate representation of the cohesive crack propagation process by incorporating shape parameters from the PPR model. Additionally, the BUS approach (STRAUB; PAPAIOANNOU, 2015) was utilized to calibrate the viscous-cohesive fracture parameters. All BEM formulations were implemented using FORTRAN 90. The computational device used for the analyses is an AMD Ryzen 9 3900X with a clock speed of 3.79 GHz, featuring 12 cores and 32 GB of RAM. Besides, the computational code does not incorporate high-performance computing techniques, such as parallel processing schemes.

1.3 Organisation of the text

The text is organized as follows. In chapter 2, the classical 3D BEM formulation is introduced, covering key topics such as the basic equations, Somigliana identity (SOMIGLIANA, 1885), the limit process, algebraic representation, and analysis at internal points. In chapter 3, fracture mechanics aspects and the theoretical foundation of the 3D dipole-based BEM formulation are discussed, including the integral representation, contributions to crack opening, and algebraic representation. chapter 4 explores the coupling of the 3D dipole-based BEM formulation with the viscous-cohesive model proposed by Santos and Sousa (2020). In chapter 5, the theoretical background of the Park-Paulino-Roesler (PPR) cohesive zone model is presented. Finally, chapter 6 introduces the general concepts of the Bayesian updating model, focusing on the likelihood function, and its integration with structural reliability methods and model class selection. The surrogate model employed in the Monte Carlo simulations is also described. In chapter 7, the final remarks and recommendations for future work are presented.

2 BOUNDARY ELEMENT METHOD

This chapter presents the theoretical foundations of the Boundary Element Method (BEM) within the context of linear elasticity. The discussion begins with the formulation of the boundary value problem for linear elasticity, followed by the necessary derivations, including Somigliana's identity (SOMIGLIANA, 1885). A key advantage of BEM is that it eliminates the need to discretize the entire domain, focusing solely on the boundary. This simplification significantly streamlines the analysis and has contributed to the widespread adoption of BEM in the scientific community for solving various engineering problems.

The Boundary Element Method provides an elegant and computationally efficient alternative to other numerical techniques, such as domain-based methods, which typically require the meshing of the entire problem domain. Due to its advantages, BEM has found extensive applications in a variety of fields, including fluid mechanics, linear and nonlinear elasticity, fracture mechanics, structural dynamics, electromagnetism, and acoustics, among others (ALMEIDA; LIMA JUNIOR; BARBIRATO, 2020b).

This chapter discusses the fundamental solution used for three-dimensional elastic problems. Following this, the limit process is introduced to enable the formulation of integral equations along the boundary of the solid. Subsequently, aspects of Lagrangian interpolation are presented, particularly in relation to element integration and the adopted strategy. In this context, the resulting algebraic system is assembled to solve for the unknown mechanical fields. Additionally, operations related to internal quantities are demonstrated, which are computed based on the responses obtained from the BEM system. It is important to note that the developments presented in this chapter are based on Aliabadi (2002), and the notation for tensor representation follows the index notation convention.

2.1 Initial considerations

2.2 Somigliana identity and Kelvin's fundamental solution

Consider a boundary value problem (BVP) with domain Ω and boundary Γ, subjected to domain forces b_k, surface forces $\bar{p}_i$, acting on the boundary Γ_p and prescribed

displacements $\bar{u}_i$, acting on the boundary Γ_u. Dynamic effects are neglected.

Figure 2 – Solid on which BVP of linear elasticity is developed

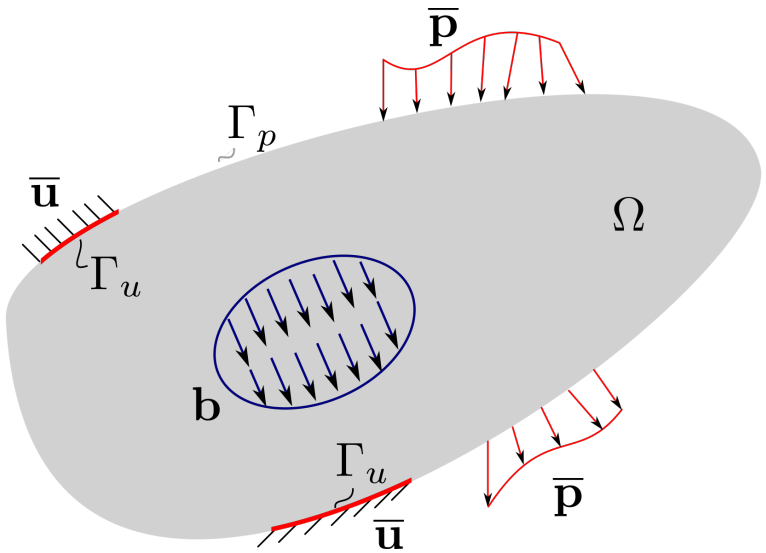

Source: The author.

The equation governing the problem can be written as follows:

$$\sigma_{jk,j} + b_k = 0_k \tag{2.1}$$

In models based on BEM, the mechanical behaviour of elastic structures must be formulated from integral equations written along the solid boundary. The weighted residual method can be applied to obtain the elastic formulation of the BEM (BREBBIA, 1978). Thus, for the three-dimensional case, the fundamental Kelvin equation for the three-dimensional field weighted by the equilibrium relation, Eq. 2.1, is written as follows:

$$\int_\Omega \left(\sigma_{jk,j} + b_k\right) w_k \, d\Omega = 0 \tag{2.2}$$

where w_k is the weighting function. The weighting function used here is based on the Kelvin fundamental solution (KELVIN, 1848). This solution relates the displacements $u^*_{\ell k}$ and surface forces $p^*_{\ell k}$ in the direction k of a given point Q before the application of a punctual and unitary force of direction ℓ at the point S, called source point. The solutions for displacements and surface forces are as follows:

$$\begin{aligned} u^*_{\ell k}(Q,S) &= \frac{1}{16\pi\mu\,(1-\nu)\,r}\left[(3-4\nu)\,\delta_{\ell k} + r_{,\ell} r_{,k}\right] \\ p^*_{\ell k}(Q,S) &= \frac{-1}{8\pi\,(1-\nu)\,r^2}\left\{\frac{\partial r}{\partial \mathbf{n}}\left[(1-2\nu)\,\delta_{\ell k} + 3r_{,\ell} r_{,k}\right] - (1-2\nu)\left(r_{,\ell} n_k + r_{,k} n_\ell\right)\right\} \end{aligned} \tag{2.3}$$

Applying integration by parts on the first term of Eq. 2.2, we obtain:

$$\int_\Omega \left(\sigma_{jk} u^*_{\ell k}\right)_{,j} d\Omega - \int_\Omega \sigma_{jk} u^*_{\ell k,j} d\Omega + \int_\Omega b_k u^*_{\ell k} \, d\Omega = 0_\ell \tag{2.4}$$

Then, applying the divergence theorem on top of Eq. 2.4:

$$\int_{\Gamma} \sigma_{jk} u^*_{\ell k} n_j \, d\Gamma - \int_{\Omega} \sigma_{jk} u^*_{\ell k,j} d\Omega + \int_{\Omega} b_k u^*_{\ell k} \, d\Omega = 0_\ell \tag{2.5}$$

Taking into account the symmetry of the stress tensor ($\sigma_{jk} = \sigma_{kj}$) and the Cauchy equation ($p_k = \sigma_{kj} n_j$), the Eq. 2.4 is rewritten as:

$$\int_{\Gamma} u^*_{\ell k} p_k \, d\Gamma - \int_{\Omega} \sigma_{kj} u^*_{\ell k,j} d\Omega + \int_{\Omega} b_k u^*_{\ell k} \, d\Omega = 0_\ell \tag{2.6}$$

From the compatibility relation $\varepsilon^*_{\ell kj} = (\, u^*_{\ell k,j} + u^*_{\ell j,k})/2$, it is valid assert that $\sigma_{kj} u^*_{\ell k,j} = \sigma_{kj} \varepsilon^*_{\ell kj}$. In this regard, Eq. 2.6 becomes:

$$\int_{\Gamma} u^*_{\ell k} p_k \, d\Gamma - \int_{\Omega} \sigma_{kj} \varepsilon^*_{\ell kj} d\Omega + \int_{\Omega} b_k u^*_{\ell k} \, d\Omega = 0_\ell \tag{2.7}$$

Hooke's isotropic linear constitutive relation is then applied, which leads to:

$$\int_{\Gamma} u^*_{\ell k} p_k \, d\Gamma - \int_{\Omega} \sigma^*_{\ell kj} \varepsilon_{kj} \, d\Omega + \int_{\Omega} b_k u^*_{\ell k} \, d\Omega = 0_\ell \tag{2.8}$$

Then, from the compatibility relation, $\sigma^*_{\ell kj} \varepsilon_{kj} = \sigma^*_{\ell kj} u_{k,j}$, we obtain:

$$\int_{\Gamma} u^*_{\ell k} p_k \, d\Gamma - \int_{\Omega} \sigma^*_{\ell kj} \, u_{k,j} \, d\Omega + \int_{\Omega} b_k u^*_{\ell k} \, d\Omega = 0_\ell \tag{2.9}$$

A new integral evaluated on the boundary is obtained by applying the Divergence theorem and integrating by parts:

$$\int_{\Gamma} u^*_{\ell k} p_k \, d\Gamma - \int_{\Gamma} p^*_{\ell k} u_k \, d\Gamma + \int_{\Omega} \sigma^*_{\ell jk,j} u_k d\Omega + \int_{\Omega} b_k u^*_{\ell k} \, d\Omega = 0_\ell \tag{2.10}$$

The domain force from the fundamental problem can be presented from the Dirac Delta, as $b^*_{\ell k} = \delta_{\ell k} \Delta \, (Q - S)$. Replacing the domain force from the fundamental problem in the integral, it becomes possible to apply the Dirac Delta filtering property. Thus, the result of the aforementioned integral is $-u_\ell$ for an internal source point and zero for an external source point. In short, Eq. 2.10 becomes the Somiglian Identity (SOMIGLIANA, 1885):

$$c_{\ell k}(S) u_k(S) + \int_{\Gamma} p^*_{\ell k} u_k \, d\Gamma = \int_{\Gamma} u^*_{\ell k} p_k \, d\Gamma + \int_{\Omega} b_k u^*_{\ell k} \, d\Omega \tag{2.11}$$

$c_{\ell k}(S)$ is the free term, which depends on the position of the source point in order to determine its value. For an internal source point, $c_{\ell k} = \delta_{\ell k}$, and for an external source point, $c_{\ell k} = 0_{\ell k}$. Thus, the Somiglian identity connects the displacement field at a point S to the known magnitudes on the boundary. The domain integral can be computed in various ways, such as using a radial integration process (GAO, 2002) or employing the dual Reciprocity method (PARTRIDGE; BREBBIA; WROBEL, 1992a). For simplicity, domain forces are assumed to be zero, and consequently, the final term in Eq. 2.11 is excluded from

further developments. The integral relationship for stresses can also be derived, starting from the compatibility equation and the constitutive relationship, resulting in:

$$\sigma_{\ell j}(S) + \int_{\Gamma} S^*_{k\ell j} u_k \, d\Gamma = \int_{\Gamma} D^*_{k\ell j} p_k \, d\Gamma + \int_{\Omega} D^*_{klj} b_k d\Omega \tag{2.12}$$

where the fundamental solutions $D^*_{k\ell j}$ and $S^*_{k\ell j}$ are:

$$\begin{aligned} D^*_{k\ell j}(Q,S) &= \frac{1}{8\pi(1-\nu)r^2}\left[(1-2\nu)(\delta_{k\ell}r_{,j} + \delta_{jk}r_{,\ell} - \delta_{\ell j}r_{,k}) + 3(r_{,\ell}r_{,j}r_{,k})\right] \\ S^*_{k\ell j}(Q,S) &= \frac{\mu}{4\pi(1-\nu)r^3}\{3\frac{\partial r}{\partial n}[(1-2\nu)\delta_{\ell j}r_{,k} + \nu(\delta_{\ell k}r_{,j} + \delta_{jk}r_{,\ell}) - 5r_{,\ell}r_{,j}r_{,k}] \\ &+3\nu(n_\ell r_{,j}r_{,k} + n_j r_{,\ell}r_{,k}) + (1-2\nu)(3n_k r_{,\ell}r_{,j} + n_j\delta_{\ell k} + n_\ell\delta_{jk}) - (1-4\nu)n_k\delta_{\ell j}\} \end{aligned} \tag{2.13}$$

A cutting plane defined by the normal vector $\mathbf{n}$ is next considered, in this way, the replacement of Eq. 2.13 in Cauchy's formula ($p_\ell = \sigma_{\ell j} n_\ell$) results in:

$$p_\ell(S) + n_\ell(S) \int_{\Gamma} S^*_{k\ell j} u_k \, d\Gamma = n_\ell(S) \int_{\Gamma} D^*_{k\ell j} p_k \, d\Gamma \tag{2.14}$$

2.3 Limit process: integral equations over the boundary

Eq. 2.11 and Eq. 2.14 provide a way to obtain the displacement values for any point within the domain, based on the forces and displacements on the boundary, the forces acting within the domain (if any), and the fundamental solution. Since the Somiglian Identity is valid only for points inside the domain, an integral representation for the boundary displacements is required. To achieve this, consider a semicircle with a radius centered on a smooth boundary point, as shown in Fig. 3. By letting the radius approach as zero, the modified Somiglian equation for the boundary is derived. This procedure is commonly referred to BEM as the limit process.

Figure 3 – Fictitious boundary for application of the limit process.

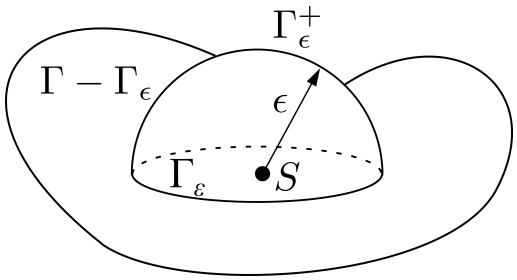

Source: The author.

Somigliana's identity, Eq. 2.11, can be rewritten taking into account the solution to the problem:

$$u_\ell(S) + \int_{\Gamma-\Gamma_\epsilon} p^*_{\ell k} u_k \, d\Gamma + \int_{\Gamma_\epsilon^+} p^*_{\ell k} u_k \, d\Gamma = \int_{\Gamma-\Gamma_\epsilon} u^*_{\ell k} p_k \, d\Gamma + \int_{\Gamma_\epsilon^+} u^*_{\ell k} p_k \, d\Gamma \tag{2.15}$$

Applying the limit process on Eq. 2.15, that is, considering the source point on the solid boundary when $\epsilon \to 0$:

$$\begin{aligned} u_k(S) + \lim_{\epsilon\to 0}\left(\int_{\Gamma-\Gamma_\epsilon} p^*_{\ell k} u_k \, d\Gamma\right) + \lim_{\epsilon\to 0}\left(\int_{\Gamma^+_\epsilon} p^*_{\ell k} u_k \, d\Gamma\right) \\ = \lim_{\epsilon\to 0}\left(\int_{\Gamma-\Gamma_\epsilon} u^*_{\ell k} p_k \, d\Gamma\right) + \lim_{\epsilon\to 0}\left(\int_{\Gamma^+_\epsilon} u^*_{\ell k} p_k \, d\Gamma\right) \end{aligned} \tag{2.16}$$

The integral over the boundary $\Gamma - \Gamma_\epsilon$ that contains the kernel u^* can be evaluated in the conventional way (Gauss quadrature), since it has a weak singularity in the limit, with order $O(r^{-1})$. The integral of u^* evaluated over the boundary Γ^+_ϵ tends to zero when $\epsilon \to 0$. However, the integrals on the right side of Eq. 2.15 present a strong singularity type, of the order $O(r^{-2})$. Thus, the portion $\lim_{\epsilon\to 0}\left(\int_{\Gamma-\Gamma_\epsilon} p^*_{\ell k} u_k \, d\Gamma\right)$ is evaluated towards the Principal Cauchy Value (PCV). The last integral, with kernel p^* is calculated on the boundary Γ^+_ϵ, and performed from the Taylor series displacement expansion, taking the first term, that is, $u_k = u_k - u_k(S) + u_k(S)$. Which results in:

$$\lim_{\epsilon\to 0}\left(\int_{\Gamma^+_\epsilon} p^*_{\ell k} u_k \, d\Gamma\right) = \lim_{\epsilon\to 0}\left[\int_{\Gamma^+_\epsilon} p^*_{\ell k}\left(u_k - u_k(S)\right) \, d\Gamma\right] + \lim_{\epsilon\to 0}\left[\int_{\Gamma^+_\epsilon} p^*_{\ell k} u_k(S) \, d\Gamma\right] \tag{2.17}$$

Due to the continuity of displacements, the first integral of Eq. 2.17 is null. Besides, since $u_k(S)$ is constant, and can be removed from the integral, the second integral can be rewritten as $u_k(S) \; lim_{\epsilon\to 0}\left[\int_{\Gamma^+_\epsilon} p^*_{\ell k} \, d\Gamma\right]$. The result of this integral is a constant, which is incorporated into the free term $c_{\ell k}$. For smooth boundaries, $c_{\ell k} = 0.5\delta_{\ell k}$. Thus, Eq. 2.11 is defined considering the source point on the boundary. Finally, from the kernel integration p^* towards the VPC, indicated by $\oint$, Eq. 2.11 can be rewritten as:

$$c_{\ell k}(S) u_k(S) + \int_\Gamma p^*_{\ell k} u_k \, d\Gamma = \int_\Gamma u^*_{\ell k} p_k \, d\Gamma + \int_\Omega \sigma^0_{jk} \varepsilon^*_{ljk} \, d\Omega_0 \tag{2.18}$$

The last term in Eq. 2.18 is the initial stress term (BREBBIA, 1978), which is deduced in appendix A. Eq. 2.18 is defined as an integral equation in displacements (IED). From this equation, it is possible to determine the relationship between displacements and surface forces at a point within the boundary of the solid, as a function of the mechanical fields defined on the structure's boundary.

2.4 BEM algebraic system and representation for interior points

It is worth mentioning that BEM solves Eq. 2.11 and Eq. 2.12 accounting for approximations on the mechanical fields and geometry. In the present study, Lagrangian functions approximate these quantities. Particularly, quadrilateral linear isoparametric elements with continuous, discontinuous or edge-discontinuous collocation positions have been applied, Fig. 4. Then, $\psi^i(\xi_1,\xi_2)$ describes the geometric approximations, while $\phi^j(\xi_1,\xi_2)$ approximates the mechanical fields. The nodes i, located at the corners of the elements,

define the functions $\Psi^i(\xi_1,\xi_2)$, while the points j correspond to $\phi^j(\xi_1,\xi_2)$. These functions are described in more detail below:

$$\begin{aligned}\Psi^i(\xi_1,\xi_2) &= c_1^i + c_2^i\xi_1 + c_3^i\xi_2 + c_4^i\xi_1\xi_2 \\ \phi^j(\xi_1,\xi_2) &= c_1^j + c_2^j\xi_1 + c_3^j\xi_2 + c_4^j\xi_1\xi_2\end{aligned} \tag{2.19}$$

in which ξ_1 and ξ_2 represent the coordinates in the parent space.

The geometrical coefficients c^i have been assessed by simply enforcing the Kronecker delta property at the parametric nodal coordinates (ξ_1^i and ξ_2^i) as described in Eq. 2.20.

$$c_k^i \Rightarrow \phi^i(\xi_1^k,\xi_2^k) = \begin{cases} 1 \text{ for } k = i \\ 0 \text{ for } k \neq i \end{cases} \quad \text{for } i = 1...n \text{ nodes} \tag{2.20}$$

where n nodes represent the amount of element nodes.

Otherwise, the mechanical fields coefficients c^j have been determined by enforcing the Kronecker delta property at the parametric coordinates (ξ_1^j and ξ_2^j) of the collocations, as indicated in Eq. 2.21.

$$c_k^j \Rightarrow \phi^i(\xi_1^k,\xi_2^k) = \begin{cases} 1 \text{ for } k = j \\ 0 \text{ for } k \neq j \end{cases} \quad \text{for } j = 1...n \text{ collocation} \tag{2.21}$$

in which, n collocation represents the number of collocation points per element. For sake of simplicity $\bar{\xi} = 0.2$ is used in the present formulation. It is worth mentioning that discontinuous and edge-discontinuous boundary elements enable the collocations positions at smooth boundaries, which have unique normal vector. Then, these boundary element types enable the proper assessment of tractions in non-smooth surfaces. In the present study, the edge-discontinuous collocation scheme, Fig. 4b, has been used in elements along geometrical and mechanical fields discontinuities, such as corners, for instance. This strategy enables the unique mechanical fields values assessment at the collocation points. The discontinuous case has been utilised along the crack surface, Fig. 4c, whereas the continuous collocation scheme, Fig. 4a, discretises any condition different from the above-mentioned

Figure 4 – Continuous quadrilateral element, edge-discontinuous, discontinuous, respectively

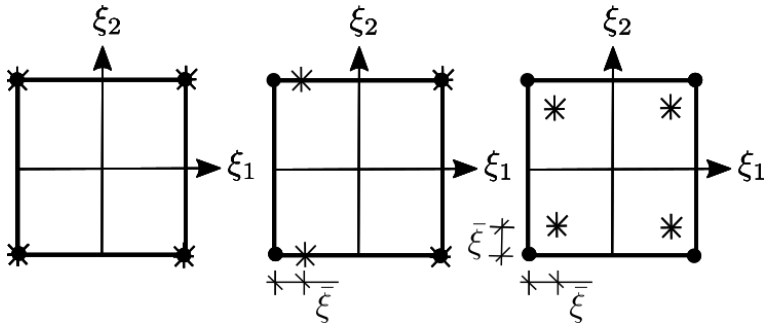

Source: The author.

The physical parameters of the problem (surface forces and displacements) are approximated through the adopted interpolation functions and their respective nodal values. The displacement and surface force values (u and p), are approximated by their nodal values (U and P):

$$\begin{aligned} u &= \phi^T U^n \\ p &= \phi^T P^n \end{aligned} \tag{2.22}$$

In its discretized form, Eq. 2.18 becomes:

$$\begin{aligned} c(S,t)u(S,t) = &- \sum_{J=1}^{J} \left[\int_{\Gamma_j} p^*(S,Q)\phi^T(Q)d\Gamma \right] U^n(Q,t) + \\ &+ \sum_{J=1}^{J} \left[\int_{\Gamma_j} u^*(S,Q)\phi^T(Q)d\Gamma \right] P^n(Q,t) \end{aligned} \tag{2.23}$$

The previously discussed approximations for geometry and mechanical fields enable the algebraic representation of Eq. 2.11 and Eq. 2.12. It is known that each node has three degrees of freedom, corresponding to three displacements and three surface forces. However, half of these values are imposed as boundary conditions, meaning the solution of the general system requires $3n$ equations. Writing the equations for all collocation points in the model leads to a system of equations with a size equal to three times the total number of nodes in the mesh. Thus, Eq. 2.11 can be expressed algebraically, disregarding the initial stress term, as:

$$HU = GP \tag{2.24}$$

H and G represent the BEM influence matrices, containing the integral kernels u^* and p^*, respectively, along the boundary Γ. After applying the boundary conditions, it is useful to rearrange the matrices H and G to obtain the final algebraic system. Following this

procedure, a system of the form $Ax = b$ is derived, where A incorporates the contributions from both H and G, x contains the unknown coefficients, and b represents the result of multiplying the influence matrices by the known boundary conditions.

In addition, Eq. 2.11 allows the evaluation of displacements at internal points, when c_{ij} is equal to the identity matrix. In this condition, the algebraic representation can be described as follows:

$$u_i + HU = GP \tag{2.25}$$

where, u_i is the vector of displacements at internal nodes.

Finally, the algebraic representation for Eq. 2.12, which brings the stress field to internal points, is written in the form:

$$\sigma_i + H^{'}U = G^{'}P \tag{2.26}$$

where, $H^{'}$ and $G^{'}$ contain the influence terms associated with the integral kernels S^*_{kij} and D^*_{kij}, respectively.

Despite the singularities involved in fundamental solutions, their evaluation is regular at internal points, Eq. 2.25 and Eq. 2.26. Thus, in these cases, the conventional Gauss-Legendre quadrature can be used. In cases where the source point is coincident with the integration element, the boundary integrals are singular. For this case, u^* has a weak singularity of order $O(1/r)$ and p^* has a strong singularity of order $O(1/r^2)$. The strong singular kernel is efficiently regularized with the singularity subtraction technique proposed by Guiggiani and Gigante (1990), Guiggiani *et al.* (1992).

3 NONLINEAR FRACTURE MECHANICS

3.1 The Cohesive Model

The NLFM theory offers various approaches for describing properly the mechanical behaviour along the FPZ in materials subjected to large extensions of this zone. One effective approach in this context is the cohesive model, in which a fictitious crack describes geometrically the FPZ whereas cohesive laws govern the residual material resistance and the energy dissipation phenomena into this zone. The residual material resistance along the FPZ can be represented by cohesive stresses, which tend to close the crack surfaces. Usually, cohesive laws relate the cohesive stresses intensity, $\sigma_{criterion}$, to the crack opening displacement values,w.

Various cohesive laws have been presented in the literature (ZHU; LIN; LI, 2013) for modelling the complex material behaviour along the FPZ. However, three of them have been applied often for crack propagation modelling in quasi-brittle material (ZHU; LIN; LI, 2015). The linear cohesive law is the largest and simplest applied, in which a linear function associates cohesive stresses and crack opening displacement values. The crack opening displacements larger than lead to the nil cohesive stresses, Fig. 5. The governing equations for this cohesive law are as follows:

$$\begin{aligned} &\sigma_{criterion}(w) = f_t\left(1 - \frac{w}{w_c}\right) \quad \text{if} \quad 0 <= w <= w_c \\ &\sigma_{criterion}(w) = 0 \quad \text{if} \quad w > w_c \end{aligned} \tag{3.1}$$

in which f_t indicates the tensile material strength value.

Similarly, cohesive stresses and crack opening displacement values can be associated by a bilinear function, as illustrated in Fig. 5b. This approach leads to the bilinear cohesive law, which has the following governing equations (LEONEL; VENTURINI, 2010):

$$
\begin{aligned}
&\sigma_{criterion}(w) = f_t - \left(\frac{f_t - f_f^{''}}{w^{''}}\right) w \quad \text{if} \quad 0 <= w <= w^{''} \\
&\sigma_{criterion}(w) = \frac{f_t^{''} w}{w^{''} - w_c} + \sigma_t^{''}\left(1 - \frac{w^{''}}{w^{''} w_c}\right) \quad \text{if} \quad w^{''} <= w <= w_c \\
&\sigma_{criterion}(w) = 0 \quad \text{if} \quad w > w_c
\end{aligned}
\tag{3.2}
$$

where $f_t^{''}$, $w^{''}$ and w_c are as follows:

$$
\begin{aligned}
f_t^{''} &= \frac{f_t}{3} \\
w^{''} &= \frac{0.8\, G_f}{f_t} \\
w_c &= \frac{3.6\, G_f}{f_t}
\end{aligned}
\tag{3.3}
$$

in which G_f indicates the material fracture energy

Finally, an exponential function associates the cohesive stresses and the crack opening displacements values in the exponential cohesive law, Fig. 5c. The governing equations for this cohesive law are as follows:

$$
\sigma_{criterion}(w) = f_t e^{-(f_t/G_f)w} \quad \text{if} \quad w > 0 \tag{3.4}
$$

Figure 5 – Classic cohesive laws. (a) linear; (b) bilinear; (c) exponential

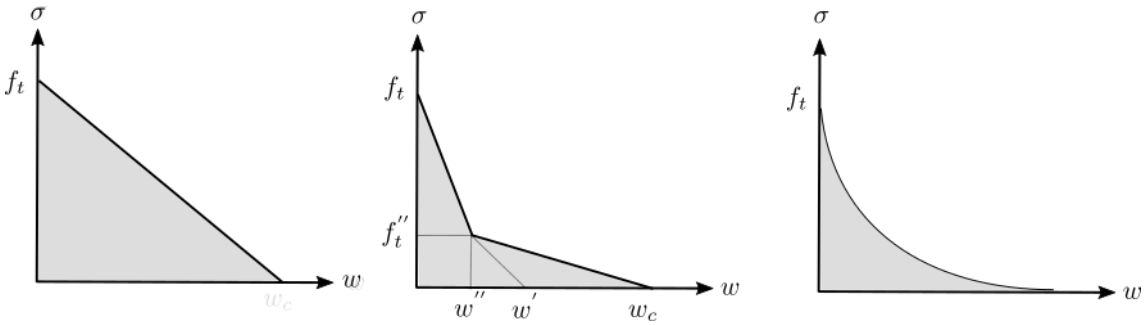

Source: The author.

It is important mentioning that the cohesive laws adopted herein solely penalise the material strength along mode I. Thus, tangential fracture energies associated to mode II and III has been neglected and the material has been assumed as perfectly brittle for modes II and III. On the opposite, the PPR CZM, which will be presented in section 5.1, is a more suitable and comprehensive model that penalizes material strength along tangential modes.

3.2 BEM Integral Equations for Dipole Formulation

This study proposes an alternative BEM formulation for handling cohesive crack propagation modelling in three-dimensional structures. This formulation requires the manipulation of the domain term from the classical BEM integral equation, Eq. 2.11, for representing the mechanical behaviour along the FPZ. Thus, such term is non-nil solely at the FPZ, which reduces its dimension by one. Therefore, the domain term degenerates to an additional boundary term, which assesses solely the FPZ boundaries. This manipulation triggers the dipoles of stresses variable, which appear as a consequence of the domain term dimension reduction.

For sake of completeness, the proposed formulation initially describes the FPZ as a narrow domain positioned in front of the crack tip. This narrow zone has boundary $\bar{\Gamma}$, which may be splitted into Γ_1^c and Γ_2^c. Thus, $\bar{\Gamma} = \Gamma_1^c \cup \Gamma_2^c$. Besides, the thickness of this region is $2a$, which has been assumed as small in comparison to its length. It is worth mentioning that the dipoles appear in the limit of $2a \Rightarrow 0$, as demonstrated in the following, Fig. 6. Then, the crack can be represented either as a curve in 2D problems, Fig. 6b, or a surface in 3D cases, Fig. 6a. In this study, the 3D representation has been employed. Besides, Fig. 6c presents the crack's boundaries and Γ^c is the crack's middle path. When the limit of $2a \Rightarrow 0$ is enforced, the discontinuity is represented by its middle surface Γ^c, and $\bar{\Gamma} = \Gamma_c$. For sake of clarity, Ω_0 indicates the material nonlinear zone.

The numerical developments in the following assume the crack, and consequently the FPZ, positioned in accordance with the illustration in Fig. 7. Nevertheless, randomly positioned cracks can be handled straightforwardly by enforcing a rotation into the coordinate system. The proper rotation is also presented in the following

The starting point of the proposed formulation is the classical BEM integral equation, Eq. 2.11, which accounts for a domain Ω with boundary Γ. The domain term can include the presence of an initial stress field σ_{jk}^0, as suggested by (BREBBIA; DOMINGUEZ, 1994)

$$c_{lk}u_k + \int_\Gamma p_{lk}^* u_k \, d\Gamma = \int_\Gamma u_{lk}^* p_k \, d\Gamma + \int_\Omega \sigma_{jk}^0 \varepsilon_{ljk}^* \, d\Omega_0 \tag{3.5}$$

where Ω_0 represents the domain of non-nil values of σ_{jk}^0 , i.e., the FPZ as illustrated in Fig. 6. ε_{ljk}^* indicates the fundamental solution for strain. It is worth mentioning that the domain term presented in Eq. 3.5 contains the initial stress field, This term will be manipulated in order to provide the correct stresses values required in the material nonlinear modelling

Firstly, the fundamental strains can be rewritten in terms of the displacement derivatives as follows:

Figure 6 – FPZ. Initial stress region

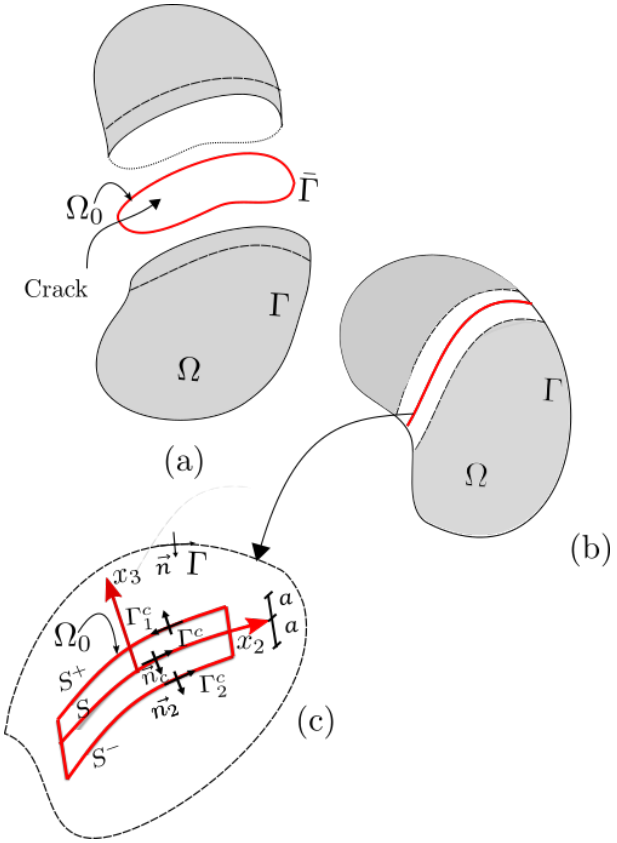

Source: The author.

Figure 7 – Crack orientation

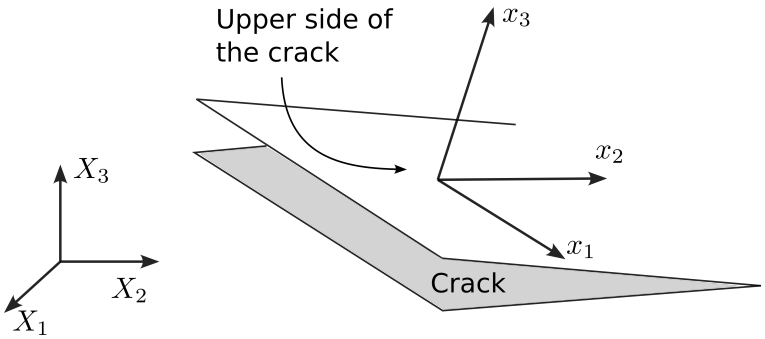

Source: The author.

$$\sigma_{jk}^0 \varepsilon_{ljk}^* = \sigma_0^{jk} u_{lj,k}^* \Rightarrow \int_{\Omega_0} \sigma_{jk}^0 \varepsilon_{ljk}^* d\Omega_0 = \int_{\Omega_0} \sigma_{jk}^0 \frac{\partial u_{lj}^*}{\partial x_k} d\Omega_0 \tag{3.6}$$

Then, the integration by parts of Eq. 3.6 leads to the following:

$$\begin{aligned} &\int_{\Omega_0} \sigma_{jk}^0 \frac{\partial u_{lj}^*}{\partial x_k} d\Omega_0 = \int_{\Gamma^c} u_{ij}^* \sigma_{jk}^0 \eta_k d\Gamma^c - \int_{\Omega_0} u_{ij}^* \sigma_{jk,k}^0 d\Omega_0 \Rightarrow \\ &\int_{\Omega_0} \sigma_{jk}^0 \frac{\partial u_{lj}^*}{\partial x_k} d\Omega_0 = \int_{\Gamma^c} u_{ij}^* p_j^0 \eta_k d\Gamma^c - \int_{\Omega_0} u_{ij}^* \sigma_{jk,k}^0 d\Omega_0 \end{aligned} \tag{3.7}$$

where $p_j^0 = \sigma_{jk}^0 \eta_k$ represents the tractions at the narrow region boundary associated to the FPZ.

The integral terms on Eq. 3.7 must be handled in separate form. Besides, the points at Γ_1^c have been indicated as S^+ whereas the points at Γ_2^c have been identified as S^-. Thus, the first integral term on right hand side of Eq. 3.7 can be rewritten as follows:

$$\int_{\Gamma^c} u_{ij}^* p_j^0 d\Gamma^c = \int_{\Gamma_1^c} u_{ij}^*(p,S^+) p_j^0(S^+) d\Gamma_1^c + \int_{\Gamma_2^c} u_{ij}^*(p,S^-) p_j^0(S^-) d\Gamma_2^c \tag{3.8}$$

where p is a point defined between Γ_1^c and Γ_2^c. It is worth stressing that direction x_3 is perpendicular to the crack surfaces. In addition, one assumes the thickness of the nonlinear region, $2a$, small in comparison to its length. Therefore, in such case, the displacements at the FPZ boundaries are smooth enough and can be redefined using a Taylor's expansion as follows:

$$\begin{aligned} u_{ij}^*(p,S^+) &= u_{ij}^*(p,S) + \frac{\partial u_{lj}^*(p,S)}{\partial x_3} a \\ u_{ij}^*(p,S^-) &= u_{ij}^*(p,S) - \frac{\partial u_{lj}^*(p,S)}{\partial x_3} a \end{aligned} \tag{3.9}$$

Because $2a$ is small and the displacements are smooth at the FPZ, the displacements can be redefined at the middle path of the FPZ. Therefore, Eq. 3.8 has been rewritten as follows:

$$\begin{aligned} \int_{\Gamma^c} u_{ij}^* p_j^0 d\Gamma^c = \int_{-\Gamma^c} \left[u_{ij}^*(p,S) - \frac{\partial u_{lj}^*(p,S)}{\partial x_3} a \right] p_j^{03}(S) d\Gamma^c + \\ \int_{\Gamma^c} \left[u_{ij}^*(p,S) + \frac{\partial u_{lj}^*(p,S)}{\partial x_3} a \right] p_j^{03}(S) d\Gamma^c \Rightarrow \\ \int_{\Gamma^c} u_{ij}^* p_j^0 d\Gamma^c = \int_{\Gamma^c} 2a \frac{\partial u_{lj}^*(p,S)}{\partial x_3} p_j^{03}(S) d\Gamma^c \end{aligned} \tag{3.10}$$

Complementarily, the domain term on the right hand side of Eq. 3.7 can be handled properly. The derivatives of the initial stress field are as follows:

$$\sigma_{jk,k}^0 = \frac{\partial \sigma_{jk}^0}{\partial X_k} = \frac{\partial \sigma_{j1}^0}{\partial X_1} + \frac{\partial \sigma_{j2}^0}{\partial X_2} + \frac{\partial \sigma_{j3}^0}{\partial X_3} \tag{3.11}$$

The derivative terms on Eq. 3.11 can be rewritten accounting for the local coordinate system x_j instead of the global coordinate system X_j. Thus, one applies the chain rule on terms of Eq. 3.11. It is worth mentioning that the derivatives along x_3 are nil because $2a$ has been assumed as small. Therefore, σ_{jk}^0 is constant along that direction. Then:

$$\sigma^0_{jk,k} = \frac{\partial \sigma^0_{j1}}{\partial x_1}\frac{\partial x_1}{\partial X_1} + \frac{\partial \sigma^0_{j1}}{\partial x_2}\frac{\partial x_2}{\partial X_1} + \frac{\partial \sigma^0_{j2}}{\partial x_1}\frac{\partial x_1}{\partial X_2} + \frac{\partial \sigma^0_{j2}}{\partial x_2}\frac{\partial x_2}{\partial X_2} + \frac{\partial \sigma^0_{j3}}{\partial x_1}\frac{\partial x_1}{\partial X_3} + \frac{\partial \sigma^0_{j3}}{\partial x_2}\frac{\partial x_2}{\partial X_3} \Rightarrow$$
$$\sigma^0_{jk,k} = \frac{\partial \sigma^0_{j1}}{\partial x_1}m_1 + \frac{\partial \sigma^0_{j1}}{\partial x_2}s_1 + \frac{\partial \sigma^0_{j2}}{\partial x_1}m_2 + \frac{\partial \sigma^0_{j2}}{\partial x_2}s_2 + \frac{\partial \sigma^0_{j3}}{\partial x_1}m_3 + \frac{\partial \sigma^0_{j3}}{\partial x_2}s_3 \tag{3.12}$$

As a result, the domain integral term on the right hand side of Eq. 3.7 is as follows:

$$\int_{\Omega_0} u^*_{ij}\sigma^0_{jk,k}d\Omega_0 = \int_{\Omega_0} u^*_{ij}\left[\frac{\partial}{\partial x_1}(\sigma^0_{jk}m_k) + \frac{\partial}{\partial x_2}(\sigma^0_{jk}s_k)\right]dx_1dx_2dx_3 \tag{3.13}$$

m_k and s_k are the cosines with normal direction. The last equation can be simplified bearing in mind that the distance between the crack surfaces is constant, small and equal to $2a$. Thus:

$$\int_{\Omega_0} u^*_{ij}\sigma^0_{jk,k}d\Omega_0 = \iint_{\Gamma_c} u^*_{ij}\frac{\partial}{\partial x_1}(\sigma^0_{jk}m_k)2adx_1dx_2 + \iint_{\Gamma_c} u^*_{ij}\frac{\partial}{\partial x_2}(\sigma^0_{jk}s_k)2adx_1dx_2 \tag{3.14}$$

In addition, the last equation can be further modified by integrating by parts its terms as follows:

$$\begin{aligned}\iint_{\Gamma_c} u^*_{ij}\frac{\partial}{\partial x_1}(\sigma^0_{jk}m_k)2adx_1dx_2 &= u^*_{ij}\sigma^0_{jk}m_k2a(x^2_1 - x^1_1) - \int_{\Gamma_c}\frac{\partial u^*_{ij}}{\partial x_1}\sigma^0_{jk}m_k2ad\Gamma^c \\ \iint_{\Gamma_c} u^*_{ij}\frac{\partial}{\partial x_2}(\sigma^0_{jk}s_k)2adx_1dx_2 &= u^*_{ij}\sigma^0_{jk}s_k2a(x^2_1 - x^1_1) - \int_{\Gamma_c}\frac{\partial u^*_{ij}}{\partial x_2}\sigma^0_{jk}s_k2ad\Gamma^c\end{aligned} \tag{3.15}$$

It is worth mentioning that the constant terms on right hand side of Eq. 3.15 become nil for coincident crack surfaces. Such assumption is usual in fracture mechanics and results in the classical Griffiths' crack. Besides, it can be achieved in the limit of $2a \Rightarrow 0$. Thus:

$$\begin{aligned}\int_{\Omega_0} u^*_{ij}\sigma^0_{jk,k}d\Omega_0 &= -\int_{\Gamma_c}\frac{\partial u^*_{ij}}{\partial x_1}\sigma^0_{jk}m_k2ad\Gamma^c - \int_{\Gamma_c}\frac{\partial u^*_{ij}}{\partial x_2}\sigma^0_{jk}s_k2ad\Gamma^c \Rightarrow \\ \int_{\Omega_0} u^*_{ij}\sigma^0_{jk,k}d\Omega_0 &= -\int_{\Gamma_c} 2a\frac{\partial u^*_{ij}}{\partial x_1}p^{01}_j d\Gamma^c - \int_{\Gamma_c} 2a\frac{\partial u^*_{ij}}{\partial x_2}p^{02}_j 2ad\Gamma^c \Rightarrow\end{aligned} \tag{3.16}$$

The previous developments lead to two main results, which have been presented in Eq. 3.10 and Eq. Eq. 3.16. Such developments enable rewriting the domain term of Eq. Eq. 3.5 as follows:

$$\begin{aligned}\int_{\Omega_0}\sigma^0_{jk}\varepsilon^*_{ljk}\,d\Omega_0 = \int_{\Gamma^c} 2a\frac{\partial u^*_{lj}}{\partial x_1}p^{01}_j d\Gamma^c - (-\int_{\Gamma^c} 2a\frac{\partial u^*_{lj}}{\partial x_2}p^{02}_j d\Gamma^c - \int_{\Gamma^c} 2a\frac{\partial u^*_{lj}}{\partial x_3}p^{03}_j d\Gamma^c \\ \sigma^0_{jk}\varepsilon^*_{ljk}\,d\Omega_0 = \int_{\Gamma^c} 2a\frac{\partial u^*_{lj}}{\partial x_l}p^{0l}_j d\Gamma^c\end{aligned} \tag{3.17}$$

It is worth emphasizing that the integral terms on Eq. 3.21 have been defined into the local coordinate system, x_l . Nevertheless, the solution of general cohesive crack growth problems requires the evaluation of such terms into the global coordinate system, X_l. Therefore, general mixed mode cohesive crack growth problems require a coordinate system transformation, which can be achieved through the simply application of chain rule as follows:

$$\frac{\partial u^*_{lj}}{\partial x_l} p^{0l}_j = \frac{\partial u^*_{lj}}{\partial X_m} \frac{\partial X_m}{\partial x_l} p^{0l}_j \tag{3.18}$$

in which the following additional cosines between global and local systems are as follows:

$$\overline{m}_l = \frac{\partial X_1}{\partial x_l} \overline{s}_l = \frac{\partial X_2}{\partial x_l} \overline{n}_l = \frac{\partial X_3}{\partial x_l} \tag{3.19}$$

Therefore, the traction values defined into global coordinates are as follows:

$$\overline{p}^{0m}_j = T_{ml} p^{0l}_j \tag{3.20}$$

em que $T_{ml} = \begin{bmatrix} \overline{m}_1 & \overline{m}_2 & \overline{m}_3 \\ \overline{s}_1 & \overline{s}_2 & \overline{s}_3 \\ \overline{n}_1 & \overline{n}_2 & \overline{n}_3 \end{bmatrix}$ e $p^{0l}_j = \begin{bmatrix} p^{01}_j \\ p^{02}_j \\ p^{03}_j \end{bmatrix}$.

Thus, Eq. 3.21 can be defined into global coordinates as follows:

$$\int_{\Omega_0} \sigma^0_{jk} \varepsilon^*_{ljk} \, d\Omega_0 = \int_{\Gamma^c} 2a \frac{\partial u^*_{lj}}{\partial x_l} p^{0l}_j d\Gamma^c = \int_{\Gamma^c} 2a \frac{\partial u^*_{lj}}{\partial X_l} \overline{p}^{0l}_{jd} \Gamma^c \tag{3.21}$$

The cohesive problem could be solved by any numerical scheme accounting for the definition of a thin FPZ. However, in such case, the nonlinear zone must be wide enough to guarantee finite values of initial stresses, which is not the real representation of the problem. Besides, singular initial stresses appear along the FPZ when its thickness goes to zero, which is explained straightforwardly by the nature of the problem.

Nevertheless, the thickness of the FPZ can be assumed as nil and the integral terms on Eq. 3.21 can be evaluated since a new tensor variable be defined. This tensor is named as dipole, q, which can be defined as follows:

$$q^l_j = 2a \overline{p}^{0l}_j \tag{3.22}$$

The dipoles are sets of self-equilibrated stresses, which superpose the stress state associated to the external loading at the FPZ. This superposition of stresses corrects the mechanical behaviour within a constitutive law, as those presented in the previous section. Thus, material nonlinear behaviour can be modelled with this approach. The dipoles have

been included in the BEM integral equations by its domain integral term once the material nonlinearity is at the domain. Besides, this new tensor variable provides finite values. When $2a \Rightarrow 0$, the forces inside the FPZ tends to infinity. Thus, the quantity dipole keeps the physical meaning of stresses within the FPZ.

The dipoles components have been illustrated in Fig. 8.

Figure 8 – Dipoles representation

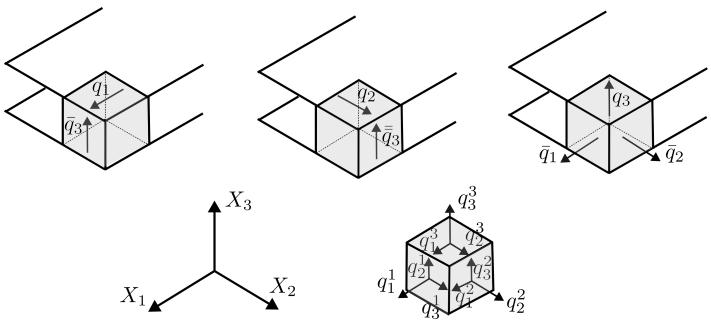

Source: The author.

Therefore, from the integral terms illustrated in Eq. 3.21, one defines a new integral kernel for representing the mechanical behaviour along the FPZ, which has been defined as follows:

$$\sigma^0_{jk}\varepsilon^*_{ljk}\, d\Omega_0 = \int_{\Gamma^c} 2a \frac{\partial u^*_{lj}}{\partial X_l} \bar{p}^{0l}_j d\Gamma^c = \int_{\Gamma^c} G^l_{lj} q^l_j \Gamma^c \tag{3.23}$$

where $G^l_{lj} = \frac{\partial u^*_{lj}}{\partial X_l}$

For sake of conciseness, the component terms of the kernel G^l_{lj} have been demonstrated in details in appendix B whereas its explicit representation is as follows:

$$G^l_{ij} = \frac{1}{16\pi\mu r^2}(1-v)\{-(3-4v)r_{,l}\delta_{lj} + r_{,j}\delta_{li} + r_l\delta_{lj} - 3r_{,i}r_{,l}r_{,j}\} \tag{3.24}$$

in which δ is the Kronecker delta and $r_{,i}$ are the distance derivatives between source and field points.

Therefore, Eq. 3.5 can be rewritten in the following form after the manipulations on the domain term previously presented:

$$c_{lk}u_k + \int_\Gamma p^*_{lk}u_k\, d\Gamma = \int_\Gamma u^*_{lk}p_k\, d\Gamma + \int_{\Gamma^c} G^l_{ij} q^l_j d\Gamma^c \tag{3.25}$$

The last equation enables the solution of the boundary value problem accounting for the material nonlinear effects at the FPZ.

3.3 Algebraic descriptions and Dipoles simplifications

The previous section demonstrates the entire manipulation procedures in the domain integral term containing an initial stress field, which lead to the dipoles of stresses. Thus, nine dipole components arise along the FPZ, Ω_0, as illustrated in Fig. 8. However, the cohesive modelling by the proposed formulation still requires further manipulations in such term. The first additional manipulation involves the evaluation of dipole terms at the crack surfaces, i.e., traction determination. In the classic cartesian form (BREBBIA; DOMINGUEZ, 1994), the stress values at the boundary can be associated to the strains components as follows:

$$\begin{aligned} \sigma_{11} &= \frac{1}{1-v}\left[v\sigma_{33} + 2\mu\left(\varepsilon_{11} + v\varepsilon 22\right)\right] \qquad \sigma_{12} = 2\mu\varepsilon_{12} \\ \sigma_{22} &= \frac{1}{1-v}\left[v\sigma_{33} + 2\mu\left(\varepsilon_{22} + v\varepsilon 11\right)\right] \qquad \sigma_{23} = p_2 \\ \sigma_{13} &= p_1 \qquad \sigma_{33} = p_3 \end{aligned} \tag{3.26}$$

in which the stress values have been illustrated in Fig. 9. ε_{ij} are the strains. μ is the transversal modulus. X_3 contains the normal crack surface direction and p_i indicates the tractions at the crack surface.

Figure 9 – Stress components at the crack surface

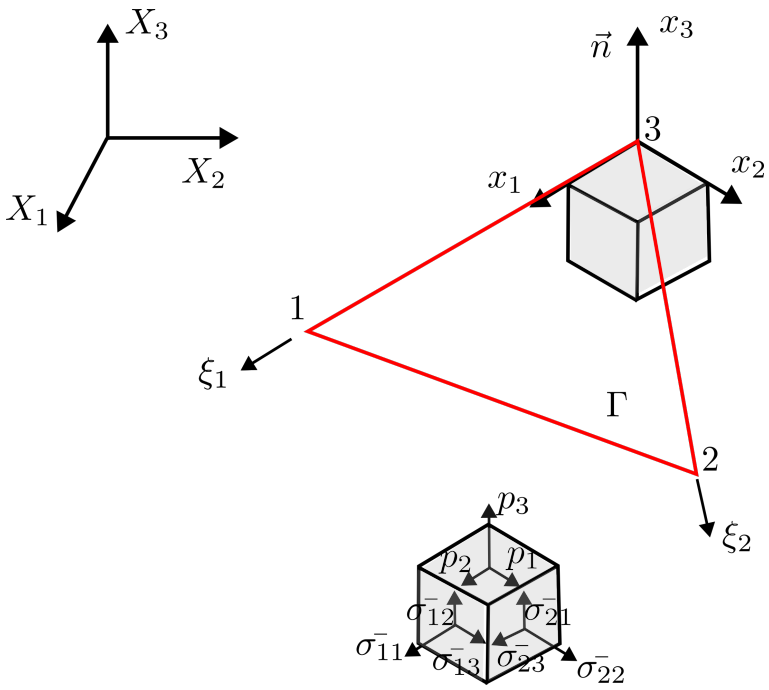

Source: The author.

The cohesive model represents the residual material strength at the FPZ by cohesive

stresses, which close smoothly the crack surfaces. Besides, these cohesive stresses model the residual strength for mode I fracture. Because of this cohesive modelling assumption, one assumes that the normal strains along the crack surfaces planes triggered by the dipoles are nil. Then, if $\varepsilon_{11} = \varepsilon_{22} = 0$, the normal stresses at the crack surfaces are as follows:

$$\begin{aligned} \sigma_{11} &= \frac{v}{1-v}\sigma_{33} \\ \sigma_{22} &= \frac{v}{1-v}\sigma_{33} \end{aligned} \tag{3.27}$$

It is worth mentioning that the dipoles on direction 3 trigger strains along directions 1, 2 and 3. The Hooke's law enables the straightforward determination of such strain values. Nevertheless, the normal strains at the crack surface planes can be avoided by enforcing additional dipoles $\overline{q}_1$ and $\overline{q}_2$, as illustrated in Fig. 8. Besides, the dipoles q_1 and q_2 require associated dipoles $\overline{q}_3$ and $\overline{\overline{q}}_3$, respectively. Thus, the additional dipoles components for obeying the compatibility conditions are as follows:

$$\begin{array}{lll} q_1^1 = \overline{q}_1^1 & q_2^1 = 0 & q_3^1 = \overline{q}_3 \\ q_1^2 = 0 & q_2^2 = \overline{q}_2 & q_3^2 = \overline{q}_3 \\ q_1^3 = q_1 & q_2^3 = q_2 & q_3^3 = q_3 \end{array} \tag{3.28}$$

Therefore, the terms on Eq. 3.28 correspond to the terms on Eq. 3.26 for representing the mechanical behaviour of quasi-brittle materials at the FPZ. Then:

$$q_3^1 = q_1^3 \qquad q_3^2 = q_2^3 \qquad q_1^1 = \frac{v}{1-v}q_3^3 \qquad q_2^2 = \frac{v}{1-v}q_3^3 \tag{3.29}$$

The correspondences presented in Eq. 3.29 enable the compact algebraic description of dipoles along the FPZ. Thus, the fully independent dipole description has been presented in Eq. 3.30, in which 9 independent components appear:

$$\begin{bmatrix} G_{l1}^1 & G_{l2}^1 & G_{l3}^1 & G_{l1}^2 & G_{l2}^2 & G_{l3}^2 & G_{l1}^3 & G_{l2}^3 & G_{l3}^3 \end{bmatrix} \begin{bmatrix} q_1^1 \\ q_2^1 \\ q_3^1 \\ q_1^2 \\ q_2^2 \\ q_3^2 \\ q_1^3 \\ q_2^3 \\ q_3^3 \end{bmatrix} \tag{3.30}$$

The description presented in Eq. 3.30 reduces to three accounting for the correspondences of Eq. 3.29. Then, Eq. 3.30 can be rewritten as follows:

$$\begin{bmatrix} G^1_{l1} + G^3_{l1} & G^2_{l3} + G^3_{l2} & \frac{v}{1-v}\left(G^1_{l1} + G^2_{l2}\right) + G^3_{l3} \end{bmatrix} \begin{bmatrix} q^3_1 \\ q^3_2 \\ q^3_3 \end{bmatrix} \tag{3.31}$$

Therefore, the kernel G^l_{ij} in its condensed algebraic form has been illustrated in Eq. 3.31. Such kernel can be algebraically represented in Eq. 3.32, in which the index varies from 1 to 3 as follows:

$$\begin{bmatrix} K_{11} & K_{12} & K_{13} \\ K_{21} & K_{22} & K_{23} \\ K_{31} & K_{32} & K_{13} \end{bmatrix} \begin{bmatrix} q^3_1 \\ q^3_2 \\ q^3_3 \end{bmatrix} \tag{3.32}$$

The algebraic form illustrated in Eq. 3.31 couples to the classical and BEM matrices for the solution of the boundary value problem. For sake of conciseness, the shape function expressions have been presented in section 2.4.

3.4 Dipoles Contribution to the Crack Openings

The cohesive crack model utilises cohesive stresses for representing the residual material strength at the FPZ. Besides, the intensities of such stresses are function of the crack opening displacements. This dependence triggers a nonlinear problem, in which the crack openings depend on the cohesive stresses values. The proposed formulation achieves the crack opening displacement values via Eq. 3.25. Particularly, by analysing the last integral term on its right hand side. This term has to be evaluated for points symmetrically positioned at $\Gamma^c_1(S^+)$ and $\Gamma^c_2(S^-)$, as illustrated in Fig. 6. Afterwards, the limit of $2a \Rightarrow 0$ leads to the representation of these surfaces at its mean path. The enforcement of this limit requires the proper description of the boundaries Γ^c_1 and Γ^c_2 by the angles on planes X_1X_3 and X_2X_3. Thus, this procedure leads to two displacement representations, which enable the crack openings by simply subtracting them. Then:

$$\{\Delta w\} = \begin{Bmatrix} \Delta w_1 \\ \Delta w_2 \\ \Delta w_3 \end{Bmatrix} \begin{bmatrix} \frac{1}{\mu} & 0 & 0 \\ 0 & \frac{1}{\mu} & 0 \\ 0 & 0 & \frac{1-2v}{2(1-v)\mu} \end{bmatrix} \begin{bmatrix} q^3_1 \\ q^3_2 \\ q^3_3 \end{bmatrix} \tag{3.33}$$

It is worth stressing that the crack opening displacement for mode I is Δw_3 . Thus, the cohesive law must be applied accounting for such term. Besides, these responses agree

with the procedures presented in Oliveira and Leonel (2013), in which the approach has been applied within 2D problems.

3.5 The Influence of Dipoles on the Stress Field

The last sections demonstrate the mechanical influence of the dipoles of stresses on the boundary values and on the crack opening displacements. In addition, the dipoles influence the stresses values out of the FPZ. Such an influence can be measured through the following classical elasticity relations:

$$\begin{aligned} \sigma_{lm} &= \lambda\delta_{lm}\varepsilon_{kk} + 2\mu\varepsilon_{lm} \quad \text{and} \quad \varepsilon_{lm} = \frac{1}{2}\left(\frac{\partial u_l}{\partial X_m} + \frac{\partial u_m}{\partial X_l}\right) \\ \sigma_{lm} &= \lambda\delta_{lm}\frac{\partial u_k}{\partial X_k} + \mu\left(\frac{\partial u_l}{\partial X_m} + \frac{\partial u_m}{\partial X_l}\right) \end{aligned} \tag{3.34}$$

in which λ indicates the Lamé parameter

The last equation can be rewritten accounting for the displacement expression presented in Eq. 3.25. Thus:

$$\begin{aligned} \sigma_{lm} = -\int_\Gamma S_{lmj}u_j d\Gamma + \int_\Gamma D_{lmj}p_j\Gamma + \\ \left\{\lambda\delta_{lm}\frac{\partial}{\partial X_k}\int_{\Gamma^c} G^l_{kj}q^l_j\Gamma^c + \mu\frac{\partial}{\int_{\Gamma^c}} G^l_{ij}q^l_j d\Gamma^c + \mu\frac{\partial}{\partial}X_l\int_{\Gamma^c} G^l_{mj}q^l_j d\Gamma^c\right\} \end{aligned} \tag{3.35}$$

The classical tensors S_{lmj} and D_{lmj} have been presented in Eq. 2.13. Nevertheless, the remaining terms account for the dipoles influence. Such terms require the derivative process, which is presented in details in appendix C. This procedure leads to the following:

$$\{...\} = \int_{\Gamma^c} G^{ml}_{ij}q^l_j d\Gamma^c + g^{ml}_{lj}\left[\sigma_{jl}(p)\right] \tag{3.36}$$

in which:

$$G^{ml}_{ij} = \frac{1}{8\pi(1-v)r^3}\left\{\begin{array}{c} (1-2v)\left(\delta_{mj}\delta_{il} + \delta_{ij}\delta_{lm} - \delta_{mi}\delta_{lj}\right) + \\ 3(1-2v)\left(\delta_{mj}r_{,i}r_{,l} + \delta_{ij}r_{,m}r,l - \delta_{im}r_{,j}r_{,l}\right) - \\ 3\left(\delta_{lj}r_{,i}r_{,m} + \delta_{ml}r_{,j}r,i + \delta_{il}r_{,m}r_{,j}\right) - 15r_{,i}r_{,j}r_{,m}r_{,l} \end{array}\right\} \tag{3.37}$$

com

$$g^{ml}_{ij} = \left|\begin{array}{ll} 0 & \text{if outside the cohesive zone} \\ \sigma^0_{im} & \text{inside the cohesive zone} \end{array}\right| \tag{3.38}$$

where g_{ij}^{ml} is the free term, which arises from the algebraic manipulation (integrations) of the hyper singular kernel. This term is nil once rigid body movements have been avoided in the material nonlinear modelling.

Therefore, Eq. 3.35 updates the elastic stress field, with dipoles terms as follows:

$$\sigma_{lm} = -\int_{\Gamma} S_{lmj} u_j d\Gamma + \int_{\Gamma} D_{lmj} p_j \Gamma + \int_{\Gamma^c} G_{ij}^{ml} q_j^l d\Gamma^c + g_{lj}^{ml} \left[\sigma_{jl}(p)\right] \tag{3.39}$$

The dipoles terms lead to the following complete algebraic representation:

$$\begin{bmatrix} G_{l1}^{m1} & G_{l2}^{m1} & G_{l3}^{m1} & G_{l1}^{m2} & G_{l2}^{m2} & G_{l3}^{m2} & G_{l1}^{m3} & G_{l2}^{m3} & G_{l3}^{m3} \end{bmatrix} \begin{bmatrix} q_1^1 \\ q_2^1 \\ q_3^1 \\ q_1^2 \\ q_2^2 \\ q_3^2 \\ q_1^3 \\ q_2^3 \\ q_3^3 \end{bmatrix} \tag{3.40}$$

Nevertheless, the complete representation above can be simplified by the strain assumptions at the crack surface, which have simplified Eq. 3.26 into Eq. 3.31. Such assumptions enable rewriting the last equation as follows:

$$\begin{bmatrix} G_{l1}^{m1} + G_{l1}^{m3} & G_{l3}^{m2} + G_{l2}^{m3} & \frac{v}{1-v}\left(G_{l1}^{m1} + G_{l2}^{m2}\right) + G_{l3}^{m3} \end{bmatrix} \begin{bmatrix} q_1^3 \\ q_2^3 \\ q_3^3 \end{bmatrix} \tag{3.41}$$

Finally, the values from the kernel G_{ij}^{ml} can be condensed into a matrix, as follows:

$$\begin{bmatrix} KS_{11}^m & KS_{12}^m & KS_{13}^m \\ KS_{21}^m & KS_{22}^m & KS_{23}^m \\ KS_{31}^m & KS_{32}^m & KS_{33}^m \end{bmatrix} \begin{bmatrix} q_1^3 \\ q_2^3 \\ q_3^3 \end{bmatrix} \tag{3.42}$$

in which m varies from 1 to 3, which lead to the 9 stress components.

3.6 Algebraic Problem Representation

The last sections described the manipulation procedures into the domain integral term of BEM integral equations for modelling stresses and displacements discontinuities at the FPZ accounting for initial stresses fields. These procedures lead to the additional

kernels G^{l}_{ij}, for boundary value problem, and G^{ml}_{ij}, for stresses values, which must be evaluated along the FPZ boundary.

The algebraic representation of these integral kernels has been obtained after the approximation of geometry and mechanical fields by shape functions, as usual in BEM. In this study, Lagrangian polynomial basis functions approximate these quantities, which have been detailed in section 2.4. Thus, the boundary discretisation leads to the well-known H and G matrices, Eq. 2.24, which account for boundary displacements and tractions. $H^{'}$ and $G^{'}$ contain the influence terms associated to the integration of S^{*}_{klj} kernels and D^{*}_{klj}, respectively. The dipoles terms associate to K, for boundary value problem, and KS , for stresses values. Therefore, Eq. 3.25 and Eq. Eq. 3.39 assume the following algebraic representations:

$$HU = GP + KQ \tag{3.43}$$

$$\sigma + H^{'}U = G^{'}P + KSQ \tag{3.44}$$

in which K and KS matrices contain the influence terms associated to the dipoles Q .

The nonlinear problem solution requires manipulations on Eq. 3.43 and Eq. 3.44. Initially, the boundary conditions can be enforced on Eq. 3.43. As usual in BEM, the vector X stores the unknown boundary values whereas the vector F contains the prescribed boundary values. Then:

$$AX = BF + KQ \Rightarrow X = M + RQ \tag{3.45}$$

where the classical columns change procedure between H and G matrices lead to the A and B matrices. Matrix B stores the influence terms associated to the prescribed values at the boundary whereas matrix A contains the influence terms associated to the unknown values at the boundary. The variables M and R are as follows:$M = A^{-1}BF$ and $R = A^{-1}K$.The boundary conditions enforcement similarly modifies Eq. 3.44 as follows:

$$\sigma + A^{'}X = B^{'}F + KSQ \Rightarrow \sigma = N + SQ \tag{3.46}$$

in which $A^{'}$ and $B^{'}$ appear from the columns change between $H^{'}$ and $G^{'}$ matrices. The variables N and S are as follows: $N = B^{'}F - A^{'}M$ and $S = KS - A^{'}R$.

The integral representations on Eq. 3.25 and Eq. 3.39 have been evaluated numerically through Gauss–Legendre numerical scheme. Besides, Guiggiani and Gigante (1990), Guiggiani *et al.* (1992) scheme regularises the hypersingular kernels on these equations, particularly the dipoles kernels. In appendix D and appendix E, the evaluation of the analytical terms required by Guiggiani scheme is presented. Therefore, this integration scheme leads to low error during the algebraic representation. It is worth mentioning that

solely discontinuous boundary elements discretise the crack surface because kernel G_{im}^{lj} is hypersingular.

Eq. 3.45 and Eq. 3.46 solve the cohesive crack growth problem. The former equation enables the solution of the unknowns at the boundary whereas the latter equation provides the stresses and displacements values at the crack surfaces. Thus, the boundary values depend on the dipoles values at the equilibrium configuration. Because cohesive laws relate cohesive stresses to crack opening displacements, such mechanical problem becomes nonlinear. The problem has been solved herein by the Newton-Raphson scheme, in which try and correction steps have been applied. Then, Eq. 3.46 assesses the stress state, which leads to the exceeding values of stresses and the increment on the dipoles values. Consequently, the crack opening displacements increment follows Eq. 3.33, which trigger a new stress state of equilibrium. The convergence occurs when the difference between the stress states (try and prevision) is smaller than the prescribed tolerance. Because all relevant matrices are kept constant during the iterative procedure, this scheme is named as constant operator solution technique (OLIVEIRA; LEONEL, 2013; ALMEIDA; LIMA JUNIOR; BARBIRATO, 2020a). Then, instead of solving a system of algebraic equations at each iteration, this implementation scheme can utilise a simple matrix-vector multiplication operation for assessing the equilibrium configuration. This simply strategy is computationally efficient.

It is worth mentioning that the DBEM solves the nonlinear problem using the algebraic equations written over all collocation points in the mesh, i.e. external and crack surface boundaries. On the other hand, the dipole-based formulation solves the problem by Eq. 3.46, which associates the dipoles to stresses along the crack path. Then, the proposed formulation handles the nonlinear problem through a small system of algebraic equations in comparison to the classical DBEM. In addition, the DBEM modelling requires six integral equations (three displacements and three tractions) per couple of points at the crack surface. On the other hand, the dipole-based formulation requires solely three integral equations in the same condition. Therefore, the dipole-based approach requires the half of algebraic equations in comparison to the DBEM. It leads to a faster and effective performance in terms of computational effort, which is a huge bottle neck in three dimensional modelling.

3.7 The crack growth process

The crack propagates when the stress state at the crack front violates a failure criterion. In the present study, the stresses values at internal points surrounding the crack front enable the evaluation of the stress state at the crack front points, Fig. 10a. This procedure requires the evaluation of the stresses components in internal points

positioned into a semi-circular scheme along the crack front. Then, these values enable a simple polynomial extrapolation along each radial position surrounding the collocations along the crack front. The stress state at the crack front points have been obtained by simply averaging all extrapolated stress values. For instance, two internal points per radial position provide a simple linear extrapolation for the stresses components, Fig. 10a. However, the accuracy of the stresses values can be improved with quadratic or even high-order approximations. The Fig. 10b illustrates the appearing of the FPZ in the first crack surface length increment. This zone appears in front of the notch tip and its geometric configuration follows the propagation methodology described below. The energy dissipation phenomena occur at the FPZ and its effects have been modelled by the formulation proposed herein. Besides, discontinuous boundary elements discretise the zone over which geometry and mechanical fields (dipoles included) have been approximated.

The failure criterion adopted herein is Saleh and Aliabadi (1995). Therefore, the crack propagates when the tensile principal stress extrapolated from the internal points is higher than the tensile material strength. The crack growth direction follows the maximum circumferential stress theory. Then, the crack grows perpendicularly to the principal tensile stress evaluated at the crack front (SALEH; ALIABADI, 1995; LEONEL; VENTURINI, 2010). Finally, the crack growth length obeys the cohesive law. Therefore, the crack length increments can be obtained by determining the point along the crack growth direction in which the principal tensile stress equals the tensile material strength. For sake of consistency, this step can be formulated as an optimisation problem by minimising the absolute difference between these two values. In the present study, one applied the classical Golden Section algorithm for this purpose once the optimisation problem involves solely one variable.

Figure 10 – Internal points distribution in front of the notch tip (a) and introduction of fracture process zone (b)

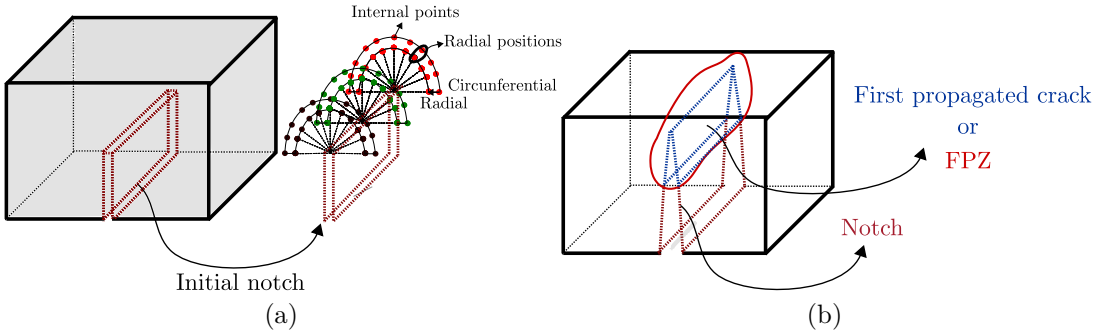

Source: The author.

The quantities previously mentioned provide information for the crack propagation process. Then, as the crack grows, new elements and collocation points add to the mesh. Discontinuous quadrilateral linear isoparametric elements discretise the crack surface

because of the continuity requirements of the dipoles hypersingular kernels, Fig. 11.

A local remeshing procedure becomes necessary when the crack surface crosses the external boundary. In this case, the crack growth path enables the identification of crossed boundary elements at the external boundary, Fig. 12. Thus, the crossed boundary element is divided into two quadrilateral or two quadrilateral and one triangular boundary elements when the crack front crosses entirely the external boundary element, Fig. 12b and Fig. 12d. Besides, the crossed boundary element is divided into three quadrilateral boundary elements when the crack front ends within the crossed element domain, Fig. 12f and Fig. 12h. The remeshing procedure splits and transforms continuous external boundary elements into edge-discontinuous boundary elements, which account properly the mechanical fields discontinuity triggered by the boundary cross. Then, the influence matrices associated to these elements have been removed and new elements appear from the division of crossed elements. The influence matrices associated to the crossed and the new elements can be evaluated and added to the algebraic representation. It is worth mentioning that the added collocation points lead to additional rows and lines into the algebraic representation.

Figure 11 – Element adding scheme during crack propagation

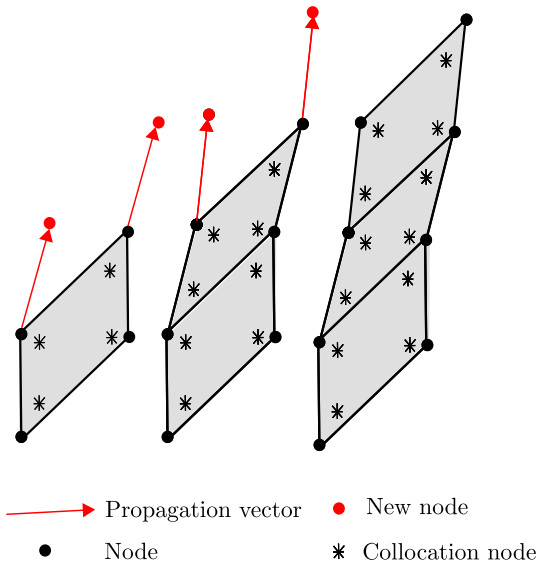

Source: The author.

For sake of clarity, the crack propagation process starts at the initial notch tip. The initial notch might be accounted by the DBEM approach, in which different integral equations integrate the collocations at the opposite crack surfaces. However, in the present study, the initial notch has been simulated as an initial void, as illustrated in Fig. 10. This strategy enables the application of the classical and stable displacement integral equation along the entire external boundary. Then, the principal tensile stress has been evaluated

at the middle path of the upper void surface. The propagation occurs when this stress is higher than the material tensile strength.

Figure 12 – Local remeshing procedure considering quadrilateral elements

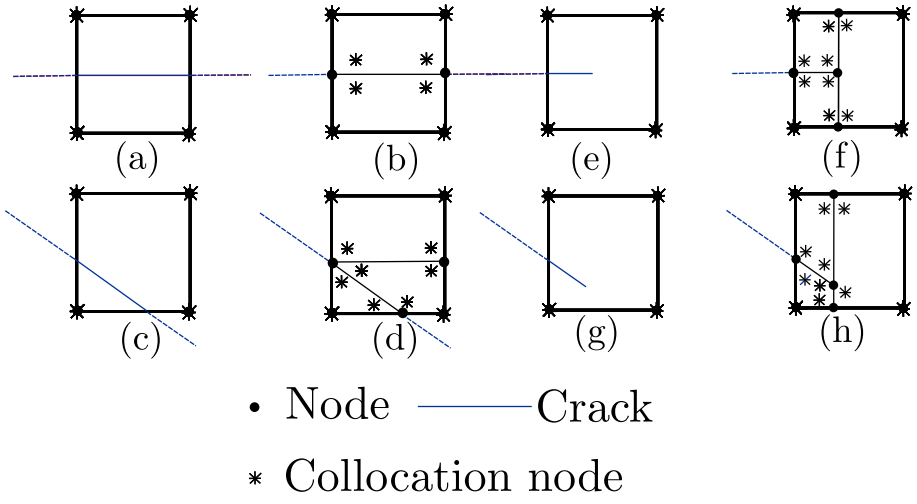

Source: The author.

3.8 Flowcharts of the Numerical Solution Scheme

The proposed nonlinear formulation solves cohesive crack propagation problems as summarised in Fig. 13. These flowcharts illustrate the calculus steps required by the dipole-based formulation. In the first load-step, the unknowns at the boundary have been evaluated without the presence of cohesive cracks once the notch is the material discontinuity. Therefore, the boundary mesh and the integration procedures lead to the H and G matrices. Then, the solution of the algebraic system of equations provides the unknown values at the boundary, X . The stress fields can be evaluated after the determination of X. The cohesive crack propagation procedure starts if the principal tensile stress at the crack front points is higher than the material tensile resistance, see section 3.7. In negative case, one applies another load step. In positive case, the crack growth direction and the crack length increment can be determined. Thus, new boundary elements add the mesh for representing the FPZ, Fig. 11. Afterwards, the internal fields can be evaluated, Fig. 13a, which enable the assessment of the stress state at collocations positioned at the cohesive crack surfaces, Fig. 11. Then, the dipoles terms add the algebraic representation and the stresses along the FPZ are corrected iteratively following the adopted cohesive law, Eq. 3.46. Because the problem is nonlinear and solved by the Newton-Raphson scheme, displacements, tractions and internal fields must be updated at each incremental step (Inc). In Fig. 13b, $Ninc$ is the total number of load steps and α indicates the increment of load, $\alpha = Inc/Ninc$. Thus, the load is applied within $Ninc$ steps until its total value. It is

worth emphasizing that the problem is nonlinear and solved into an incremental–iterative scheme. Thus, the equilibrium configuration has been achieved by the superposition of the solutions during the correction iterations. After the convergence, one applies another load step, which accounts for the dipole terms into the algebraic representation once cohesive crack are now part of the problem.

It is worth mentioning that the crack propagation procedure, Fig. 13c, requires crack growth direction assessment and eventually the local remeshing process at the external boundaries. The vector of elastic stress, N , Eq. 3.46, and the matrices K and KS, Eq. 3.43 and Eq. 3.44, must be calculated during this step. Finally, the matrices R , Eq. 3.45, and S , Eq. 3.46, can be evaluated. In the iterative procedure, Fig. 13d, the exceeding stresses lead to the dipoles, Eq. 3.46, which enable the crack opening values assessment, Eq. 3.33. At the end of the procedure, the convergence can be achieved as a function of non-equilibrated stress values and the vectors X and σ can be finally updated.

Figure 13 – Flowchart of the dipole-based model (a) incremental procedure (b) crack propagation procedure (c) iterative procedure (d)

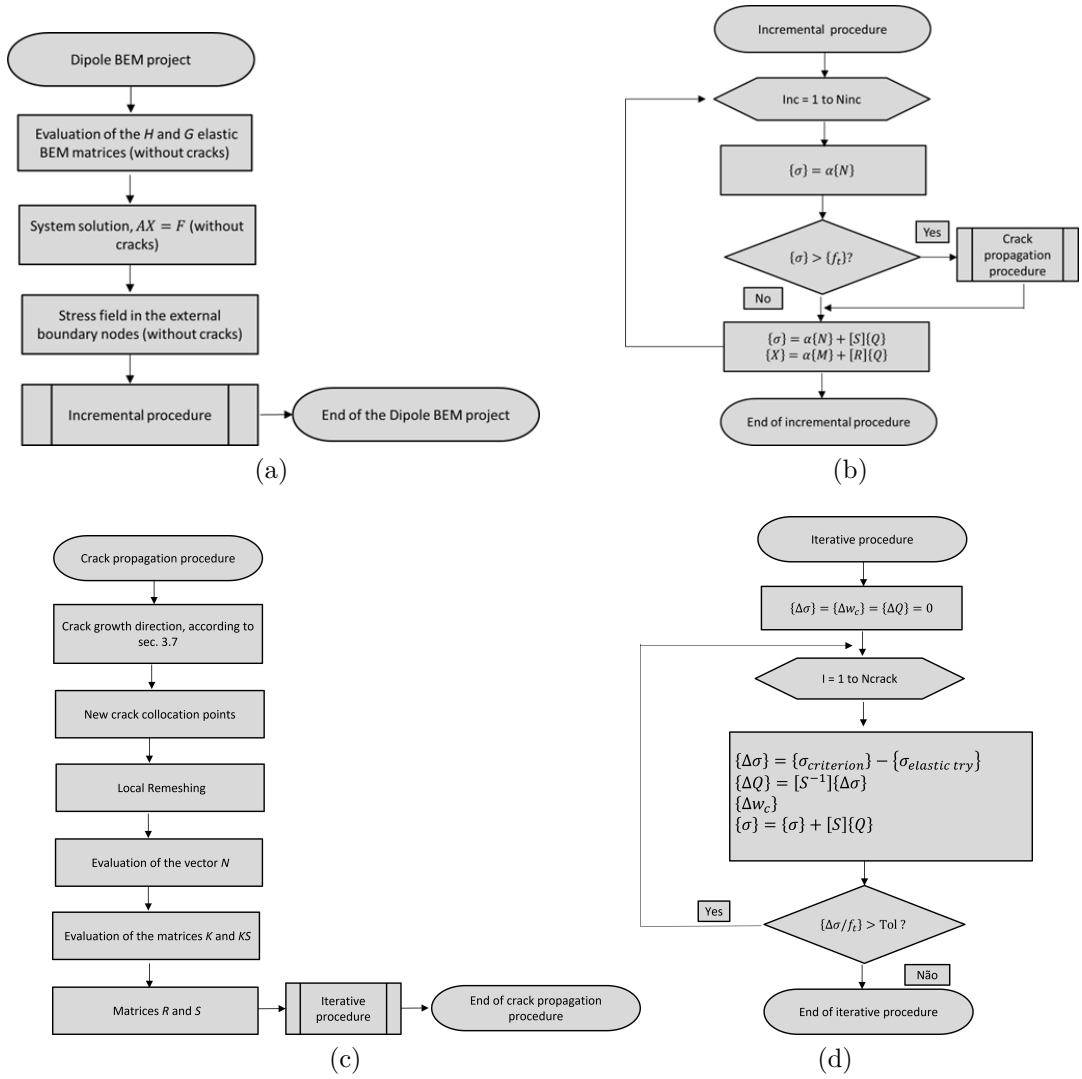

Source: The author.

3.9 Applications

Five applications demonstrate the accuracy of the proposed nonlinear dipole-based BEM formulation in modelling three-dimensional cohesive crack propagation problems. The first three applications deal with crack growth in mode I. The last two applications handle mixed mode crack propagation problems. The reference results are numerical and experimental responses available in the literature. The nonlinear system of equations accounts for a tolerance of convergence equal 10^{-2} based on the norm of non-equilibrated stress values.

3.9.1 Application 1: Parallelepiped solid under tensile loading

The first application deals with a parallelepiped solid under a pure tensile loading. The left structure end is clamped whereas a displacement $\bar{u} = 0.02\,m$ has been applied incrementally at the right end. A cohesive crack is assumed to appear at the half span length along the YZ plane. Because the normal stress along X direction is constant, the cohesive crack surface takes a square dimension of $1\ x\ 1\ m^2$ during the propagation. Fig. 14 illustrates the structure geometry, boundary conditions and material properties.

Figure 14 – Parallelepiped solid under tractions

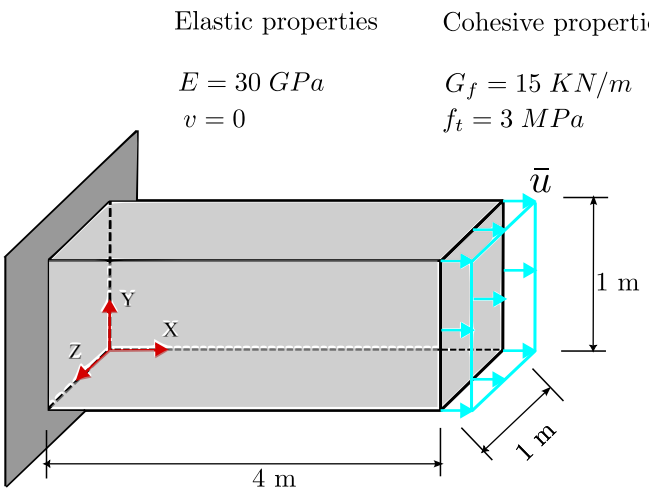

Source: The author.

In Fig. 15a, the boundary element mesh adopted in this application is presented. The mesh contains 360 collocation points and 250 quadrilateral isoparametric linear boundary elements. The external loading has been applied within 100 load steps. Fig. 15b presents the displacement X results for the last load step. It is worth mentioning the solid fracture into two independent parts.

In Fig. 16 the curve force *versus* displacement along the incremental-iterative process is presented. For sake of information, the analytical responses presented in Oliveira and Leonel (2013) are reference herein. The mechanical behaviour is linear elastic until the normal stress along X direction equals the tensile material strength. In this moment, the cohesive crack appears and cohesive laws govern the material behaviour along the FPZ. This application analyses the structural behaviour when the cohesive laws described in section 3.1 govern the material behaviour at the FPZ, in which both linear and bilinear cohesive laws predicted the structure fracture. Fig. 16 illustrates an excellent agreement among numerical and analytical results. The dipole-based formulation represented accurately the mechanical behaviour predicted analytically. It is worth mentioning that the entire analysis

Figure 15 – Boundary discretisation (a) Crack propagation (linear cohesive law) in colour scale (m) (b)

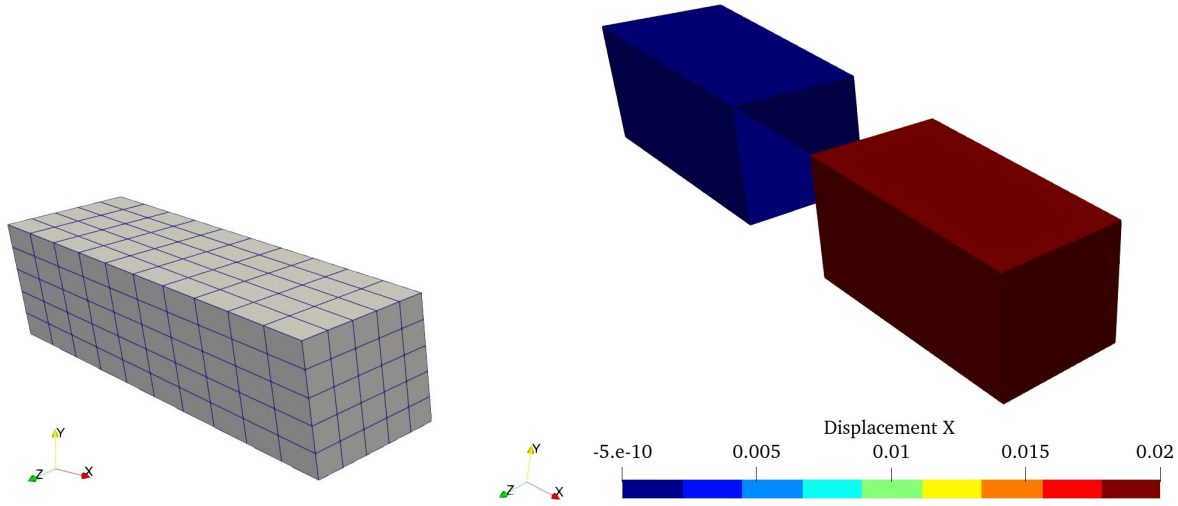

(a) (b)

Source: The author.

with linear cohesive law required solely 36 seconds, which illustrates the computational efficiency of the dipole-based formulation.

Figure 16 – Force *versus* displacement curves

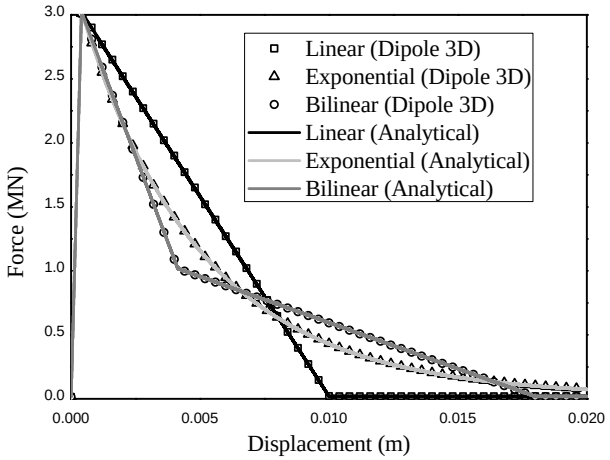

Source: The author.

3.9.2 Application 2: Three-point bending test

The second application handles a three-point bending test in a notched concrete specimen. Carpinteri (1989) analysed this specimen experimentally whereas Most and Bucher (2007) utilised standard 2D FEM and Chaves, Peixoto and Silva (2023) utilised

a 3D BEM formulation with the continuum strong discontinuity approach (CSDA) for numerical results. These experimental and numerical results are references for the numerical responses achieved by the proposed dipole-based formulation. Fig. 17a presents the structure geometry, dimensions, boundary conditions and material properties. Fig. 17b illustrates the boundary mesh utilised within the BEM modelling, which is composed of 3441 collocation points and 2900 quadrilateral isoparametric linear boundary elements. The external loading $\bar{u} = 0.25\ mm$ has been applied within 200 load steps.

Figure 17 – Three-point bending test (a) Boundary mesh (b)

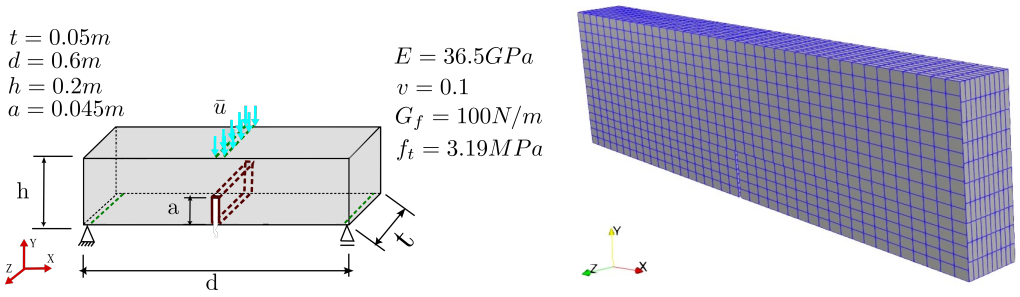

(a) (b)

Source: The author.

The crack propagation process starts at the notch tip and the crack grows towards the external load region. Then, the crack grows in pure mode I. Fig. 18a illustrates the crack growth path and the displacements along Y direction for two particular load steps: the first and the last. This figure describes the displacement discontinuity caused by the crack growth. Besides, the BEM predictions do not indicate the specimen fracture, despite the crack tip is at few millimetres of the upper boundary in the last load step.

Figure 18 – Crack path in colour scale (m) for the linear cohesive law: (a) 86 load steps; (b) 200 load steps.

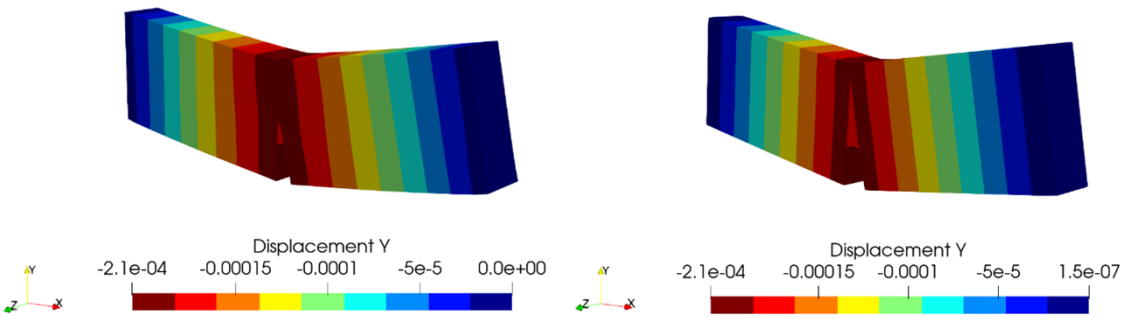

(a) (b)

Source: The author.

In Fig. 19, the mechanical behaviour by the curves relative load *versus* relative mid

deflection. The relative load is $\delta_p = P/(t.h.f_t)$, where P is the equivalent external load value along Y direction is presented. The relative mid deflection results from the quotient of the mid deflection, f, and the beam height, h. Fig. 19 demonstrates the excellent accuracy provided by the dipole-based formulation. Particularly for the linear cohesive law, which was the cohesive law adopted by the references (MOST; BUCHER, 2007). It is important to highlight the higher peak load value when using the linear cohesive law, which is plausible considering that the material degradation under this law occurs more rapidly than with the others. In addition, the dipole-based formulation also presents excellent results in comparison to the CSDA approach (CHAVES; PEIXOTO; SILVA, 2023). Besides, the mechanical representation by the dipole-based formulation during the softening part is remarkable. As expected, the bilinear and exponential cohesive laws led to lower peak load values in comparison to the linear cohesive law.

The dipole-based formulation required 30.4 minutes for the entire nonlinear analysis with linear cohesive law. This performance is excellent and illustrates the computational efficiency of the proposed formulation. Obviously, the computational time consuming can be reduced with the use of less load steps, which lead to the less crack propagation steps.

Figure 19 – Relative load *versus* relative mid deflection for application 2

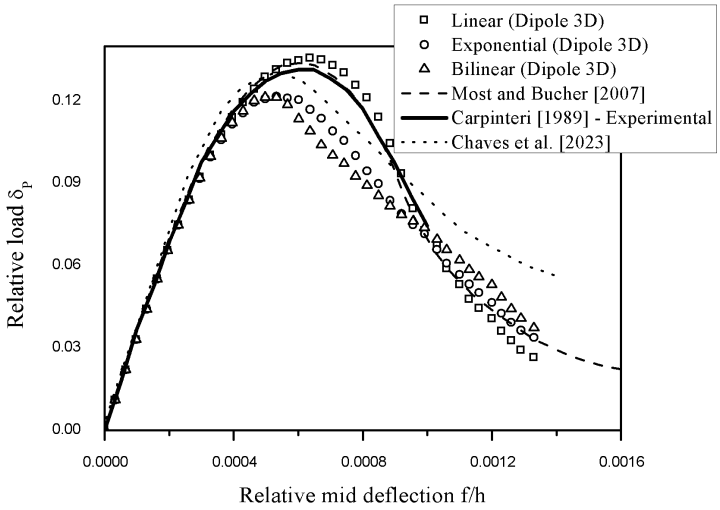

Source: The author.

3.9.3 Application 3: Concrete specimen in Mode I (Wedge-Splitting Test)

The third application deals with the fracture modelling of a concrete specimen in pure mode I propagation. A horizontal displacement $\bar{u} = 2\,mm$ has been applied incrementally on both sides at the structure top. A cohesive crack is assumed to appear in the notch tip. Fig. 20a illustrates the structure geometry (mm), boundary conditions and material properties. Fig. 20b illustrates the boundary element mesh adopted in this

application. The mesh contains 2754 collocation points and 2176 quadrilateral isoparametric linear boundary elements. The external loading has been applied within 200 load steps.

Figure 20 – Wedge-splitting test (a) Boundary discretisation (b)

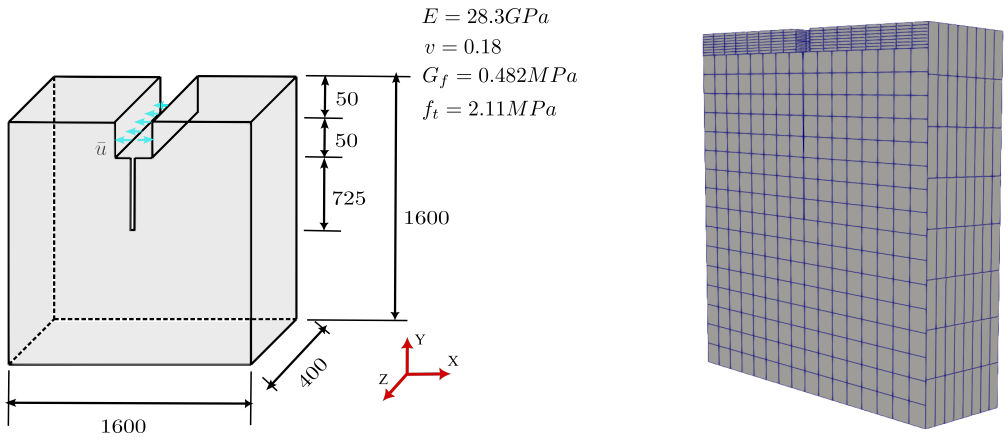

(a) (b)

Source: The author.

In Fig. 21a, the displacement X results whereas Fig. 21b presents the displacement Y for the last load step (200 load steps), is presented. It is worth mentioning that the dipole BEM approach did not predict the specimen fracture.

Figure 21 – Crack path (colour scale - (m)) (a) horizontal (b) vertical

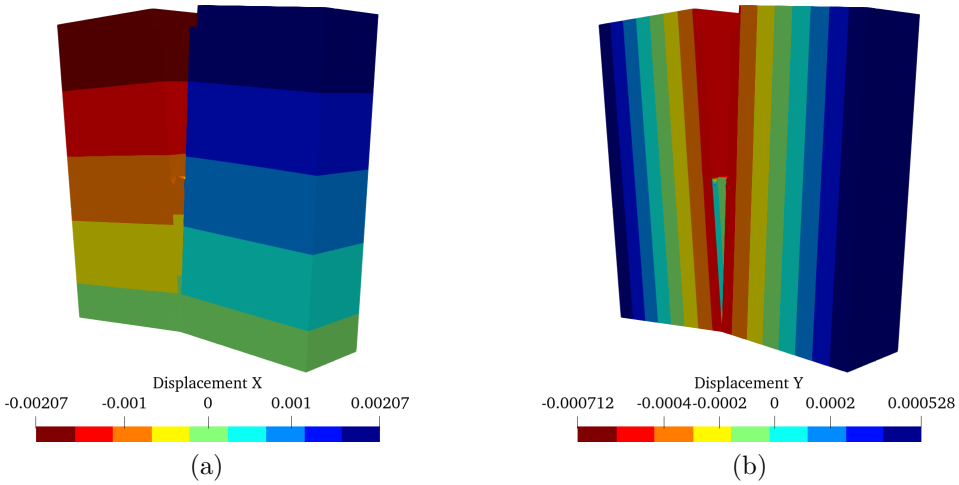

(a) (b)

Source: The author.

In Fig. 22, the curve force *versus* displacement during the incremental-iterative process is presented. For sake of information, the experimental response presented in Winkler (2001) is reference herein. The mechanical behaviour is linear elastic until the normal stress equals the tensile material strength. In this moment, the cohesive crack appears and cohesive laws govern the material behaviour along the FPZ. This application analyses the structural behaviour when the cohesive laws described in section 3.1 govern

the material behaviour at the FPZ, in which the linear cohesive law better predicted the peak load. Fig. 22 illustrates excellent agreement among numerical and experimental results. The dipole-based formulation represented accurately the mechanical behaviour predicted experimentally.

It is worth mentioning that the entire analysis with linear cohesive law required solely 8 minutes, which illustrates the computational efficiency of the dipole-based formulation.

Figure 22 – Force *versus* displacement curves

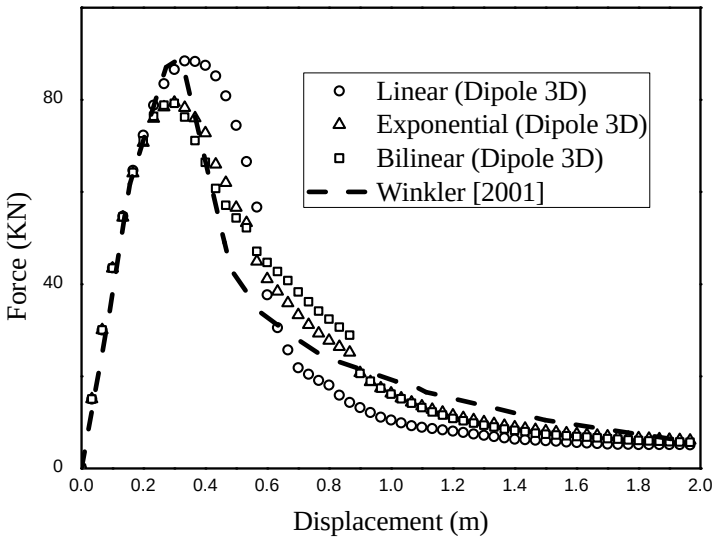

Source: The author.

3.9.4 Application 4: L-Shaped specimen

This application models the material failure in a L-shaped concrete specimen. Winkler (2001) analysed this specimen experimentally, which lead to the reference results herein. In addition, Cervera, Barbat and Chiumenti (2017) analysed this specimen with a 3D FEM model based on an isotropic damage approach. Fig. 23a presents the structure geometry, boundary conditions and material properties (WINKLER, 2001).

The proposed dipole-based formulation has been utilised in this application for modelling mixed mode cohesive crack growth problem. The boundary mesh consists of 2630 collocation points and 2250 quadrilateral isoparametric linear boundary elements, Fig. 23b. The external loading has been applied within 200 load steps. Besides, the three cohesive laws presented in section 3.1 describe the nonlinear material behaviour at the FPZ. Fig. 24 illustrates the displacement results provided by the proposed dipole-based formulation along X and Y directions. This figure shows the displacement discontinuity caused by the crack growth, in which the numerical approach does not predict the specimen fracture.

Figure 23 – L-shaped section (a) Boundary discretisation (b)

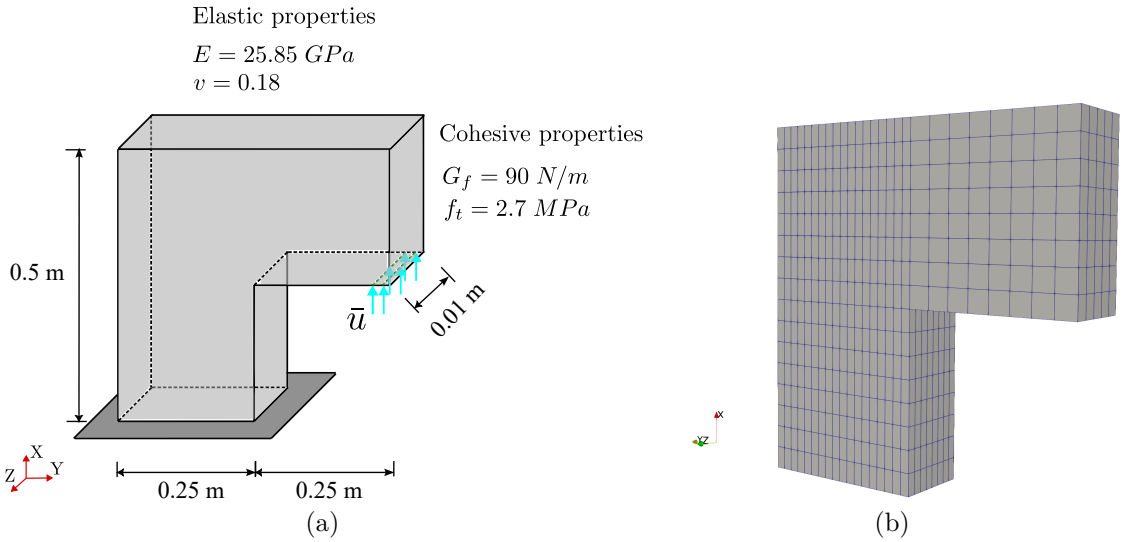

Source: Author.

In Fig. 25, the crack paths predicted by the dipole-based approach and the references is presented. This figure illustrates the result provided by the linear law once bilinear and exponential led to very similar response. The proposed formulation led to good predictions in comparison to the experimental range curves (WINKLER, 2001) and the numerical reference (CERVERA; BARBAT; CHIUMENTI, 2017).

Fig. 26 presents the curves force *versus* displacements, which indicate the material degradation evolution as a function of external loading values. Bilinear and exponential cohesive laws led to excellent performance in comparison to experimental results. These laws led to excellent representation of the peak load value and the softening behaviour. As expected, the linear cohesive law provided higher peak-load value in comparison to bilinear and exponential approaches. The results presented in Fig. 26 indicate the accuracy of the proposed BEM formulation in modelling mixed mode crack growth.

Finally, the dipole-based formulation with linear cohesive law required 32.5 minutes for the entire nonlinear analysis. It illustrates the computational efficiency of the proposed formulation. The computational time consuming can be reduced with the use of less load steps, which lead to the less propagation steps.

For sake of completeness, a mesh dependency analysis has been carried out in this application. This complementary analysis demonstrates the objectivity of the mechanical responses predicted by the proposed nonlinear formulation as a function of the mesh refinement. Then, in addition to the boundary mesh illustrated in Fig. 23b, which is named as mesh A and consists of 2630 collocation points and 2250 elements, three other boundary meshes have been considered. The boundary mesh B accounts for 735 collocation points and 540 boundary elements, the mesh C consists of 1918 collocation points and 1596

Figure 24 – Crack path (linear cohesive law) in colour scale (m): 41 load steps (a) and (c); 200 load steps (b) and (d)

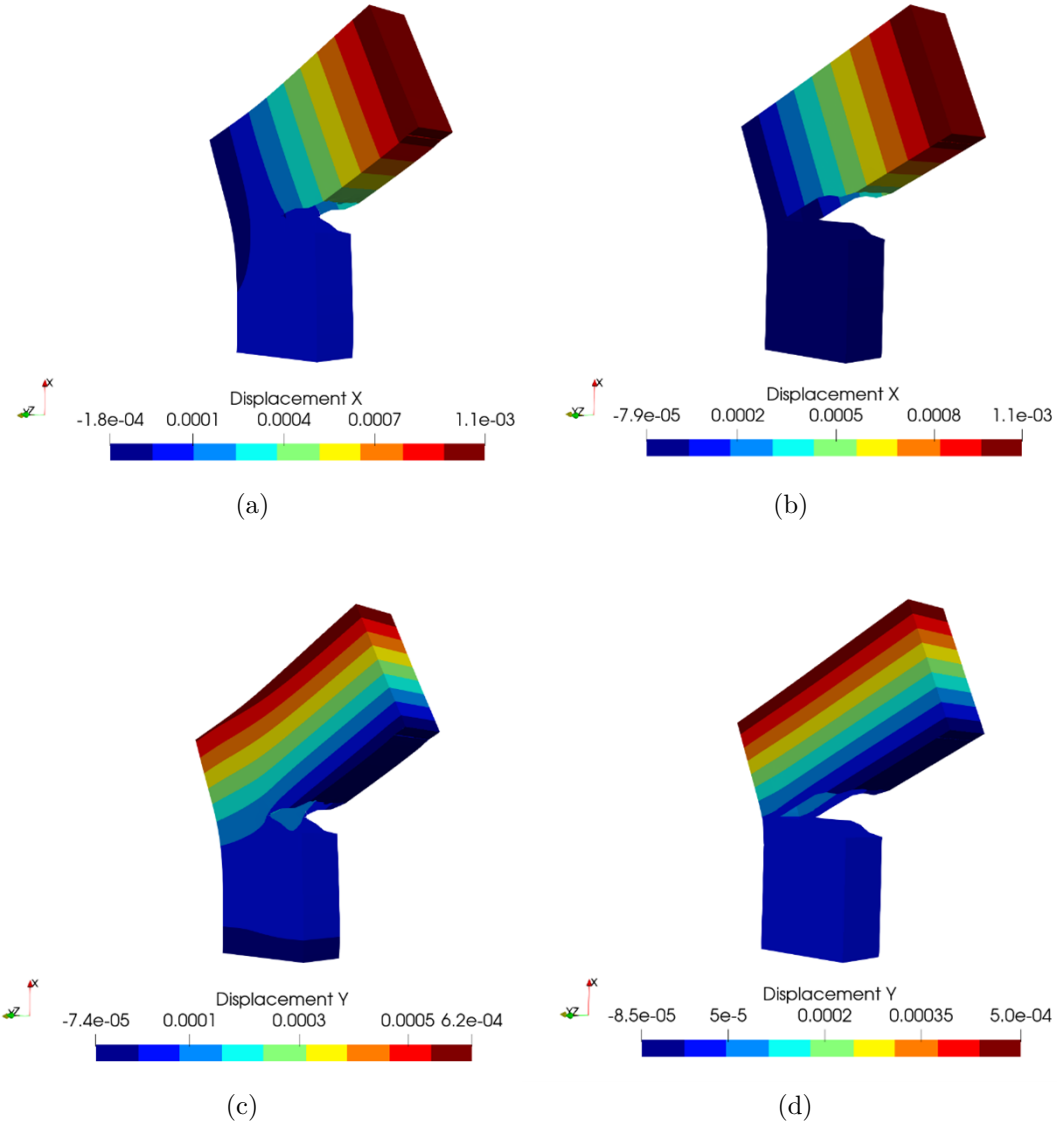

Source: The author.

boundary elements and finally the mesh D is composed of 3605 collocation points and 3157 boundary elements. The entire analysis required 12.15 minutes, 25.43 minutes and 52.33 minutes for the respective B, C and D meshes. Fig. 27 illustrates these meshes, which utilise quadrilateral isoparametric linear boundary elements into the boundary and crack surface discretisation.

Fig. 28 illustrates the responses provided by the above-mentioned meshes. Fig. 28a presents the curves force versus displacement. For sake of simplicity, solely the bilinear cohesive law has been utilised in the mesh convergence analysis. Nevertheless, similar behaviour has been observed with the other cohesive laws introduced section 3.1. As

Figure 25 – Crack path in the L-shaped specimen

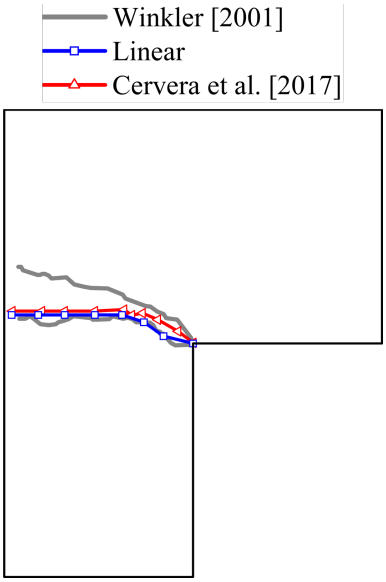

Source: The author.

Figure 26 – Force *versus* displacement curves

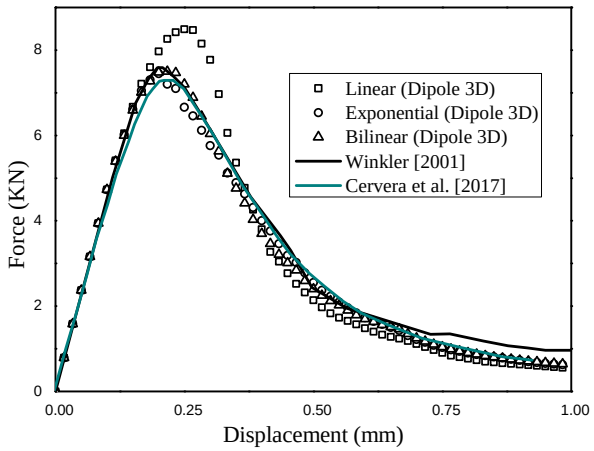

Source: The author.

expected, the numerical results demonstrate convergence as the mesh refinement improves. Even the coarse mesh enables the accurate description of the peak load value. However, this mesh, mesh B, do not describe properly the softening behaviour and the crack path. Finally, Fig. 28b, illustrates the error evolution behaviour for the tested meshes. The absolute error is the absolute difference between the force values observed in the experimental and numerical curves. It is noticeable the higher value of error in the less refined mesh, mesh B. Oppositely, the meshes A, C, and D demonstrate equivalent values of error. Then,

this analysis illustrates the objectivity of the mechanical fields predictions. Because the dipole-based formulation corrects nonlinearly the stress field along the FPZ, even coarse meshes can lead to accurate results. This aspect has major importance in the context of computational effectivity, which is a bottle neck in three-dimensional computational fracture mechanics.

It is worth mentioning that mesh convergence analyses have been carried out in applications 1 and 2, in which mechanical fields objectivity and mesh convergence have been also observed. These results are omitted herein to avoid repetitive matter.

Figure 27 – Boundary discretisation

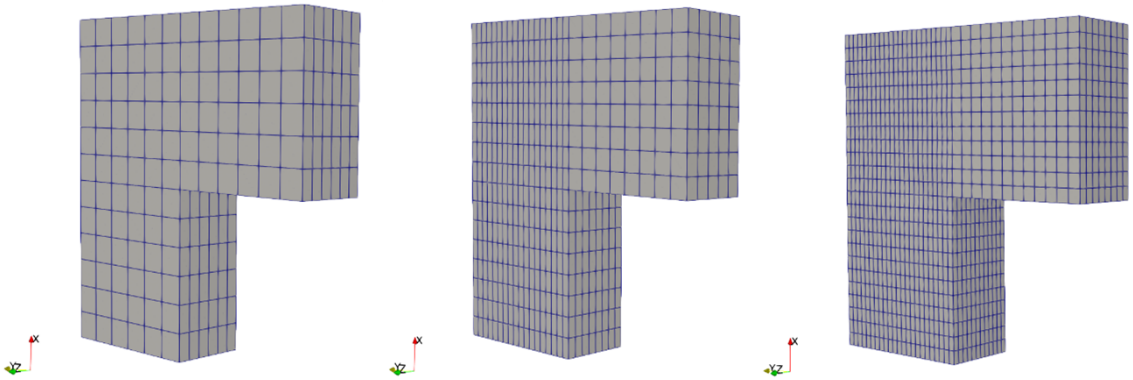

(a) Mesh B (b) Mesh c (c) Mesh d

Source: The author.

Figure 28 – Mesh convergence analysis: Force versus displacement curves (a) Error analysis (b)

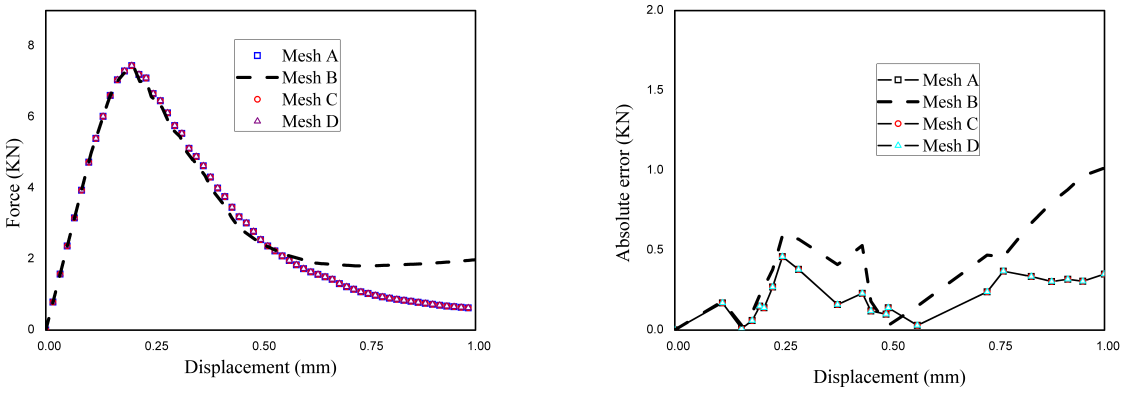

(a) (b)

Source: The author.

3.9.5 Application 5: Geometrically complex concrete specimen subjected to mixed-mode fracture

The last application of this study deals with the crack propagation modelling in a geometrically complex concrete specimen subjected to fully mixed-mode fracture and combined modes I-II-III. This application provides benchmark results for further researches in nonlinear computational fracture mechanics field. Particularly, results within complex geometry and fracture modes context, which are complex tasks in experimental programs. Fig. 29a llustrates specimen's geometry, material properties and boundary conditions. The specimen has irregular parallelepiped geometry with an asymmetric notch positioned at its bottom surface. The loading has been applied at the specimen upper surface.

The proposed dipole-based formulation has been utilised in this essentially three-dimensional fracture problem. The boundary mesh adopted herein consists of 2250 linear quadrilateral boundary elements and 2630 collocation points, Fig. 29b. Besides, the external loading has been applied within 200 load steps and the three cohesive laws presented in section 3.1 model the mechanical behaviour along the FPZ. The load is applied in $X = 0.2105$ m.

Figure 29 – Analysed specimen (a) Boundary discretisation (b).

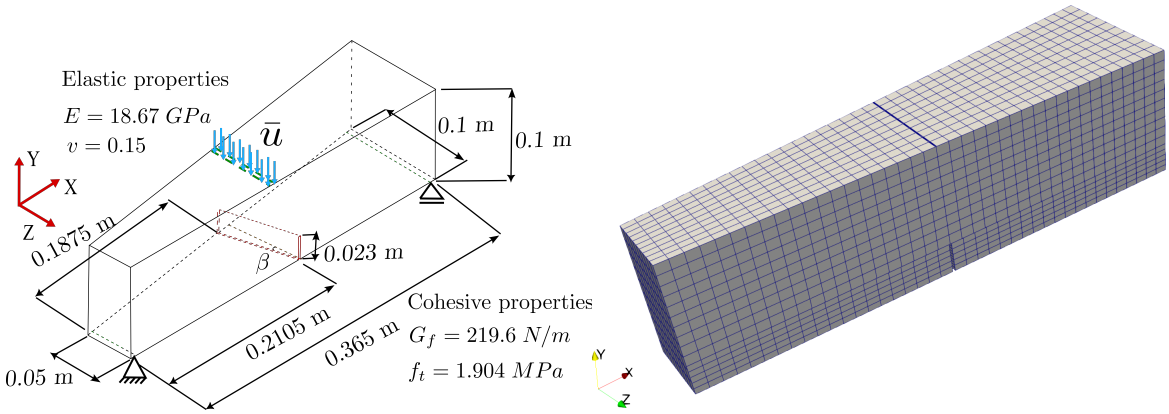

Source: The author.

The mechanical behaviour can be assessed by the evolution of force and displacement values as a function of external loading. The forces have been evaluated at the specimen upper surface and the displacements values involve the crack opening mouth displacement. Fig. 30 illustrates this evolution. The three cohesive laws employed herein enable excellent agreement along the linear elastic part. Afterwards, the linear cohesive law led to higher peak load value in comparison to bilinear and exponential approaches, as expected. Finally, the three cohesive laws represented the softening material behaviour, similarly to the observed in previous applications.

Figure 30 – Force versus crack mouth opening displacement curves (CMOD)

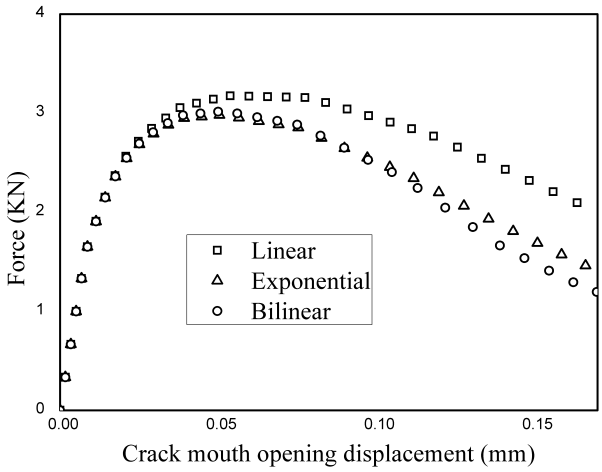

Source: The author.

In Fig. 31, the displacement results provided by the dipole-based formulation along Y direction in two different load steps (linear cohesive law), (a) 50 and (b) 200 is provided. The figure shows the significant displacement discontinuity caused by the crack growth process. Additionally, the dipole-based formulation did not predict the structural collapse in spite of the large extension of crack surfaces.

Figure 31 – Displacement along Y direction (a) 50 load step (b) 200 load step

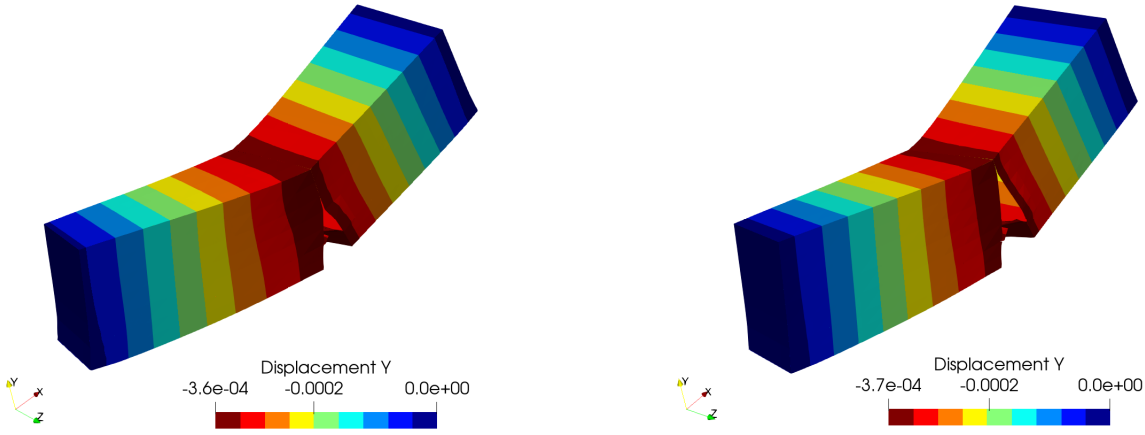

(a) (b)

Source: The author.

In Fig. 32, the CMOD as a function of load steps evolution is presented. In this figure, mode I indicates the opening mode, mode II is the sliding mode and mode III the tearing mode both evaluated the crack mouth. Fig. 32 shows mode I as preponderant during

the entire analysis. This behaviour is expected once the crack surfaces grow according to the maximum circumferential stress theory, i.e. along a principal direction. Nevertheless, modes II and III are not nil and influence importantly the crack path, particularly the tearing mode. Therefore, the crack propagates under mixed-mode I-II-III. The linear cohesive law has been utilised in this analysis.

Figure 32 – Crack mouth opening displacement versus load steps: mode I (a) mode II and III (b).

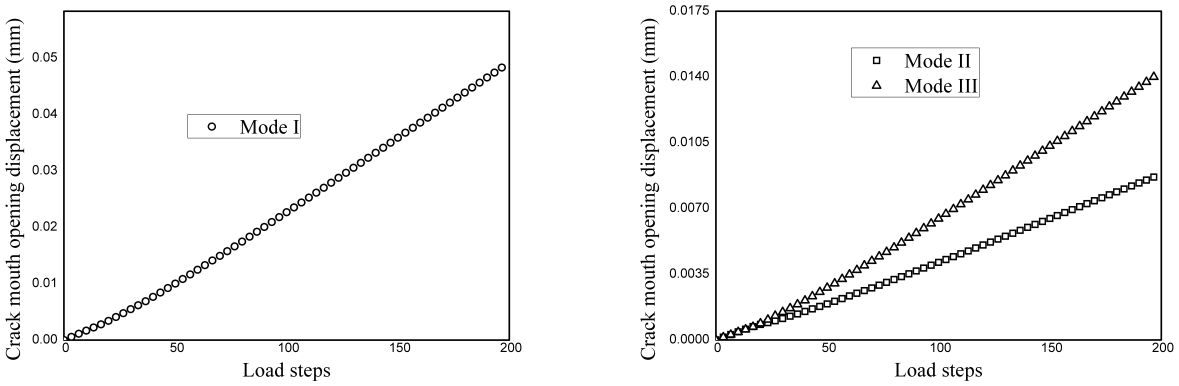

(a) (b)

Source: The author.

Finally, Fig. 33 presents the crack growth path during two specific load steps, 50 (a) and 200 (b). This result has been obtained using the linear cohesive law. Particularly, this figure illustrates the crack surface crossings along xy specimen's planes. The solid curve indicates the crossings for the notch end positioned in whereas the dashed curve illustrates, similarly, the crossings for the notch end positioned in . The solid curve shows crossings in predominant mode I. This path is expected because of the notch end position, which is aligned with the upper surface loading. Contrarily, the dashed curve illustrates the influence of mode II during the propagation. This path has been triggered by the asymmetric position of notch end and upper surface loading. Therefore, the notch ends cross differently the specimen's boundaries, which is due to the specimen's asymmetric geometry and problem boundary conditions.

Figure 33 – Crack growth paths along specimen's xy planes: 50 load steps (a) 200 load steps (b).

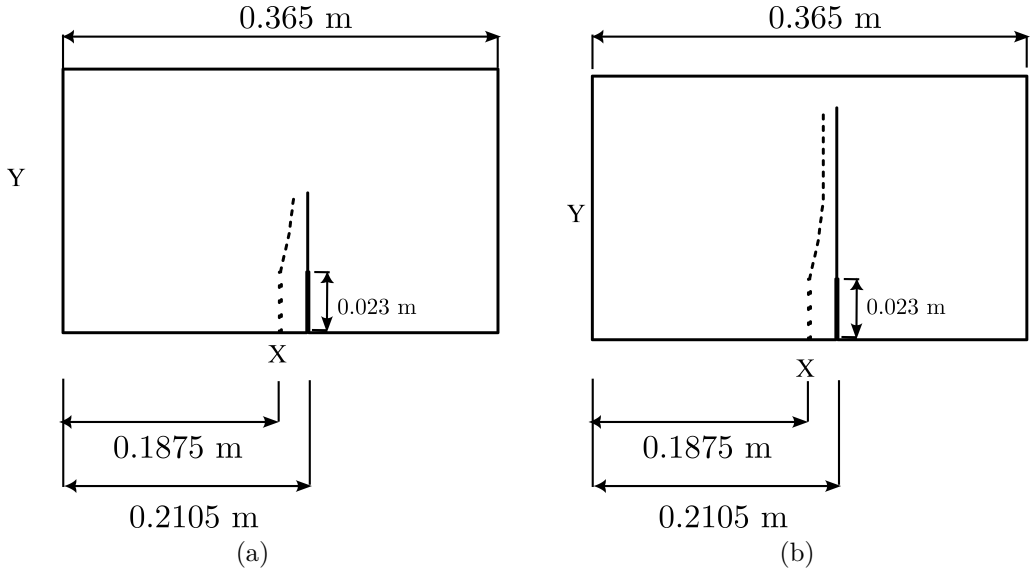

Source: The author.

4 THE COHESIVE CRACK MODELLING WITHIN DIFFERENT LOADING RATES CONTEXT

Next, a viscous-cohesive cracking approach that considers the influence of loading rate is presented. In this context, viscosity refers to the variation in the loading application rate. The formulation modifies the classical cohesive crack model by introducing a rate-dependent function. The model used is the one proposed by Santos and Sousa (2020), which represents the behavior of concrete at low loading rates. In general, low loading rates are those which inertial effects can be neglected and which are characterized by the reduction of apparent fracture energy, G_f, and critical crack opening, w_c, as broadcast on Wittman *et al.* (1987), Ruiz *et al.* (2010), Santos and Sousa (2020).

4.1 Loading Velocity Rate Parameters

The classical cohesive crack modelling accounts for quasi-static conditions. Thus, the loading must be applied within low velocities rates and inertial effects have been disregarded. However, experimental results involving the fracture of specimens composed of quasi-brittle materials demonstrate that G_f,f_t and w_c parameters hugely modify as a function of the loading velocity rate increase (RUSH, 1960; RUIZ *et al.*, 2010; WITTMAN *et al.*, 1987). Santos and Sousa (2020) addressed analytically this failure problem and proposed improvements over the classical cohesive laws. However, this problem has been marginally addressed in the literature in the numerical domain. It is worth mentioning that the present study is pioneer in handling numerically this failure problem within three-dimensional description.

The mechanical influence of different loading rates over the material resistance at the energy dissipation zone can be handled properly by a viscous (time dependent) function, which modifies the classical cohesive crack model. Then, the viscous-cohesive approach can be defined as follows (SANTOS; SOUSA, 2020):

$$\sigma(\dot{w},w) = \Psi(\dot{w})f(w) \tag{4.1}$$

in which σ indicates the updated cohesive stress values, w is the crack opening displacement

parameter, $f(w)$ refers to the classical cohesive laws modified by the loading rate dependent fracture energy and $\Psi(\dot{w})$ is the viscous function. The crack opening rate, $\dot{w}$, is determined computationally using the relation $\dot{w} = w/\dot{w}_v$, where $\dot{w}_v$ refers to the total time of load application divided by the number of load increments. The dot over the variable indicates time variation. The $\Psi(\dot{w})$ is as follows (ROSA *et al.*, 2012):

$$\Psi(\dot{w}) = 1 + \left(\frac{\dot{w}}{\dot{w}_0}\right)^n \tag{4.2}$$

where $\dot{w}_0$ indicates a normalization parameter for w and n is the exponent of rate dependence.

The last equations presented modifications to the classic approach to the model cohesive cracking to deal with the effects of loading rate. It has been demonstrated the influence of increasing the loading rate, which leads to an increase in resistance traction of the material. However, higher strain rates also lead to a reduction in the critical crack opening displacement. Then, fragile behaviour appears at as the strain rate increases.

In this sense, Rush (1960) observed a direct relationship between strain rate, initial stiffness, peak stress value and slope immediately after the peak for bodies concrete test in flexural tests. Furthermore, Wittman *et al.* (1987) evaluated the effect of the loading rate on the value of G_f and the parameters of the bilinear cohesive law. The results show that at initial rates the value of G_f decreases to a minimum value, defined by the authors as moderate loading rates. After moderate rates, G_f grow again at high loading rates. Similar behavior appears for critical crack opening, w_c. This following equation provide an additional modification in the cohesive crack model to take into account the increase in strain rate. The modification refers to the correction of fracture energy as a function of the crack opening rate, (SANTOS; SOUSA, 2020)

The modification proposed by (SANTOS; SOUSA, 2020) has been defined as follows:

$$\sigma(\dot{w},w) = \Psi(\dot{w}) f(w,G(\dot{w})) \tag{4.3}$$

where $f(w,G(\dot{w}))$ refers to the cohesive law modified by the correction of the fracture energy, $G(\dot{w})$.

Additionally, $G(\dot{w})$ has been defined as follows (SANTOS; SOUSA, 2020):

$$G(\dot{w}) = \begin{Bmatrix} 1 - \left(\frac{\dot{w}}{\dot{w}_w}\right)^{n_w} & \text{for} & \dot{w} \leq \dot{w}_w \\ 0 & \text{for} & \dot{w} > \dot{w}_w \end{Bmatrix} \tag{4.4}$$

In the last equation, $\dot{w}_w$ is the crack opening displacement rate at which the material tends to the brittle behaviour and n_w is an exponent for governing the evolution from quasi-brittle to brittle mechanical behaviour. These parameters represent the mechanical

material behaviour and can be evaluated experimentally. Thus, as the loading rate and the material stiffness increase, a critical loading rate, $\dot{w}_w$, characterises the critical material stiffness, in which all components fail at the same limit strength.

The above-presented equations describe the mechanical behaviour of quasi-brittle materials observed in the experimental tests of (RUSH, 1960; RUIZ *et al.*, 2010; SANTOS; SOUSA, 2020). Fig. 34 illustrates the evolution of G_f , f_t and w_c as a function of loading rate increase. Then, w_c decreases as the loading rate increase and f_t slightly increase as the loading rate increase.

Figure 34 – Evolution of time dependent cohesive model

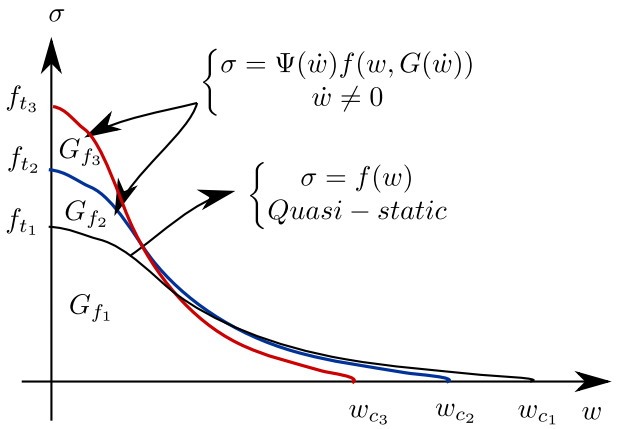

Source: The author.

It is worth mentioning that Eq. 4.3 addresses failure mechanisms during crack propagation. Vegt, Breugel and Weerheijm (2007) presented an extensive experimental analysis of the propagation of macro and microcracks at different loading rates. From microscopic analysis at FPZ, they observed that cracks propagate in the weakest part of the cement paste, that is, the interfacial transition zone, under static and quasi-static loading conditions. Then, the main crack appears due to the interconnection of small cracks in the FPZ.

However, at low and moderate loading rates, Vegt, Breugel and Weerheijm (2007) mention that the cracks have less time to search for the weakest parts. Consequently, faults were observed throughout the aggregate. Furthermore, a large number of microcracks were observed around the larger crack. The observations from Vegt, Breugel and Weerheijm (2007) can be correlated with Eq. 4.3. The distribution of small cracks in the interfacial transition zone provides a reduced value of f_t and an extended cohesive behavior, with a larger value of w_c, under static and quasi-static loading rates. On the other hand, under low and moderate loading rates, the path of the main crack through the aggregate gives a higher value of f_t and a lower value of w_c due to the reduction of neighboring cracks.

4.2 The updated cohesive laws

The loading rate parameters previously presented lead to the updated expressions for classical cohesive laws, $f(w,G(\dot{w}))$. The updated linear cohesive law (HILLERBORG; MODEER; PETERSON, 1976) is as follows:

$$\begin{aligned} \sigma_{criterion} &= E\varepsilon \quad \text{for} \quad \varepsilon \leq \varepsilon_c \\ \sigma_{criterion}(w) &= f_t\left(1 - \frac{w}{w_c^{up}}\right) \quad \text{for} \quad 0 \leq w \leq w_c^{up} \\ \sigma_{criterion} &= 0 \quad \text{for} \quad w > w_c \end{aligned} \tag{4.5}$$

where ε_c refers to the limit in the elastic phase, f_t represents the tensile strength of the material and w_c^{up} indicates the updated value for the critical crack opening, w_c, which is $w_c^{up} = G(\dot{w})w_c$:

The updated bilinear cohesive law is as follows (SANTOS; SOUSA, 2020):

$$\begin{aligned} \sigma_{criterion} &= E\varepsilon \quad \text{for} \quad \varepsilon \leq \varepsilon_c \\ \sigma_{criterion}(w) &= f_t\left(1 - \frac{\left(f_t - f_t^{''}\right)}{w^{''}}\right)\frac{w}{G(\dot{w})} \quad \text{for} \quad 0 \leq w \leq w_{up}^{''} \\ \sigma_{criterion}(w) &= \frac{f_t^{''}}{w^{''} - w_c}\frac{w}{G(\dot{w})} + f''_t\left(1 - \frac{w^{''}}{w^{''} - w_c}\right) \quad \text{for} \quad w_{up}^{''} \leq w \leq w_c^{up} \\ \sigma_{criterion}(w) &= 0 \quad \text{for} \quad w > w_c^{up} \end{aligned} \tag{4.6}$$

where the variables $f_t^{''}$, $w^{''}$, $w_{up}^{''}$, w_c and w_c^{up} are defined as:

$$\begin{aligned} f_t^{''} &= \frac{f_t^c}{3} \quad w^{''} = \frac{0.8\,G_f}{f_t} \quad w_{up}^{''} = w^{''}G(\dot{w}) \\ w_c &= \frac{3.6\,G_f}{f_t}G(\dot{w}) \quad w_c^{up} = w_cG(\dot{w}) \end{aligned} \tag{4.7}$$

Finally, the updated exponential cohesive law is governed by the following equations:

$$\begin{aligned} \sigma_{criterion} &= E\varepsilon \quad \text{for} \quad \varepsilon \leq \varepsilon_c \\ \sigma_{criterion}(w) &= f_t e^{\left(-\frac{f_t}{G_f}\frac{w}{G(\dot{w})}\right)} \quad \text{for} \quad w > 0 \end{aligned} \tag{4.8}$$

In the above equations, $\sigma_{criterion}$ is the $f(w,G(\dot{w}))$ term presented in Eq. 4.3. Besides, the incremental-iterative procedure used here is the same as the one presented in chapter 3, Fig. 13. However, here, the $\sigma_{criterion}$, is obtained using the equations previously presented.

4.3 Applications

Three applications demonstrate the accuracy of the proposed dipole-based BEM formulation for modelling the three-dimensional fracture of quasi-brittle materials accounting for different loading velocities rates. The first application deals with a parallelepiped concrete specimen under a simple tensile test. The second application handles the three-point bending concrete beam. It is worth mentioning that both applications account pure mode I crack growth modelling. Finally, in the third application, a L-shaped concrete specimen demonstrates the performance of the proposed formulation in mixed mode crack propagation modelling. The results achieved by the proposed formulation have been compared to analytical and experimental responses available in the literature. The nonlinear system of equations accounts for a tolerance of convergence equal 10^{-2} based on the norm of non-equilibrated stress values.

4.3.1 Application 1: Parallelepiped solid specimen on simple tensile test

The first application deals with the fracture modelling of a parallelepiped solid subjected to a pure tensile loading. The proposed dipole-based BEM formulation including the mechanical influence of different loading velocities rates describes the structural behaviour and models the cohesive crack growth process in pure mode I. The structure is clamped at its left end and subjected to a prescribed displacement at its right end. The prescribed displacement of $\bar{u} = 0.015\ m$ has been applied incrementally. Fig. 67a illustrates the structural geometry and material properties. Besides, the analytical reference results for this application are available in the literature (OLIVEIRA; LEONEL, 2013; ALMEIDA; LIMA JUNIOR; BARBIRATO, 2020a). The loading has been applied within 100 load steps. Fig. 67b illustrates the boundary mesh, which contains 360 collocation points and 250 quadrilateral isoparametric linear boundary elements.

The loading has been applied accounting for three different loading velocities rates, which are: $10^{-7}\ m/s$, $10^{-5}\ m/s$ and $10^{-3}\ m/s$. Furthermore, linear, bilinear and exponential updated cohesive laws describe the mechanical material behaviour. Fig. 36 illustrates the curves force versus displacement for the adopted updated cohesive laws as a function of the loading velocity rate. As expected, the increase on the loading velocity rate leads to an apparent increase on the tensile material strength. The fracture energy slightly reduces as a function of the loading velocity rate increase. This behaviour has been observed experimentally (RUSH, 1960; RUIZ *et al.*, 2010; SANTOS; SOUSA, 2020) and properly described by the proposed approach. Besides, the numerical responses provided by the proposed approach are in excellent agreement with the reference analytical predictions in quase-static condition (OLIVEIRA; LEONEL, 2013; ALMEIDA; LIMA JUNIOR; BARBIRATO, 2020a).

Figure 35 – Parallelepiped solid under pure tensile loading (a) Properties (b) Discretisation

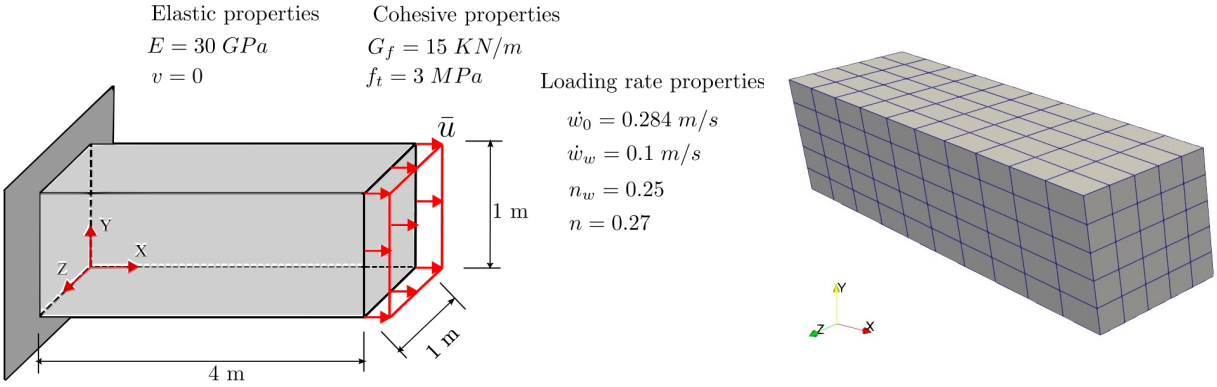

(a) (b)

Source: The author.

Figure 36 – Force versus displacement curves including loading velocities rate effects (a) Linear (b) Bilinear (c) Exponential considering analytical and numerical results

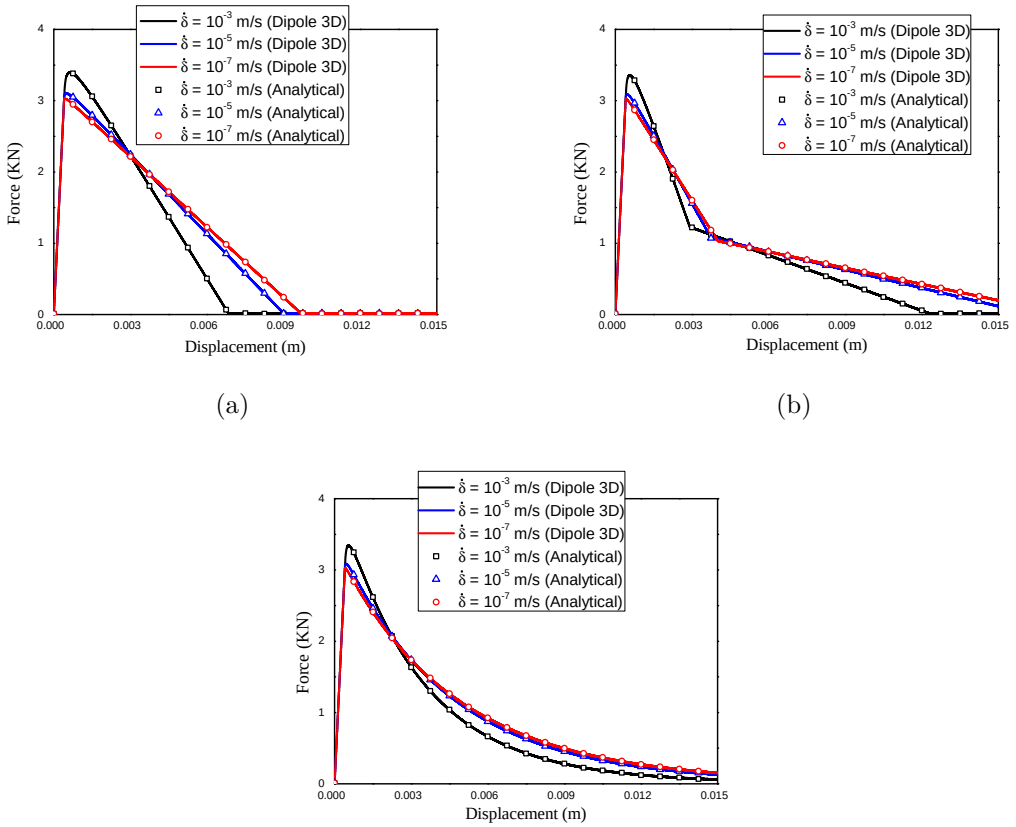

(a) (b)

(c)

Source: The author.

In Fig. 15, the results for displacements along X direction for the last load step with the loading velocity rate of 10^{-3} are presented. This figure illustrates the specimen fracture configuration and its separation in two parts. The right part keeps the prescribed displacement value whereas the left part has nil displacement value. Similar behaviour can be observed when the updated bilinear cohesive law is adopted. The predictions provided by the proposed formulation are in excellent agreement with the analytical reference results. Besides, the NLFM approach enabled an adequate phenomenological description of the mechanical degradation processes.

Figure 37 – Specimen fracture (linear cohesive law – Application 1) in colour scale (m)

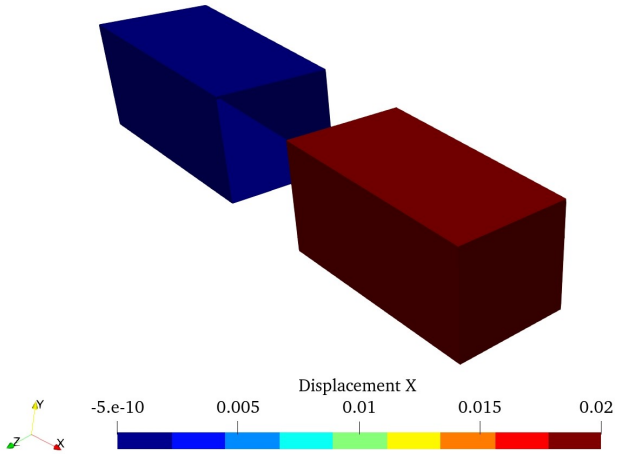

(a)

Source: The author.

4.3.2 Application 2: Three-point bending concrete specimen

The second application handles the fracture modelling of a concrete specimen in the three-point bending test. Santos and Sousa (2020) analysed experimentally this specimen and presents its material properties. Fig. 38 illustrates geometry, boundary conditions and material properties.

The loading has been applied at the structure mid-span upper surface, which is composed of the prescribed displacement of $\bar{u} = 0.35mm$. In addition, the loading has been applied within 200 load steps with the following velocities rates $8.33.10^{-4}$, $8.33.10^{-3}$ and $8.33.10^{-2}$. As illustrated in Fig. 38b, 3,441 collocation points and 2,900 quadrilateral isoparametric linear boundary elements compose the boundary mesh. Besides, linear, bilinear and exponential cohesive laws describe the mechanical material behaviour at the energy dissipation zone.

In Fig. 39, the responses achieved by the proposed numerical formulation, for all cohesive laws, and the experimental results (SANTOS; SOUSA, 2020), which involve force

and displacement values, are provided. The displacements have been measured at the crack mouth whereas the force values have been obtained at the mid-span upper surface. The proposed numerical formulation describes properly the elastic domain for all loading velocities rates considered in the experimental analyses. Besides, good agreement between numerical and experimental responses is observed for the peak load in the lower loading velocity rate. As the loading velocity rate increases, the numerical predictions tend to agree with the experimental values observed in the lower envelope. Finally, the three cohesive laws previously mentioned describe adequately the softening behaviour. Nevertheless, the bilinear and exponential laws enabled the best fit with the experimental predictions for all loading velocities rates accounted in the experimental analyses.

Figure 38 – Three-point bending test (a) Properties (b) Discretisation

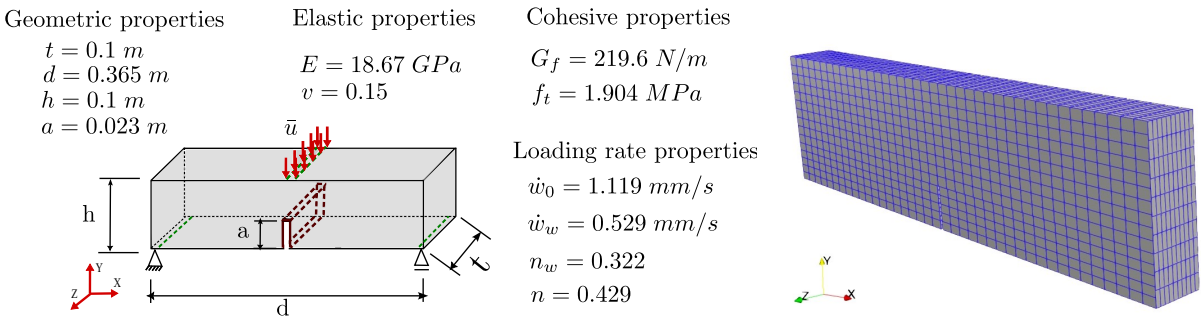

(a) (b)

Source: The author.

In Fig. 40, the evolution of cohesive stress versus crack opening displacement values for all loading velocities rates considered in the experimental analyses is presented. Thus, as expected, the loading velocity rate growth leads to the apparent increase in the tensile strength and the decrease in the apparent fracture energy. This behaviour has been experimentally presented in (RUSH, 1960; RUIZ *et al.*, 2010; SANTOS; SOUSA, 2020). Besides, the threshold crack open reduces as the loading velocity rate increases. Thus, the growth on the loading velocity rate tends to modify the failure material processes from quasi-brittle to brittle. In Fig. 40d, its noticeable the higher peak load with increasing loading rates.

For sake of completeness, Fig. 41 illustrates the crack growth path for two different load steps when the loading velocity rate is $\dot{\delta} = 8{,}33 \cdot 10^{-2}\ mm/s$. The crack grows in pure mode I, as expected. Besides, the fracture is not observed despite the large crack surface length. The dipole-based formulation required 30.4 minutes for the entire nonlinear analysis with linear cohesive law (the other laws required similar CPU time).

Figure 39 – Force *versus* displacement curves including three loading rates

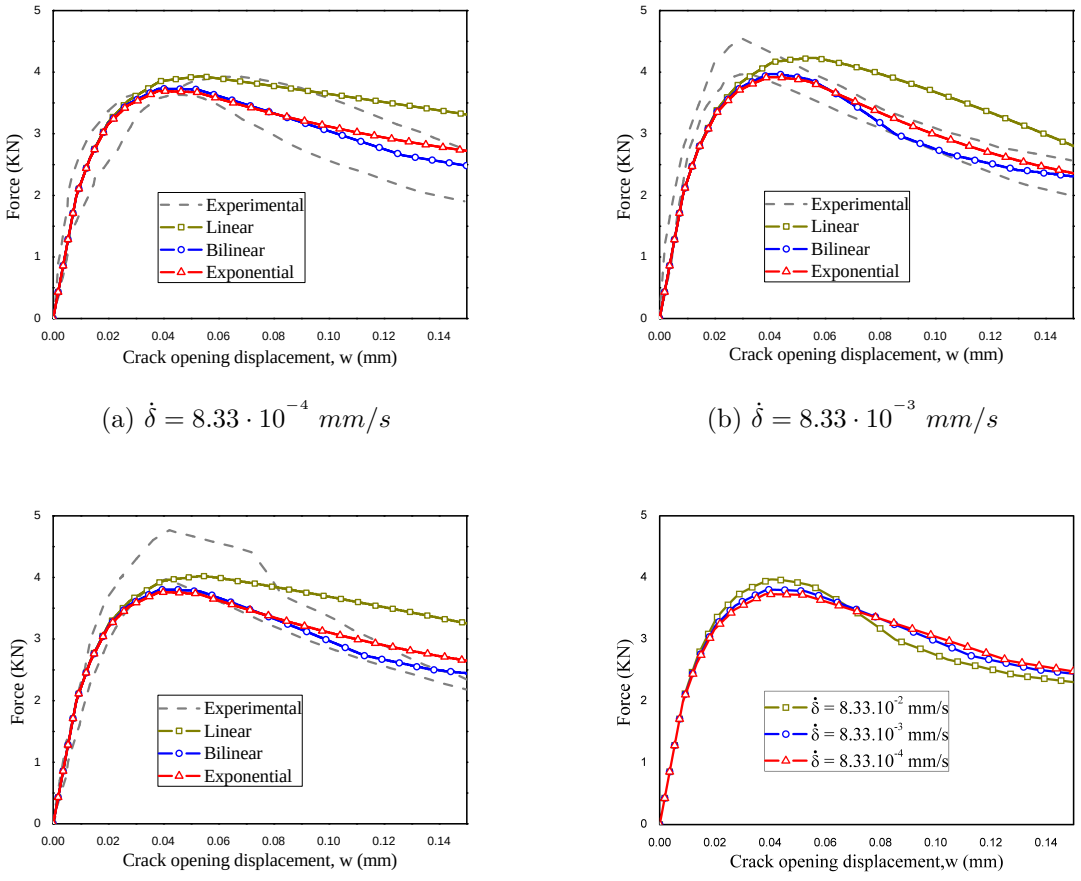

(a) $\dot{\delta} = 8.33 \cdot 10^{-4}\ mm/s$

(b) $\dot{\delta} = 8.33 \cdot 10^{-3}\ mm/s$

(c) $\dot{\delta} = 8.33 \cdot 10^{-2}\ mm/s$

(d) Bilinear cohesive law

Source: The author.

Figure 40 – Curves $\sigma(MPa)$ *versus* crack opening displacement, $w(mm)$, for all cohesive laws and loading rates applied

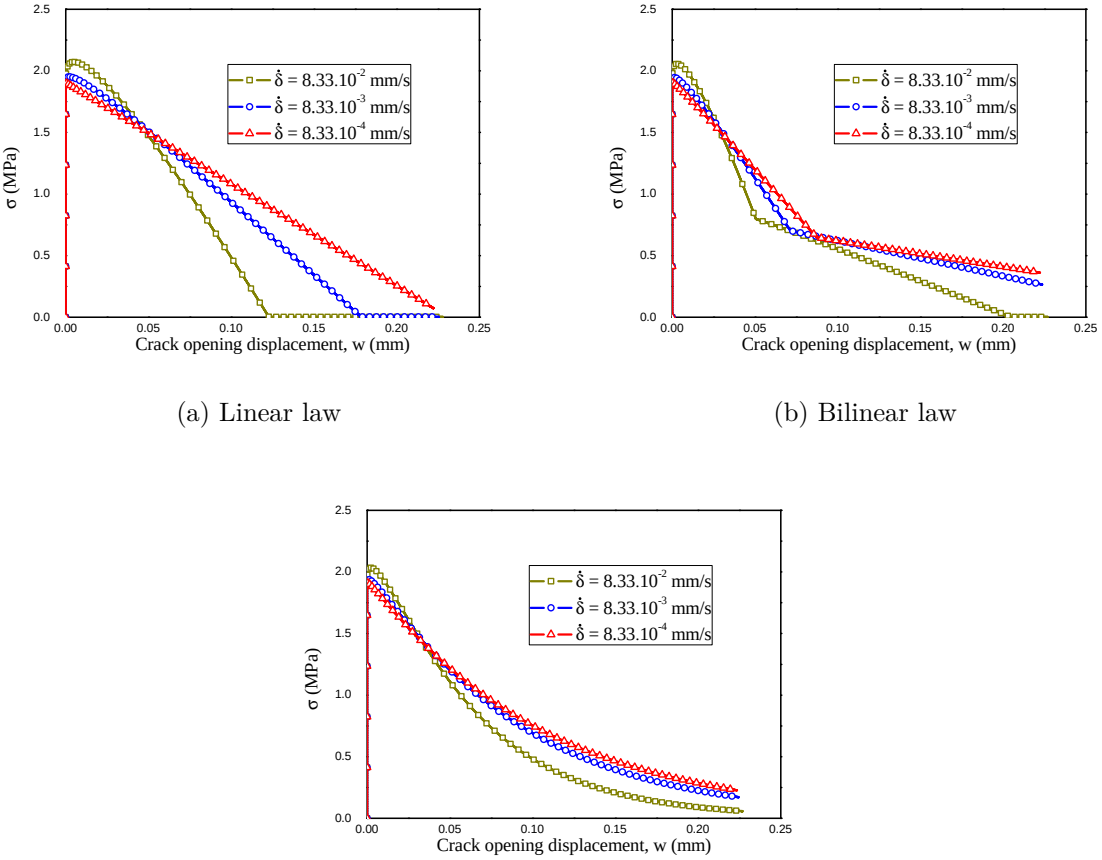

(a) Linear law

(b) Bilinear law

(c) Exponential law

Source: The author.

Figure 41 – Crack propagation path (linear cohesive law – Application 2) in colour scale (m)): 34 load steps (a); 200 load steps

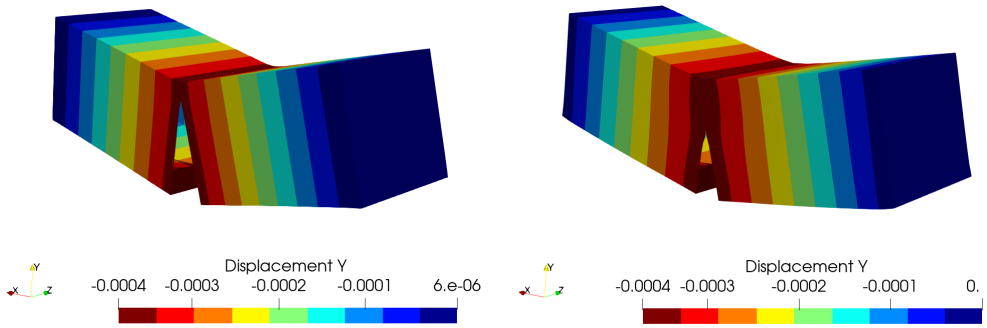

(a)

(b)

Source: The author.

4.3.3 Application 3: L-shaped concrete specimen under mixed mode propagation

The last application analyses the cohesive fracture of the L-shape structure illustrated in Fig. 42. Winkler (2001) analysed experimentally this structure and determined the fracture failure under quasi-static condition. Thus, this application demonstrates the accuracy of the proposed dipole-based formulation in modelling mixed-mode crack propagation in nonlinear regime and provides benchmark results for further viscous-cohesive formulations. Fig. 42a illustrates geometry dimensions, boundary conditions and material properties. The experimental study of Winkler (2001) provides the elastic and cohesive material properties whereas the experimental analysis of Santos and Sousa (2020) leads to the viscous material properties.

The numerical modelling via the dipole-based formulation utilises the same boundary mesh presented in Fig. 23b (2630 collocation points and 2250 quadrilateral isoparametric linear boundary elements). Besides, the loading has been applied within 200 load steps. For sake of simplicity, the mechanical modelling utilises solely the bilinear cohesive law because of the accurate results provided by this law in the previous applications. The analysis has been carried out in quasi-static conditions and in loading velocity variation. In the latter case, the following velocities have been assumed: $\dot{\delta} = 2.38 \cdot 10^{0}\ mm/s$, $\dot{\delta} = 2.38 \cdot 10^{-1}\ mm/s$, and $\dot{\delta} = 2.38 \cdot 10^{-3}\ mm/s$. Besides, the quasi-static case was also considered.

Figure 42 – L-shaped concrete specimen properties

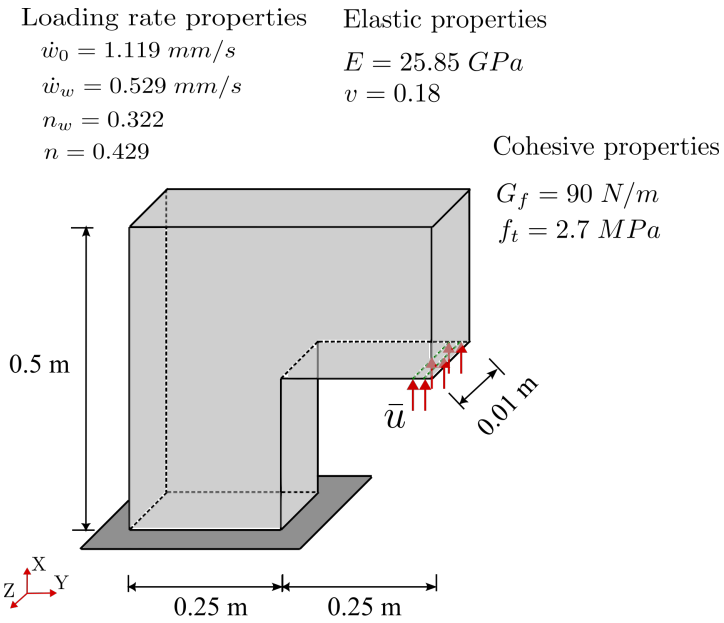

Source: The author.

in Fig. 43a, the curves force *versus* displacement are presented. The responses provided by the proposed dipole-based formulation in quasi-static condition and in low loading velocity are in good agreement with the experimental values provided by Winkler

(2001). In these cases, the elastic part is accurately described as well as the peak load value. Besides, the softening behaviour is adequately modelled in both cases.

In the viscous cohesive modelling, the peak load value increases as the loading velocity rate increases, as expected. In addition, the fracture energy values have been modified accordingly, which lead to the tendency of brittleness as the loading velocity rates increase.

In Fig. 43b, the evolution of cohesive stresses values as a function of crack opening displacement is presented. This figure demonstrates the loading velocity rate influence on the materials properties. As expected, the tensile material strength grows as the loading velocity rate increases.

Figure 43 – Force curve *versus* displacement for the adopted rates (b) σ *versus* crack opening displacement (w)

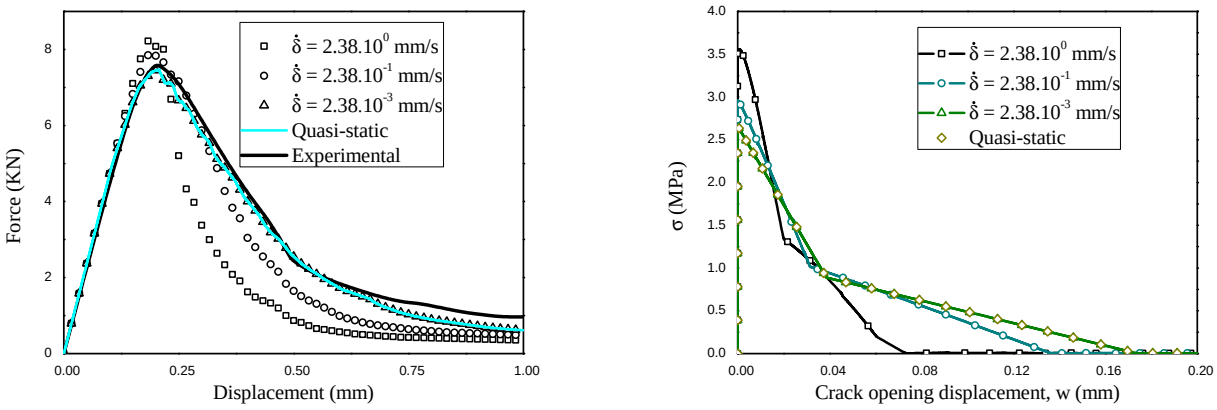

(a) (b)

Source: The author.

In Fig. 44, the displacement field and the crack growth path for loading velocity rate of $\dot{\delta} = 2.38 \cdot 10^{0}\ mm/s$ is presented. The crack grows in mixed-mode and triggers the displacement discontinuity at the body's boundaries.

Figure 44 – Crack path and displacement (m) in colour scale (m): 41st load step (a); 200th load step (b)

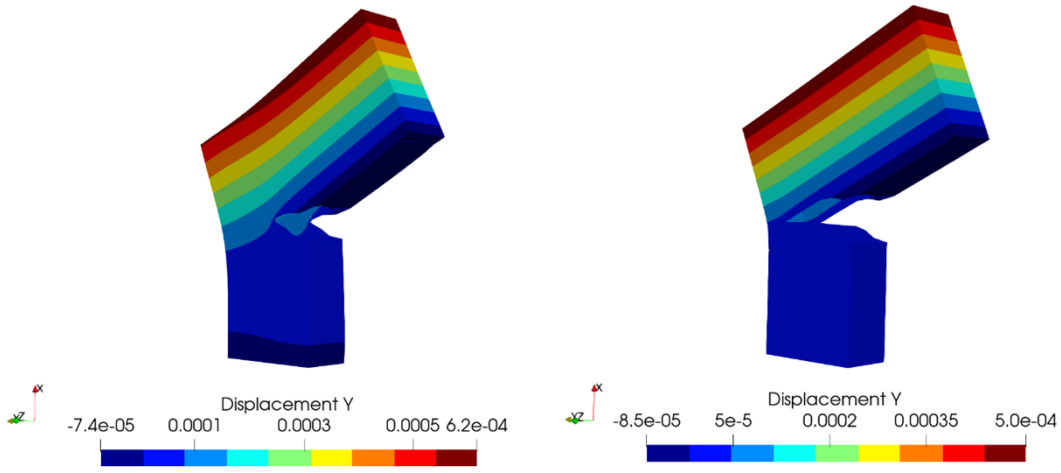

(a) (b)

Source: The author.

5 PARK-PAULINO-ROESLER COHESIVE MODEL

There are various drawbacks to efficient displacement-based models of cohesive zones. Potential-based models, have been created to overcome some of these obstacles. Park, Paulino and Roesler (2009) proposed an unified potential-based cohesive model capable of representing a wide variety of materials, and also different fracture energies, by choosing appropriate parameters. Instead of using the effective displacement (w), cohesive tensile separation formulas were developed based on a potential that is a function of the normal and tangential separations (w, w_t). Normal cohesive traction are provided by the derivative of a potential with regard to the normal separation, while tangential cohesive traction is obtained by the derivative of a potential with respect to the tangential separation. The cohesive traction derived from potential-based models represents monotonic material separation processes, as one must note. A potential-based model may include additional constitutive relationships if additional physical phenomena are taken into consideration, such as fatigue loading, contact and frictional sliding along the fracture surface (CORDEIRO; DAUMAS; MONTEIRO, 2024).

There are two distinct categories of cohesive-zone models, namely, intrinsic models and extrinsic models. The main difference between then is the presence of the initial slope in the traction-separation curve. For intrinsic models, the traction T first increases with the increase of the displacement discontinuities w till it reaches a maximum value (cohesive strength). The intrinsic PPR CZM is used in this work, enabling the adjust of pre-peak curve inclination by introducing initial slope parameters

5.1 PPR CZM formulation

The Park-Paulino-Roesler (PPR) cohesive zone model (PARK; PAULINO, 2012) propose a unified model suitable for different types of materials. This model can represent a wide variety of materials, e.g., brittle, plateau, and quasi-brittle, by introducing shape parameters (α and β) that control the post-peak behaviour. In addition, this model can represent fracture energies for mode I and II. The potential of cohesive fracture, according to PPR cohesive model (PARK; PAULINO, 2012) is given by:

$$\psi(w,w_{t1},w_{t2}) = min(G_f,G_t) + F_n(w)F_t(w_{t1},w_{t2}) \tag{5.1}$$

where w is the normal crack opening displacement, w_{t1} and w_{t2} are the tangential crack opening displacements, G_f is the normal fracture energy (mode I), G_t is the tangential fracture energy (mode II). To achieve the cohesive tractions, we have to define the functions F_n and F_t, which are related to normal and tangential crack opening displacements, respectively,

$$F_n(w) = \Gamma_n \left(1 - \frac{w}{w_c}\right)^{\alpha} \left(\frac{m}{\alpha} + \frac{w}{w_c}\right)^{m} + \langle G_f - G_t \rangle \tag{5.2}$$

$$F_t(w_t) = \Gamma_t \left(1 - \frac{w_t}{w_{ct}}\right)^{\beta} \left(\frac{n}{\beta} + \frac{w_t}{w_{ct}}\right)^{n} + \langle G_t - G_f \rangle \tag{5.3}$$

where w_c and w_{ct} are the normal and tangential critical crack opening displacements, respectively, α and β, are the shape parameters, (Γ_n, Γ_t), are the energy constraints, m and n, are non-dimensional exponents, and $\langle . \rangle$ is the Macaulay bracket, i.e.

$$\langle x \rangle = \begin{cases} 0 & (x < 0), \\ x & (x \geqslant 0) \end{cases} \tag{5.4}$$

The shape parameters α and β are introduced to model several material fracture behaviour, e.g., brittle, plateau, and quasi-brittle. According to Park and Paulino (2012), $\alpha = [2 - 5]$ induced a quasi-brittle behaviour for the normal tractions T_n, while $\beta = 1.3$ induced a plateau behaviour for the tangential tractions T_t. The non dimensional exponents m and n are defined in terms of initial slope parameters λ_n and λ_t:

$$m = \frac{\alpha\,(\alpha - 1)\,\lambda_n^2}{(1 - \alpha\lambda_n^2)} \qquad n = \frac{\beta\,(\beta - 1)\,\lambda_t^2}{(1 - \beta\lambda_t^2)} \tag{5.5}$$

Besides, the energy constraints (Γ_n, Γ_t) are expressed as a function of the fracture energies G_f and G_t:

$$\Gamma_n = -G_f^{\frac{\langle G_f - G_t \rangle}{G_f - G_t}} \left(\frac{\alpha}{m}\right)^{m} \qquad \Gamma_t = -G_t^{\frac{\langle G_t - G_f \rangle}{G_t - G_f}} \left(\frac{\beta}{n}\right)^{n} \; for \;\; G_f \neq G_t \tag{5.6}$$

$$\Gamma_n = -G_f \left(\frac{\alpha}{m}\right)^{m} \qquad \Gamma_t = -G_t \left(\frac{\beta}{n}\right)^{n} \; for \;\; G_f = G_t \tag{5.7}$$

The initial slope (pre-peak curve inclination) can also be adjusted in the PPR cohesive model, a feature not shared in the traditional linear, bilinear and exponential (ALMEIDA; LIMA JUNIOR; BARBIRATO, 2020a) cohesive methods. Further, the initial slope parameters λ_n and λ_t are here defined as $\lambda_n = 0.005$ and $\lambda_t = 0.005$ (PARK;

PAULINO, 2012). Finally, the critical crack opening displacements, w_c and w_{ct} are determined following the above relationships:

$$w_c = \frac{G_f}{f_t}\alpha\left(1-\lambda_n\right)^{\alpha-1}\left(\frac{\alpha}{m}+1\right)\left(\frac{\alpha}{m}\lambda_n+1\right)^{m-1} \tag{5.8}$$

$$w_{ct} = \frac{G_t}{\tau_t}\beta\left(1-\lambda_t\right)^{\beta-1}\left(\frac{\beta}{n}+1\right)\left(\frac{\beta}{n}\lambda_t+1\right)^{n-1} \tag{5.9}$$

where f_t is the normal cohesive strength and τ_t is the tangential cohesive strength.

The PPR-cohesive model also allows the generalisation of crack propagation modelling to three dimensional components. The three cohesive tractions T_n, T_{t1}, and T_{t2} are dependent upon the normal separation, w, and two sliding displacements, w_{t1} and w_{t2}, Fig. 45.

The effective sliding displacement, w_t, is given by

$$w_t = \sqrt{(w_{t1}^2)+(w_{t2}^2)} \tag{5.10}$$

The tangential cohesive tractions, T_{t1} and T_{t2}, relate to w_t as follows:

$$T_{t1}(w,w_{t1},w_{t2}) = \frac{w_{t1}}{w_t}T_t(w,w_t) \tag{5.11}$$

$$T_{t2}(w,w_{t1},w_{t2}) = \frac{w_{t2}}{w_t}T_t(w,w_t) \tag{5.12}$$

where T_t is an effective tangential traction. Thus, the vector T_t is composed by two tangential components, T_{t1} and T_{t2}.

Figure 45 – Cohesive element collapsed and deformed with separations demarcated

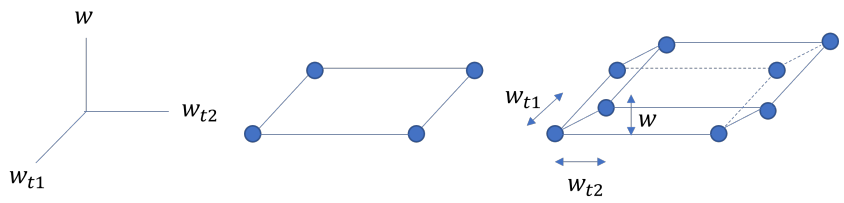

Source: The author.

It is interesting to rewrite the potential of cohesive fracture as a stress function. Thus, The derivatives of the potential as a function of the crack opening displacements, w and w_t, Eq. 5.1, leads to the traction vector:

$$\mathbf{T} = \frac{\partial\psi}{\partial w} = \begin{Bmatrix} \frac{\partial\psi}{\partial w} \\ \frac{\partial\psi}{\partial w_t} \end{Bmatrix} = \begin{Bmatrix} T_n \\ T_t \end{Bmatrix} \tag{5.13}$$

in which $T_n(w,w_t) = \partial\psi/\partial w = F_n^{'}F_t$ and $T_t(w,w_t) = \partial\psi/\partial w_t = F_t^{'}F_n$. The shear tractions, T_{t1} and T_{t2}, are subsequently determined from Eq. 5.11. Besides, the derivatives of functions F_t and F_n are expressed as:

$$F_n^{'}(w) = \frac{\partial F_n}{\partial w} = \frac{\Gamma_n}{w_c}\left[m\left(1-\frac{w}{w_c}\right)^{\alpha}\left(\frac{m}{\alpha}+\frac{w}{w_c}\right)^{\alpha-1} - \alpha\left(1-\frac{w}{w_c}\right)\alpha - 1\left(\frac{m}{\alpha}+\frac{w_n}{w_c}\right)^{m}\right] \tag{5.14}$$

$$F_t^{'}(w_t) = \frac{\partial F_t}{\partial w_t} = \frac{w_t}{|w_t|}\frac{\Gamma_t}{w_{ct}}\left[n\left(1-\frac{|w_t|}{w_{ct}}\right)^{\beta}\left(\frac{n}{\beta}+\frac{|w_t|}{w_{ct}}\right)^{\beta-1} - \beta\left(1-\frac{|w_t|}{w_{ct}}\right)\beta - 1\left(\frac{n}{\beta}+\frac{|w_t|}{w_{ct}}\right)^{n}\right] \tag{5.15}$$

The normal and tangential cohesive tractions T_n and T_t can be generally related to the normal and tangential crack opening displacements, w and w_t, by the cohesive stiffness K_n and K_t. Besides, the bar under the parameters indicates the local coordinate system,

$$\begin{Bmatrix}\bar{T}_n(w)\\ \bar{T}_t(w_t)\end{Bmatrix} = \begin{Bmatrix}\bar{K}_n(w,w_t) & 0\\ 0 & \bar{K}_t(w,w_t)\end{Bmatrix}\begin{Bmatrix}w\\ w_t\end{Bmatrix} = \bar{\mathbf{T}} = \bar{\mathbf{K}}(\bar{\mathbf{w}})\bar{\mathbf{w}} \tag{5.16}$$

The normal and tangential cohesive stiffness are defined as follows:

$$\bar{K}_n(w,w_t) = \frac{\bar{T}_n(w)}{w} = \frac{\partial\psi}{\partial w}\frac{1}{w} = \frac{F_n^{'}(w)F_t(w_t)}{w} \tag{5.17}$$

$$\bar{K}_t(w,w_t) = \frac{\bar{T}_t(w_t)}{w_t} = \frac{\partial\psi}{\partial w_t}\frac{1}{w_t} = \frac{F_n^{'}(w_t)F_t(w_t)}{w_t} \tag{5.18}$$

It is important emphasising that the Eq. 5.16 have been written in the local coordinate system, x_i. However, the nonlinear crack growth solution requires the transformation in the global coordinate system, X_i. Thus, regarding the coordinate transformation:

$$\bar{\mathbf{T}}(w,w_t) = \bar{\mathbf{K}}(\bar{\mathbf{w}})\bar{\mathbf{w}} \Rightarrow \mathbf{R}^T\mathbf{T}(w,w_t) = \bar{\mathbf{K}}(\bar{\mathbf{w}})\mathbf{R}^T\mathbf{w} \Rightarrow \mathbf{T}(w,w_t) = \mathbf{R}\bar{\mathbf{K}}(\bar{\mathbf{w}})\mathbf{R}^T\mathbf{w} \tag{5.19}$$

where R is the transformation matrix and is defined as:

$$R = \begin{bmatrix}\bar{m}_1 & \bar{m}_2 & \bar{m}_3\\ \bar{s}_1 & \bar{s}_2 & \bar{s}_3\\ \bar{n}_1 & \bar{n}_2 & \bar{n}_3\end{bmatrix} \tag{5.20}$$

where m_k, s_k and n_k are the cosines with normal direction.

Finally, the quasi-static PPR cohesive model can be defined as:

$$\mathbf{T} = \mathbf{K}(\bar{\mathbf{w}})\mathbf{w} \tag{5.21}$$

where the vector **T** contains the cohesive stress components and vector **w** contains the normal and tangential crack openings. T can be also identified as $\sigma_{criterion}$, section 3.1. However, here, T contains normal and tangential stress components. Eq. 5.21 defines the normal and tangential cohesive stress considering quasi-brittle behaviour for mode I, and plateau-type behaviour for modes II and III. Therefore, the PPR-cohesive model penalises the material in the three cohesive-propagation modes, I, II and III. Fig. 46 presents the nonlinear behaviour for the unified mixed-mode potential considering the shape parameters.

Figure 46 – Fracture behaviour for the unified mixed-mode potential.

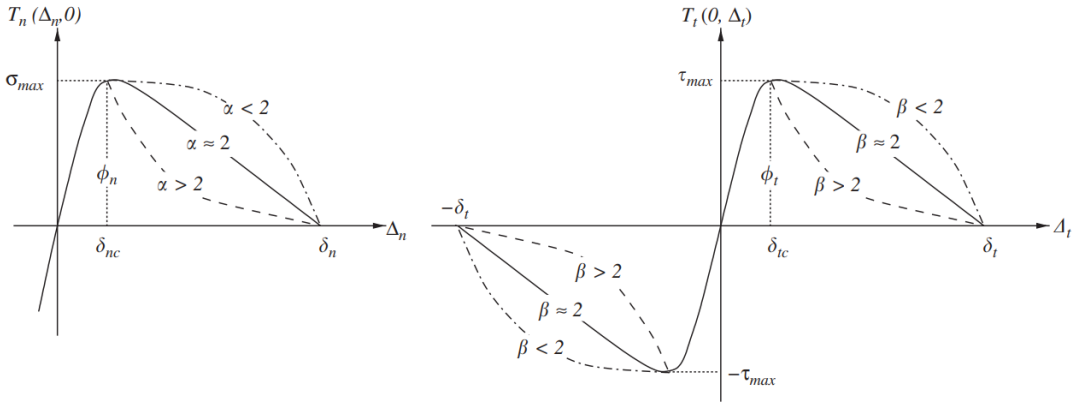

Source: Park, Paulino and Roesler (2009)

An example of PPR model is illustrated in Fig. 47 for the following parameters: $G_f = 100\ N/m$, $G_t = 200\ N/m$, $f_t = 40\ MPa$, $\tau_t = 30\ MPa$, $\alpha = 5$, $\beta = 1.3$, $\lambda_n = 0.1$, $\lambda_t = 0.2$. The shape parameters α and β control the post-peak behaviour (enabling the modelling of different materials) and the initial slope indicators λ_n and λ_t enable the adjustment of the initial cohesive stiffness (the pre-peak curve).

Figure 47 – PPR cohesive zone model considering $G_f = 100\ N/m$, $G_t = 200\ N/m$, $f_t = 40\ MPa$, $\tau_t = 30\ MPa$, $\alpha = 5$ and $\beta = 1.3$

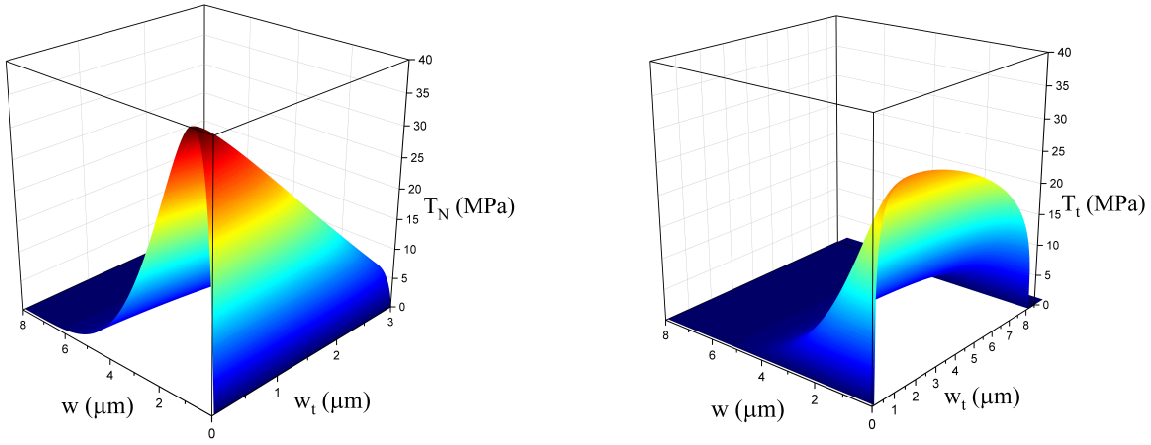

(a) Normal cohesive stress, T_n

(b) Tangential cohesive stress, T_t

Source: The author.

5.1.1 The updated PPR cohesive law

The following modification enables the viscous effects at the FPZ by rewriting the PPR cohesive model as a function of the loading rate dependent fracture, $G(\dot{w})$. Thus, we propose an updated PPR cohesive zone model to account for the loading velocity rate influence at the FPZ, which is another novelty herein. This modification is defined as follows:

First, the functions $F_n(w,G(\dot{w}))$ and $F_t(w,G(\dot{w}))$, Eq. 5.2 and Eq. 5.3, are updated for account the loading velocity rate influence:

$$F_n(w,G(\dot{w})) = \Gamma_n \left(1 - \frac{w}{w_c^{up}}\right)^{\alpha} \left(\frac{m}{\alpha} + \frac{w}{w_c^{up}}\right)^{m} + \langle G_f - G_t \rangle \tag{5.22}$$

$$F_t(w_t,G(\dot{w})) = \Gamma_t \left(1 - \frac{w_t}{w_{ct}^{up}}\right)^{\beta} \left(\frac{n}{\beta} + \frac{w_t}{w_{ct}^{up}}\right)^{n} + \langle G_t - G_f \rangle \tag{5.23}$$

in which w_c^{up} and w_{ct}^{up} indicate the updated values for w_c and w_{ct} respectively. Thus, $w_c^{up} = G(\dot{w})w_c$ and $w_{ct}^{up} = G(\dot{w})w_{ct}$. Besides, the derivatives of the functions $F_n(w,G(\dot{w}))$ and $F_t(w,G(\dot{w}))$, Eq. 5.14 and Eq. 5.15, are rewritten as:

$$\begin{aligned} F_n'(w,G(\dot{w})) = \frac{\partial F_n}{\partial w} = \frac{\Gamma_n}{w_c^{up}} \Bigg[m \left(1 - \frac{w}{w_c^{up}}\right)^{\alpha} \left(\frac{m}{\alpha} + \frac{w}{w_c^{up}}\right)^{\alpha-1} - \\ -\alpha \left(1 - \frac{w}{w_c^{up}}\right) \alpha - 1 \left(\frac{m}{\alpha} + \frac{w_n}{w_c^{up}}\right)^{m} \end{aligned} \tag{5.24}$$

$$F_t^{'}(w_t,G(\dot{w})) = \frac{\partial F_t}{\partial w_t} = \frac{w_t}{|w_t|}\frac{\Gamma_t}{w_{ct}^{up}}\left[n\left(1-\frac{|w_t|}{w_{ct}^{up}}\right)^{\beta}\left(\frac{n}{\beta}+\frac{|w_t|}{w_{ct}^{up}}\right)^{\beta-1} - \right.$$
$$\left. -\beta\left(1-\frac{|w_t|}{w_{ct}^{up}}\right)\beta-1\left(\frac{n}{\beta}+\frac{|w_t|}{w_{ct}^{up}}\right)^{n}\right. \tag{5.25}$$

In addition, the normal and tangential updated cohesive stiffness, Eq. 5.17 and Eq. 5.18, are rewritten as:

$$K_n(w,w_t,G(\dot{w})) = \frac{F_n^{'}(w,G(\dot{w}))F_t(w_t,G(\dot{w}))}{w} \tag{5.26}$$

$$K_t(w,w_t,G(\dot{w})) = \frac{F_n^{'}(w,G(\dot{w}))F_t(w_t,G(\dot{w}))}{w} \tag{5.27}$$

Finally, the updated PPR cohesive zone model (PARK; PAULINO, 2012), after the coordinate transformation, Eq. 5.20, is governed by the following equation:

$$\mathbf{T}(\mathbf{w},\mathbf{G}(\dot{\mathbf{w}})) = f(\mathbf{w},\mathbf{G}(\dot{\mathbf{w}})) = K(\bar{\mathbf{w}},\mathbf{G}(\dot{\mathbf{w}}))\mathbf{w} \tag{5.28}$$

$\mathbf{T}(\mathbf{w},\mathbf{G}(\dot{\mathbf{w}})$ refers to the PPR cohesive law modified by the fracture energy dependent on the loading rate, $G(\dot{w})$. Finally, Eq. 5.28 is introduced in Eq. 4.3, section 4.1, enabling the loading-rate influence. Therefore, the last equation of the updated PPR CZM is:

$$\sigma(\dot{\mathbf{w}},\mathbf{w})_{cohesive} = \Psi(\dot{\mathbf{w}})\mathbf{T}(\mathbf{w},\mathbf{G}(\dot{\mathbf{w}})) \tag{5.29}$$

The details about the Santos and Sousa (2020) viscous-cohesive model have been presented in chapter 4.

5.2 Flowchart of the 3D PPR dipole-based procedure

The incremental-iterative procedure is similar from that one presented in section 3.8. However, here, the $\sigma_{cohesive}$ is the cohesive stress introduced by the updated PPR cohesive law, section 5.1. Besides, the fracture energy rate, $G(\dot{w})$ is written as a function of crack opening displacement rate, $\dot{w}$, enabling the viscous effects.

Figure 48 – Incremental-iterative procedure and updated PPR cohesive model from viscous-cohesive 3D dipole-based BEM formulation

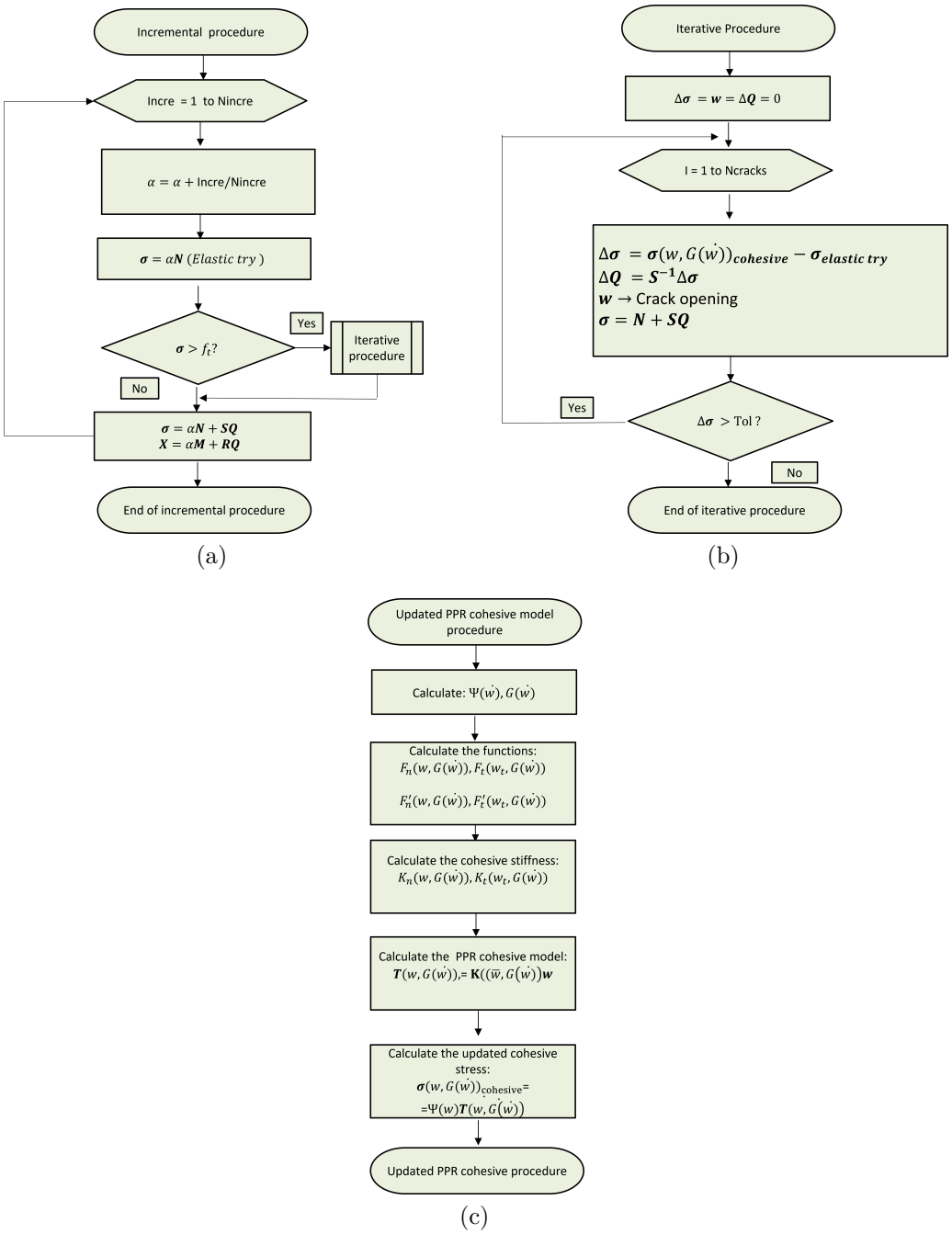

Source: The author.

5.3 Applications

Four applications demonstrate the accuracy of the proposed PPR dipole-based BEM formulation for modelling the three-dimensional fracture of quasi-brittle materials. The first application deals with a parallelepiped concrete specimen under a simple tensile

test. The second application handles the fracture modelling of a parallelepiped solid under mode II propagation. The third application handles the crack propagation modelling in a geometrically complex concrete specimen subjected to fully mixed-mode fracture. Finally, in the last application, two groups of concrete tested at three-point bending including loading rates and experimentally performed by Santos and Sousa (2020), are presented. The results achieved by the proposed formulation have been compared to analytical and experimental responses available in the literature. The system of nonlinear equations accounts for a convergence tolerance equal to 10^{-2} based on the norm of unbalanced stress values.

5.3.1 Application 1: Parallelepiped solid under mode I

The first application deals with the fracture modelling of a parallelepiped solid subjected to mode I and mode II. The structure is clamped at its left end and subjected to a prescribed displacement, $\bar{u} = 0.08\,mm$, that is represented by the blue colour. Fig. 49a and Fig. 49b illustrates the structural geometry, elastic, cohesive and PPR properties considering the solid under mode I and mode II, respectively. Fig. 49b illustrates the boundary mesh, which contains 150 quadrilateral isoparametric linear boundary elements. Besides, this analyses was also performed by Park and Paulino (2012). In Fig. 49a, the region where the discontinuity propagates is highlighted in red.

Figure 49 – Parallelepiped solid under mode I (a) discretisation (b)

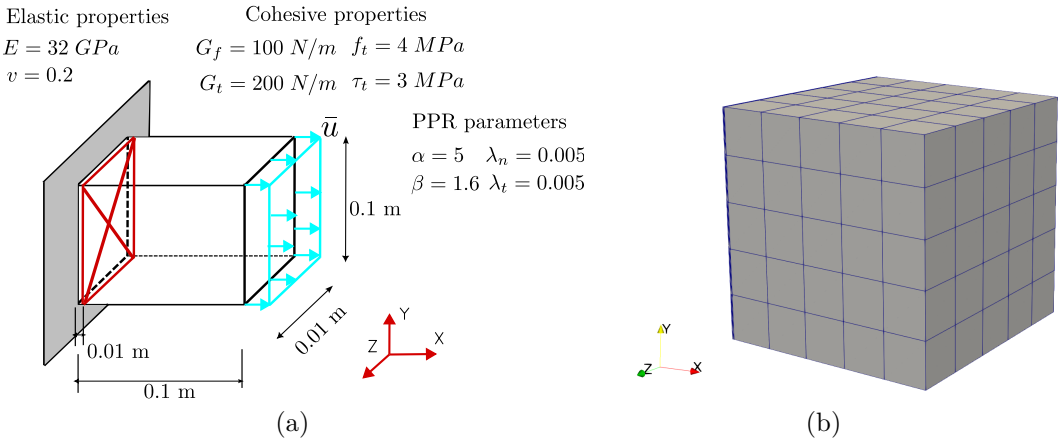

Source: The author.

In Fig. 50a, the normal stress *versus* displacement relationship is illustrated. It is important to mention that after the peak (close to 4 MPa), the solid presents softening behaviour, which is explained by the $\alpha = 5$ value adopted. The dipole-based BEM formulation provided good agreement with the results presented in Park and Paulino (2012).

Figure 50 – Normal cohesive stress (a) Crack propagation colour map (b)

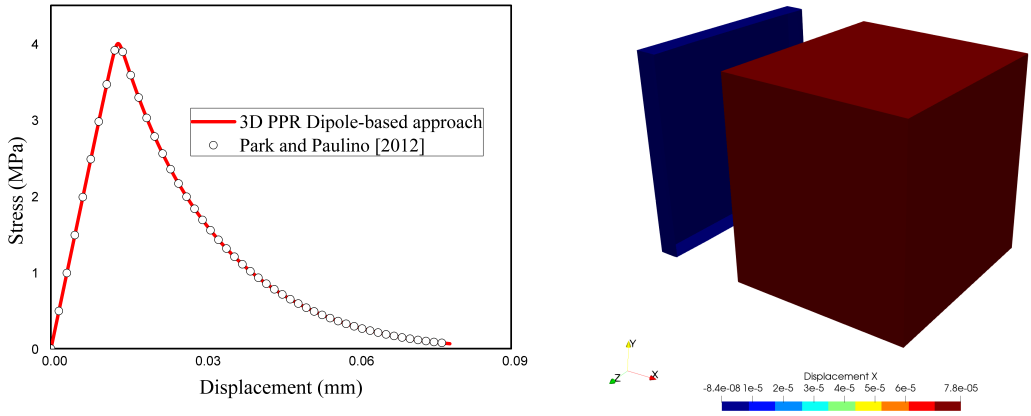

(a) (b)

Source: The author.

5.3.2 Application 2: Parallelepiped solid under mode II

The second application deals with the fracture modelling of a parallelepiped solid under pure mode II propagation. For the mode II problem, a square plate (0.1 m × 0.1 m) with diagonal cohesive interface is elongated and compressed at the top and right hand sides up to 0.08 mm. The principal stresses in this case are along the horizontal and vertical directions, and the maximum shear stress occurs along the 45° cohesive interface. The magnitude of the maximum shear stress is equal to the magnitude of the principal stresses. Fig. 51b illustrates the boundary mesh, which contains 150 quadrilateral isoparametric linear boundary elements. Besides, this analyses was also performed by Park and Paulino (2012). In Fig. 51a, the region where the discontinuity propagates is highlighted in red.

Figure 51 – Parallelepiped solid under mode II (a) discretisation (b)

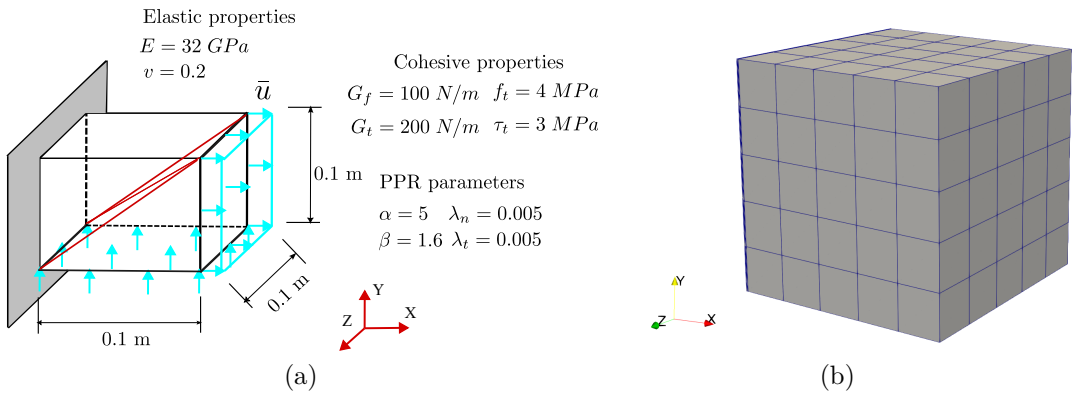

(a) (b)

Source: The author.

The maximum shear stress–displacements response is presented in Fig. 52. Note

that the maximum shear stress reaches the cohesive strength τ_t, followed by a softening behavior. The softening curve is concave because the mode II shape parameter β is less than 2.

Figure 52 – Shear cohesive stress

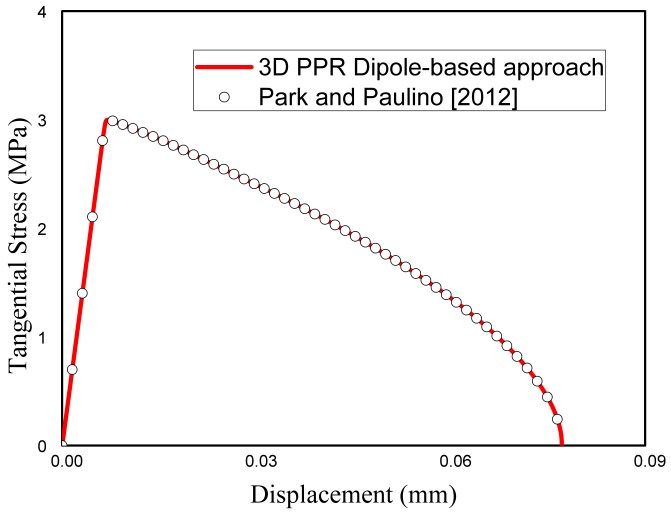

Source: The author.

Fig. 53 illustrates the displacement results provided by the dipole-based formulation along Y direction in two different load steps (a) 41 and (b) 200. The shows that the crack propagates along 45°. This is plausible, since the maximum shear stress is in 45° direction.

Figure 53 – Crack path and displacement (m) in colour scale (m): 41st load step (a); 200th load step (b)

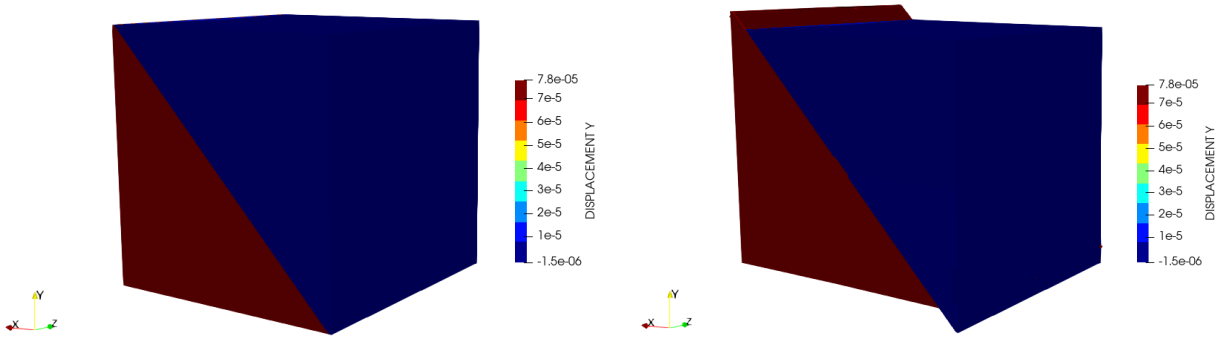

Source: The author.

5.3.3 Application 3: Geometrically complex concrete specimen subjected to mixed-mode fracture

The third application of this study deals with the crack propagation modelling in a geometrically complex concrete specimen subjected to fully mixed-mode fracture and combined modes I-II-III. This application provides benchmark results for further researches in nonlinear computational fracture mechanics field. Particularly, results within complex geometry and fracture modes context, which are complex tasks in experimental programs. Fig. 54a illustrates specimen's geometry, material properties and boundary conditions. The specimen has irregular parallelepiped geometry with an asymmetric notch positioned at its bottom surface. The loading has been applied at the specimen upper surface.

The proposed dipole-based formulation has been utilised in this essentially three-dimensional fracture problem. The boundary mesh adopted herein consists of 2250 linear quadrilateral boundary elements and 2630 collocation points, Fig. 54b. Besides, the external loading has been applied within 200 load steps and the PPR cohesive zone model the mechanical behaviour along the FPZ. Three α values ($\alpha = 2$,3 and 5) have been employed. Besides, $\beta = 1.6$, $\lambda_n = 0.005$ and $\lambda_t = 0.005$. The load is applied in $X = 0.2105$ m.

Figure 54 – Analysed specimen (a) Boundary discretisation (b)

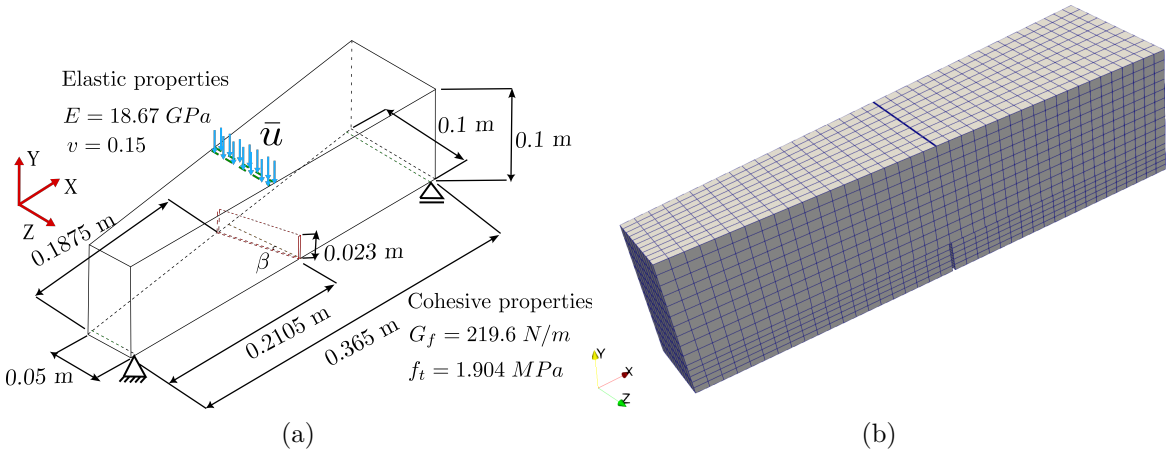

Source: The author.

The mechanical behaviour can be assessed by the evolution of force and displacement values as a function of external loading. The forces have been evaluated at the specimen upper surface and the displacements values involve the crack opening mouth displacement. Fig. 55a illustrates this evolution. The three α values employed herein enable the nonlinear post-peak behaviour. Similar behaviour can be observed in previous applications. As expected $\alpha = 2$ provides higher peak force values. In Fig. 55b, the cohesive stress curves are presented.

In Fig. 56, a comparative study between the classic cohesive laws (Linear, Bilinear

Figure 55 – Force versus crack mouth opening displacement curves (CMOD) (a) Cohesive stress versus CMOD (b).

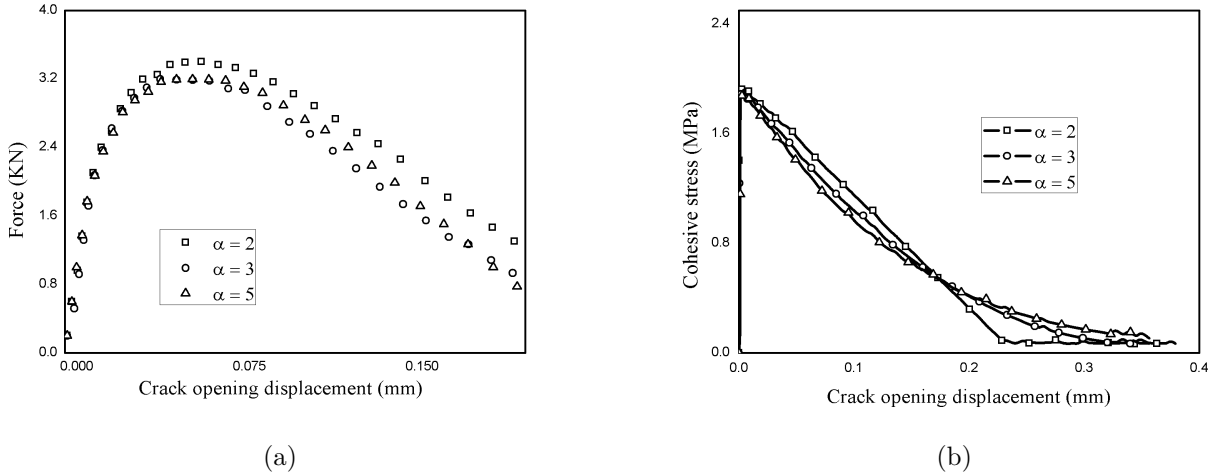

(a) (b)

Source: The author.

and Exponential), section 3.1, and the PPR CZM is presented. Slightly higher peak load values can be observed for the PPR model. Besides, when the α parameter is set to 2, the curve tends to align more closely with the linear model, whereas α values close to 5 tend to approximate the exponential/bilinear curves.

Figure 56 – Force versus crack mouth opening displacement curves considering classic cohesive laws and the PPR CZM.

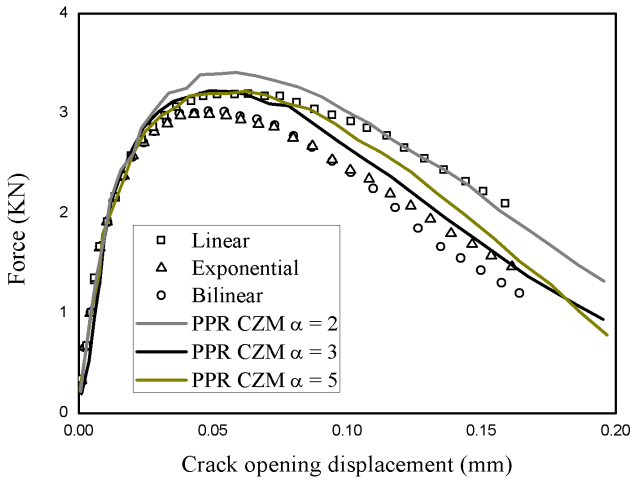

Source: The author.

Fig. 57 illustrates the displacement results provided by the dipole-based formulation along Y direction in two different load steps (linear cohesive law), (a) 50 and (b) 200. The figure shows the significant displacement discontinuity caused by the crack growth process. Additionally, the dipole-based formulation did not predict the structural collapse in spite

of the large extension of crack surfaces.

Figure 57 – Displacement along Y direction (a) 50 load step (b) 200 load step

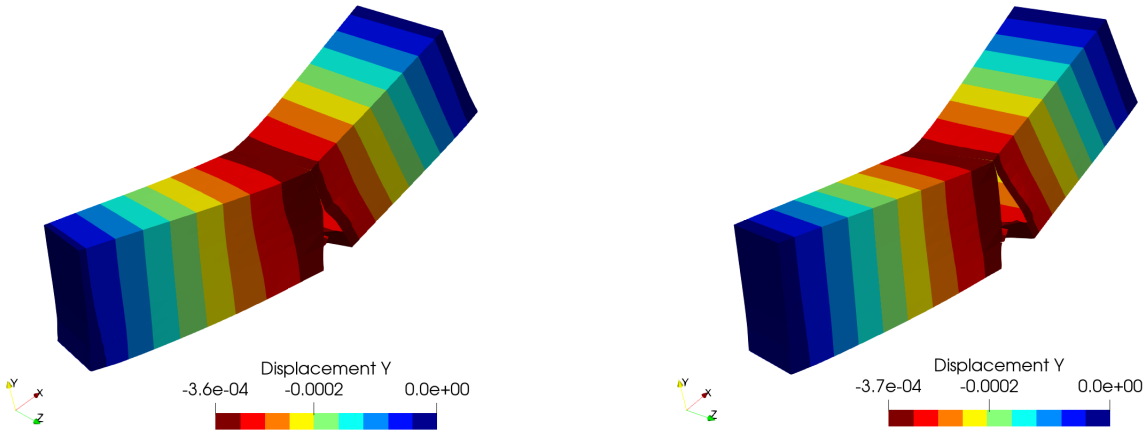

(a) (b)

Source: The author.

5.3.4 Application 4: Three-point bending concrete specimen including loading rates

Two groups of concrete tested at three-point bending including loading rates were experimentally performed by Santos and Sousa (2020). The first group is the conventional concrete, with a compressive strength of $f_c = 30\ MPa$, and a velocity of load application as $8.33 \cdot 10^{-3} mm/s$. The second group is the ultra-high strength concrete, with a strength of $f_c = 120\ MPa$, and $8.33 \cdot 10^{-3} mm/s$ as the loading rate. for both types of concrete, the beam has $d = 400$ mm in length, depth $h = 100$ mm, thickness $t = 100$ mm and notch depth $a = 23$ mm. Three experimental load-deflection curves were obtained for each case, (SANTOS; SOUSA, 2020). For both concretes, the PPR parameters were: $\alpha = 1.3;\ 2\,;5$ and 7, $\beta = 1.6$, $\lambda_n = 0.005$ and $\lambda_t = 0.005$.

A total of 200 load steps were introduced. The geometric properties and discretisation utilised are presented in Fig. 58. As illustrated in Fig. 58b, 3,441 collocation points and 2,900 quadrilateral isoparametric linear boundary elements compose the boundary mesh. Besides, the parameter P refers to the load applied.

5.3.4.1 Conventional concrete

A cohesive analysis of a three-point bending test (conventional concrete) considering different loading rates and α values, section 5.1, is presented. The nominal values of all parameters utilised in the analysis are presented in Fig. 58. The updated cohesive

stress, $\sigma(\dot{w},w)$, is determined considering the couple viscous-cohesive dipole-based BEM formulation and the PPR cohesive model, see Eq. 5.29. Besides, the quasi-static curve, Fig. 59e, refers to velocity loading rate equal $\dot{\delta} = 0$ mm/s. The influence of the α parameter, section 5.1, is highlighted in Fig. 59a-d.

Figure 58 – Three point bending test: (a) geometric properties (b) discretisation

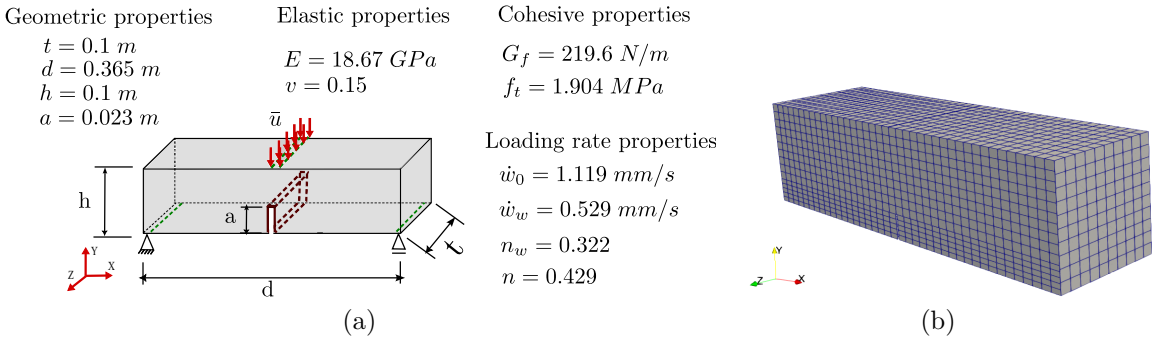

Source: The author.

The increase of this parameter results in a quasi-brittle behavior (softening) tendency of the material, while the decrease suggests a fragile behavior tendency. In addition, higher values than $\alpha = 5$ seem to not change the post-peak curve. Besides, the loading rate increase leads to the apparent growth of the material tensile strength and decreased apparent fracture energy. Thus, the threshold opening displacement reduces as the load rate increase, Fig. 59e. As expected, the physical phenomenon experimentally observed in (SANTOS; SOUSA, 2020; RUIZ *et al.*, 2010; REINHARDT; WEERHEIJM, 1991), was achieved using the 3D viscous-cohesive dipole-based BEM formulation coupled with the modified PPR cohesive model proposed in this work, section 5.1. Finally, a comparison between the experimental curves (SANTOS; SOUSA, 2020) and numerical results are also performed, Fig. 59e. In this case, the numerical curve with $\alpha = 5$ or $\alpha = 7$ provided a better fit with the experimental curves.

Fig. 60 introduces the crack path behaviour for two different load steps and considering $\dot{\delta} = 8.33 \cdot 10^{-3}$.

Figure 59 – Cohesive stress versus crack opening [a-e] and force versus crack opening [f] curves including different α parameters and loading rates $\dot{\delta}$

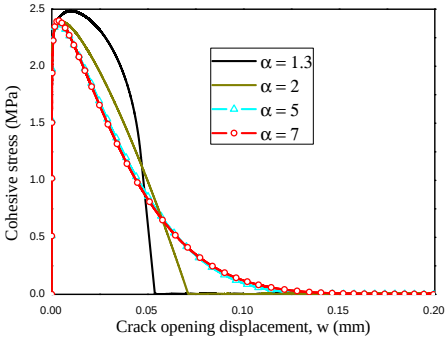

(a) $\dot{\delta} = 8.33 \cdot 10^{-2}\ mm/s$

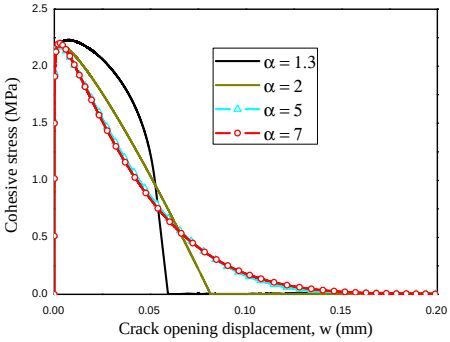

(b) $\dot{\delta} = 8.33 \cdot 10^{-3}\ mm/s$

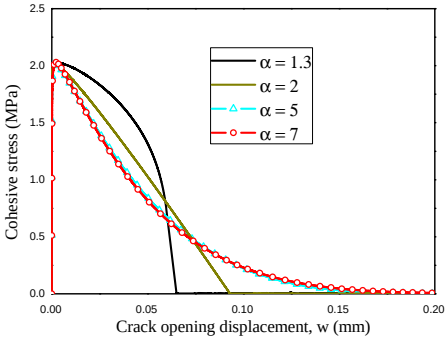

(c) $\dot{\delta} = 8.33 \cdot 10^{-4}\ mm/s$

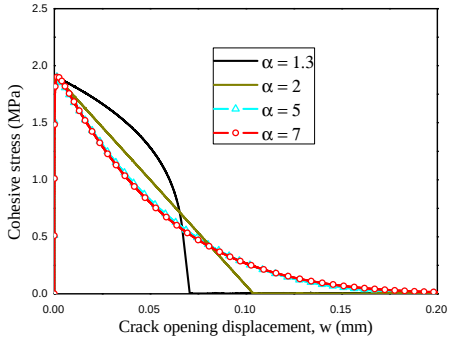

(d) Quasi-static, $\dot{\delta} = 0$ mm/s

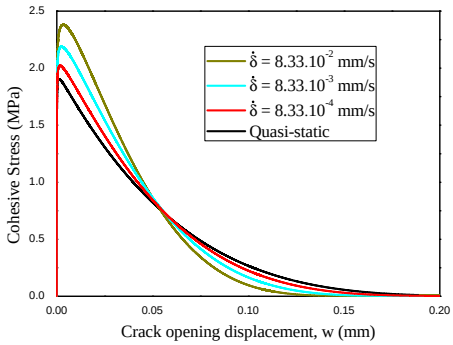

(e) $\alpha = 5$

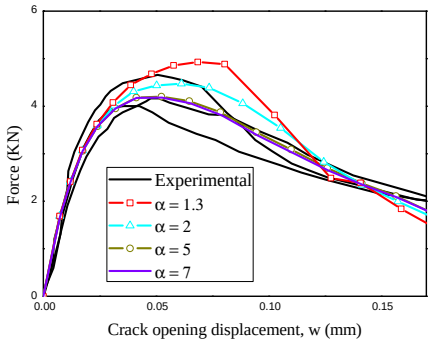

(f) $\dot{\delta} = 8.33 \cdot 10^{-3}\ mm/s$

Source: The author.

Figure 60 – Crack path (linear cohesive law – study case 1) in colour scale: 50 load steps (a); 200 load steps (b)

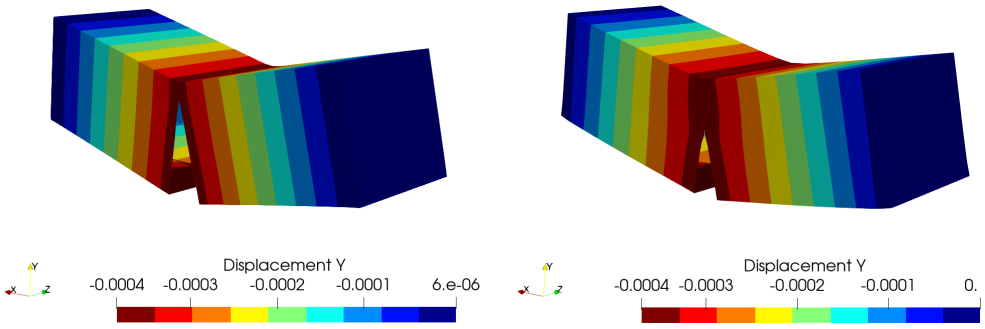

(a) (b)

Source: The author.

5.3.4.2 Ultra-high strength concrete

This section deals with an analysis of a three-point bending test specimen with ultra-high strength concrete (UHPC). The geometric properties are presented in Fig. 61 and the discretisation in Fig. 58b.

Figure 61 – Three point bending test: (a) geometric properties (b) discretisation

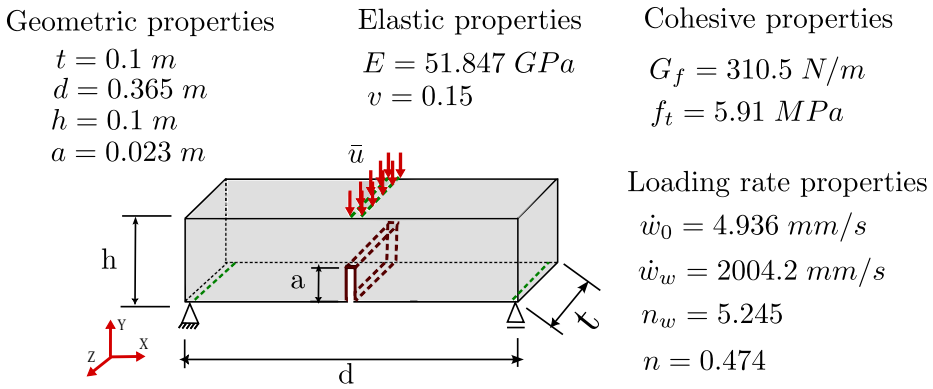

The results presented in Fig. 62a account for a force *versus* crack opening displacement result considering different α values and the loading rate as $\dot{\delta} = 8.33 \cdot 10^{-3}\ mm/s$. The nominal values introduced in Fig. 61 were used. As in the analysis with conventional concrete, it is noticeable the influence of the α parameter in the nonlinear solution, Fig. 62b. The increase of this parameter strongly modifies the post-peak curve behaviour. In addition, values higher than $\alpha = 5$ provide similar results to $\alpha = 5$ curve.

Figure 62 – Cohesive stress versus crack opening (a) and force *versus* crack opening (b) curves including different α parameters and loading rates $\dot{\delta}$

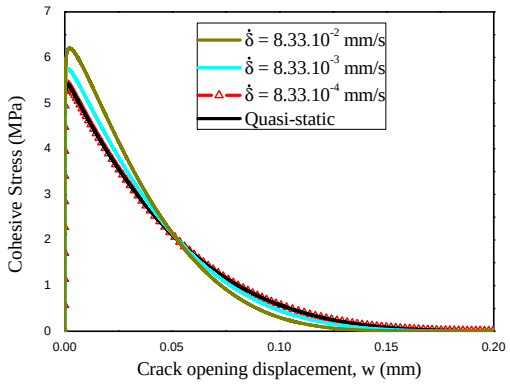

(a) $\alpha = 5$

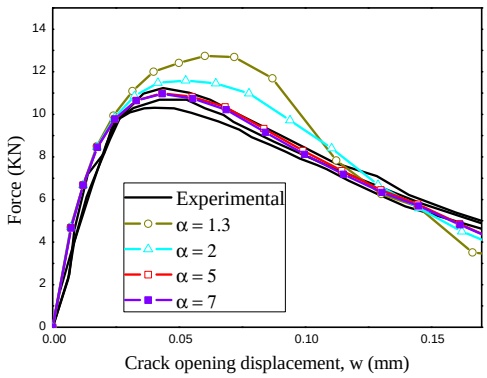

(b) $\dot{\delta} = 8.33 \cdot 10^{-3}\ mm/s$

Source: The author.

6 BAYESIAN UPDATING MODEL

In the previous chapters, the theoretical basis for obtaining the governing equations for the 3D dipole-based BEM formulation has been presented, section 3.2. Besides, the updated PPR cohesive model was coupled to this formulation, subsection 5.1.1. Thus, the analysis of cohesive crack propagation under the influence of the loading velocity rate can be adequately performed. However, a key point in this type of analysis concerns the calibration of the parameters that govern the problem. In this case, the cohesive and viscous parameters.

Uncertainty in structural mechanics is a critical topic for developing models that are essential for the design and control of complex structures. It has been extensively studied by numerous researchers. Benjamin and Cornell (1970) described the use of Bayesian updating for improved engineering decision making through examples from material testing and Geotechnical site investigation. Tang (1973) recognized the potential of Bayesian updating for updating the probabilistic description of material imperfections and flaws with inspection information. Bayesian analysis has also been used extensively for structural identification, i.e., the task of identifying dynamic properties of structural systems based on vibration measurements, e.g., rainfall and discharge measurements Kavetski, Kuczera and Franks (2006), Beven (2008). The topic has also attracted the attention of the mathematical community , Kennedy and O'Hagan (2001). Its popularity is further increasing as computational limitations are becoming less of a concern with increased computing power and enhanced algorithms.

The calibration of cohesive and viscous parameters is a huge challenge, once few statistical data information is available in the literature. To the author's knowledge, only Santos and Sousa (2020) proposed a methodology that calibrate the cohesive and viscous parameters from fracture applications. Despite being a important advance in this field of study, the deterministic predictions may compromise the accuracy of the calibration, once the knowledge about the model characteristics is not complete.

A consistent and effective framework for combining new information with existing models is provided by Bayesian analysis, in which prior probabilistic models are updated with data and observations. The Bayesian framework enables the combination of uncertain and incomplete information with models from different sources and it provides probabilistic

information on the accuracy of the updated model. The latter is of particular relevance, since system predictions typically remain uncertain even with new information. For this reason, important decisions on engineering systems should be made on the basis of reliability and risk assessments, and Bayesian analysis is essential to achieve such assessments. In general, Bayesian inference is an interesting tool for controlling and quantifying uncertainties present in structural models. Besides, uncertainty quantification in structural mechanics is an important subject for constructing models that are essential for the design and control of complex structures

6.1 Bayesian updating model

The Bayesian updating approach is a robust and suitable method to learn and to calibrate parameters of a model based on data observations. The statistical procedure of the Bayesian inference begins by considering a data set $\mathfrak{D}$, which can be experimental results and the model parameters as θ. Applying Bayes's theorem, the following posterior distribution can be achieved:

$$\rho(\theta \mid \mathfrak{D}, \mathbf{M}) = \frac{\rho(\mathfrak{D} \mid \theta, \mathbf{M})\rho(\theta \mid \mathbf{M})}{\rho(\mathfrak{D} \mid \mathbf{M})} \tag{6.1}$$

in which $\theta = [\theta_1,...,\theta_{N_p}]$ is the set of N_p model parameters. $\mathbf{M}$ is the data from the viscous-cohesive dipole-based BEM model, $\mathfrak{D}$ indicates the available experimental data.

In Eq. 6.1, $\rho(\theta \mid \mathbf{M})$ is the prior probability density function, which represents the prior knowledge about the distribution of θ. $\rho(\mathfrak{D} \mid \theta, \mathbf{M})$ is the likelihood function, which expresses the plausibility of observing data $\rho(\mathfrak{D})$ given a certain value of θ. Finally, $\rho(\mathfrak{D} \mid \mathbf{M})$ is a normalising constant called model evidence. This constant assumes an integral of the product between the likelihood and prior functions along the domain (STRAUB; PAPAIOANNOU, 2015).

6.1.1 Likelihood function

In this study, the posterior distribution, $\rho(\theta \mid \mathfrak{D}, \mathbf{M})$, is achieved by performing Monte Carlo simulations. In such case, the likelihood function $\rho(\mathfrak{D} \mid \theta, \mathbf{M})$ is necessary and built with basis on numerical and experimental curves of a three-point bending test under loading velocities rates condition. To construct this function, we follow the same strategy presented in Cordeiro, Leonel and Beaurepaire (2017), which consists of defining n reference deflections $\mathbf{d} = [d_1, d_2, ...d_n]$. The deflections are carefully placed in the reference curves. Next, the correspondent values of load $\mathbf{l} = [l_1, l_2, ..., l_n]$ are retrieved in the same deflections positions. The number of deflection points is chosen based on the number of reference curves. It is important to mention that the relation $N = n + 1$ must be defined

to enable correlation matrix construction, Eq. 6.3. Besides, N is the total number of experimental curves available, whereas n is the total number of deflection points. In this study, the likelihood function is built with basis on three experimental curves from a three-point bending test available in Santos and Sousa (2020) and two statistical curves (media +/- standard deviation of these experimental curves), with total five reference curves and four deflection points.

To introduce the likelihood function, we must consider a statistical distribution to match the experimental load data. The Gaussian distribution can be utilised (CORDEIRO; LEONEL; BEAUREPAIRE, 2017), and the covariance and mean matrix are determined as:

$$\mathbf{m} = [m_1, m_2, ..., m_n]^T; \quad \mathbf{C} = [c_{ij}]_{1 \leqslant i,j \leqslant n} \tag{6.2}$$

The covariance matrix and the vector of mean values can be expressed as:

$$m_i^N = \frac{1}{n}\sum_{k=1}^{N} l_i^k; \quad c_{ij}^N = \frac{1}{n}\sum_{k=1}^{N}(l_i^k - m_i)(l_j^k - m_j) \tag{6.3}$$

where l_j^k is the load associated to the deflection point d_i of the k^{th} experimental curve

Considering the Gaussian distribution, the probability density function can be constructed as follows:

$$\mathbf{f_N}(\mathbf{l}) = \frac{1}{(2\pi)^{1/2}|\mathbf{C_N}|^{1/2}} \exp\left(-\frac{1}{2}(\mathbf{l} - \mathbf{m_N})^T \mathbf{C_N^{-1}}(\mathbf{l} - \mathbf{m_N})\right) \tag{6.4}$$

where $\mathbf{l}$ is the vector with force values associated to reference deflection points d_i. Besides, $\mathbf{m_N}$ and $\mathbf{C_N}$ are the mean and covariance tensors. Finally, the likelihood function $\rho(\mathfrak{D} \mid \theta, \mathbf{M})$, can be constructed for a viscous-cohesive numerical model $\mathbf{M}$ as:

$$\rho(\mathfrak{D} \mid \theta, \mathbf{M}) = \mathbf{f_N}(\mathbf{l}) \tag{6.5}$$

where $\mathbf{M}$ is the viscous-cohesive dipole-based 3D model, section 6.4.

6.1.2 Bayesian Updating with Structural Reliability Methods

Evaluation of the posterior PDF involves the evaluation of highly dimensional integrals, which may represent a challenging task. The Bayesian Updating with Structural Reliability Method (BUS) approach (STRAUB; PAPAIOANNOU, 2015) can overcome this challenging task, providing an alternative procedure to generate samples of a posterior distribution.

When applying structural reliability methods, it is convenient to introduce an additional variable ξ, uniform in the interval $[0,\xi_{max}]$.

$$\xi_{max} = \max\ \rho(\mathfrak{D} \mid \theta, \mathbf{M})\rho(\theta \mid \mathbf{M}) \tag{6.6}$$

The ξ samples are generated using the Monte Carlo method, and the sample $[\theta^k, \xi^k]$, is accepted if:

$$\xi_k \leq \rho(\mathfrak{D} \mid \theta_k, \mathbf{M})\rho(\theta_k \mid \mathbf{M}) \tag{6.7}$$

Complementarily, the samples are rejected if:

$$\xi_k > \rho(\mathfrak{D} \mid \theta_k, \mathbf{M})\rho(\theta_k \mid \mathbf{M}) \tag{6.8}$$

The parameter k can be any value between 1 and the total number of samples N_m. The posterior distribution of θ is achieved at the end of the process when k is equal to the total number of samples. Fig. 63 illustrates schematically the rejection process. The boundary of the shaded area is $\rho(\mathfrak{D} \mid \theta_k, \mathbf{M})\rho(\theta_{\mathbf{k}} \mid \mathbf{M})$. Besides, the accepted and rejected samples are represented by the red and black points, respectively.

Figure 63 – Bayesian update approach considering a simple rejection algorithm

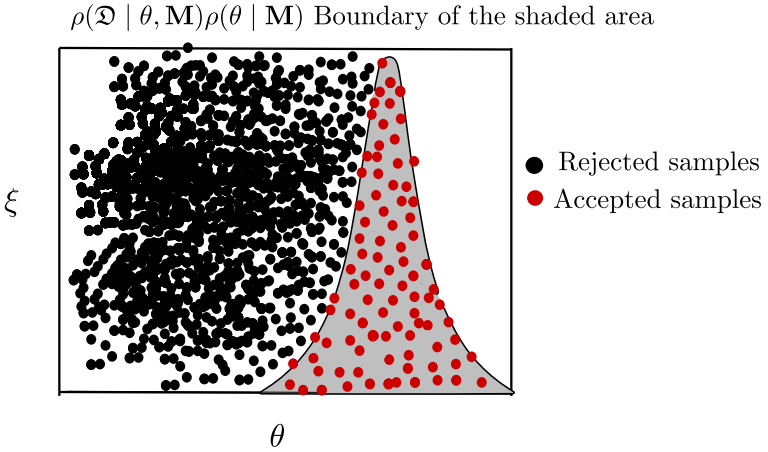

Source: The author.

In this procedure, a large number of samples is rejected during the process. This aspect increases the computational effort once each simulation requires a numerical model run for constructing the likelihood function. One important step to compute the posterior distribution is related to the definition of a failure domain, which is constructed based on rejected samples, while the safe domain is associated to accepted samples, i.e.

$$g(\theta, \xi) = \xi - \rho(\mathfrak{D} \mid \theta, \mathbf{M})\rho(\theta \mid \mathbf{M}) \tag{6.9}$$

where $g(\theta, \xi) \leqslant 0$ is the limit state function. The rejection process is similar to the one presented in Fig. 63. However, in this case, the shaded area's boundary is the limit function $g(\theta, \xi) \leqslant 0$, Eq. 6.9.

Among the available structural reliability methods, the importance sampling (IS) methods are suitable for generating (weighted) samples from the observation domain Ω_u. The classic transformation methods First Order Reliability Method (FORM) or Second Order Reliability Method (SORM) can also be applied within the BUS context. However, the use of these methods shouldn't be considered without further investigations into their accuracy. An alternative method, proposed by Au and Wang (2008), is based on subset simulations (SUS), which according to Straub and Papaioannou (2015), are particularly efficient in problems involving a large number of random variables.

The subset technique is based on replacing the calculation of a very small failure probability, at high computational cost, by a sequence or product of conditional failure probabilities. This is performed by choosing intermediate failure limits. Then, the failure probability of conditional events can be estimated with a reduced number of simulations. To estimate the probabilities of conditional events, the Monte Carlo Markov Chain (MCMC) (BECK, 2010) can be used. The mathematical definition of the technique is given below.

$$p_f = P(E) = \prod_{i=1}^{m-1} P(E_{i+1} \mid E_i) \tag{6.10}$$

where E is the set of intermediate failure domains constructed as $E_1 \supset E_2 \supset ... \supset E_m$, where E_1 is the first intermediate domain, E_m is the last intermediate domain and m the number of intermediate domains. Besides, p_f is the probability of acceptance, $P(\cdot)$ is the probability associated to an event and $P(E_{i+1} \mid E_i)$ are the conditional probabilities. Each intermediate domain is defined by:

$$E_i = g(\theta, \xi) \leq b_i \tag{6.11}$$

where $b_i = b_1,...,b_m$ is the set of intermediate probabilities, $g(\theta, \xi)$, is the limit state function, Eq. 6.9. b_i is chosen as a percentile p_0 of the samples, where $b_1 > b_2 > ... > b_m = 0$.

The main aspect of the subset technique is to estimate the probability of the event $P(E)$ from E_0 and from $P(E_{i+1} \mid E_i)$, $i = 1,..., m-1$. Intermediate events E_i are chosen adaptively using probability information from conditional events. The last intermediate event E_m will be reached when $b_m = g(\theta, \xi) = 0$, Eq. 6.9.

Initially, a Monte Carlo simulation with N_m samples is performed, which allows obtaining the vector $\theta_{0,k}$, $k = 1,...N_m$. Subsequently, the vector $\theta_{0,k}$ is applied in the limit state equation, $Y_{0,k} = g(\theta_{0,k},\xi)$, and sorted in ascendant order, enabling the determination of $Y^+_{0,k}$. The first intermediate probability b_1 is determined considering $k = p_0 N_m$ in $Y^+_{0,k}$.

Thus, $p_0 N_m$ sampling points are defined in the failure domain with intermediate probability b_1. From each of these sampling points, conditional sampling points are generated via MCMC (BECK, 2010). $(1-p_0)N_m$ conditional sampling points with distribution $P(\cdot \mid E_i)$ are defined in the first level, representing a sampling size N_m at level 1. Subsequently, the sample points are applied in the limit state equation, $Y_{(1|0),k} = g(\theta_{(1|0),k}, \xi)$. Following, the vector $Y_{(1|0),k}$ is sorted in ascendant order, which enables the determination of $Y^{+}_{(1|0),k}$. The second intermediate probability b_2 is determined considering $k = p_0 N_m$ in $Y^{+}_{(1|0),k}$. Thus, the next intermediate domain, $E_2 = \mathbf{Y} \leqslant b_2$, can be defined. It's simple to notice that the $p_0 N_m$ sampling points are the seeds from the next conditional samplings. Thus, repeating the process, conditional samples can be generated until the final limit b_m reaches the value $b_m = 0$ (AU, 2005). This process is illustrated in Fig. 64 and can also be found in (AU, 2005):

Figure 64 – Subset procedure and the intermediate events

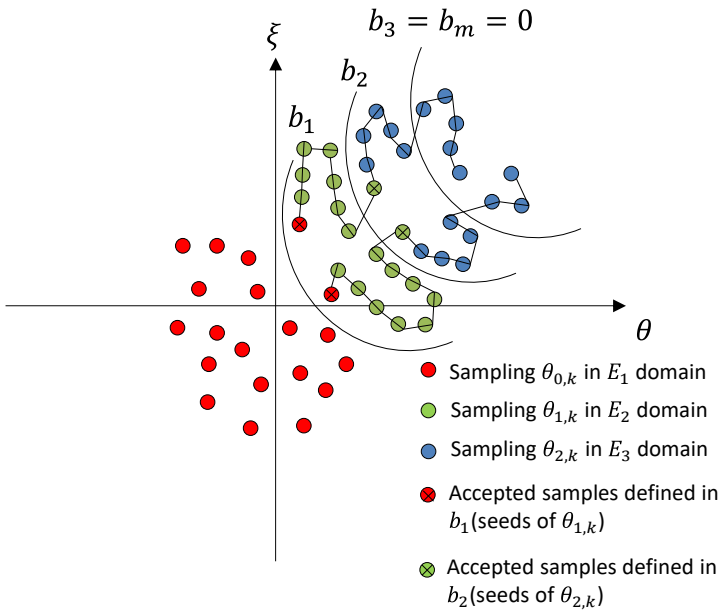

Source: The author.

6.1.3 Model class selection

The Bayesian updating scheme also enables the choice of the best/optimal model considering a number of specified models (PERALTA; RUIZ; TAFLANIDIS, 2020). For this purpose, a set of classes can be defined and the most plausible class can be chosen. First, the Bayes theorem is rewritten as:

$$\rho(\mathbf{M}_k \mid \mathfrak{D}, \mathbf{M}) = \frac{\rho(\mathfrak{D} \mid \mathbf{M}_k)\rho(\mathbf{M}_k \mid \mathbf{M})}{\rho(\mathfrak{D} \mid \mathbf{M}_k)} \tag{6.12}$$

where $\mathbf{M} = [M_1,...,M_{N_C}]$ is the set of classes. N_C is the number of classes/models, k varies from 1 until the total number of samples N_m and $\rho(\mathbf{M}_k \mid \mathbf{M}) = 1/N_C$. The term $\rho(\mathfrak{D} \mid \mathbf{M}_k)$ is a normalising constant. Besides, $\rho(\theta \mid \mathfrak{D}, \mathbf{M}_k)$ is the posterior distribution.

$$\rho(\theta \mid \mathfrak{D}, \mathbf{M}_k) = \frac{\rho(\mathfrak{D} \mid \theta, \mathbf{M}_k)\rho(\theta \mid \mathbf{M}_k)}{\rho(\mathfrak{D} \mid \mathbf{M}_k)} \tag{6.13}$$

Next, the BUS procedure can be applied and the best model can be chosen. The optimal model is defined based on the highest evidence value. Finally, the evidence,$\rho(\mathfrak{D} \mid \mathbf{M})$, can be expressed as:

$$\rho(\mathfrak{D} \mid \mathbf{M}) = \xi_{max} p_f \tag{6.14}$$

The model with the highest $p(\mathfrak{D},M)$ value is selected as the optimal model.

6.2 Artificial neural networks - surrogate model

Artificial neural networks (ANN) enable a simplified and effective representation of complex high-fidelity models with reduced computational effort. The ANN are computational techniques with a mathematical model inspired by the neural structure of intelligent organisms, where the learning process occurs through experience. As a biological neuron, an artificial neuron includes components that can capture and transmit impulses (information), as well as a component that processes the received information (HAYKIN, 2009). These two regions are shown in Fig. 65, highlighted in blue and red, respectively.

Figure 65 – Artificial neuron

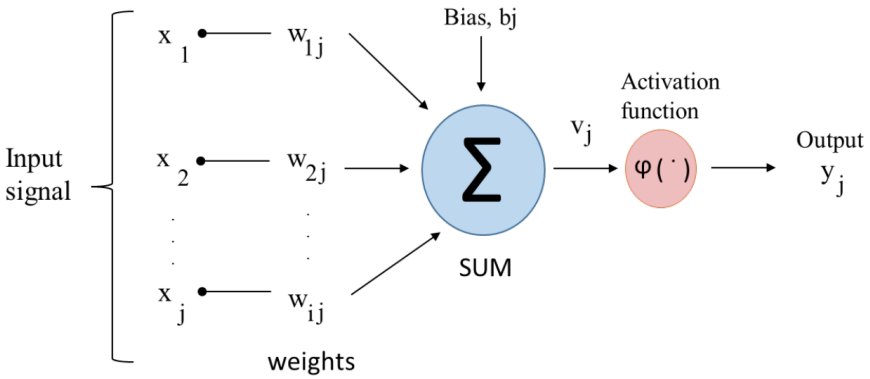

Source: Haykin (2009)

To perform the BUS procedure and to obtain force versus displacement curves, simulations from the dipole-based BEM formulation are required. It is worth mentioning

that each simulation, in the three point bending test Fig. 67, from the numerical model requires 30.4 minutes, approximately, whereas each surrogate simulation requires less than a second. Despite its accuracy, the computational cost associated to the dipole-based BEM predictions makes impeditive its full use into the Bayes analyses. Thus, the ANN has been utilised as a surrogate model in the framework proposed herein in order to keep the dipole-based BEM formulation accuracy and to enable a computational efficient approach. The Statistics and Machine Learning Toolbox from Matlab is used here to train a neural artificial network and perform the Monte Carlo simulations from BUS procedure, subsection 6.1.2.

A network with N_l layers is considered herein. The input layer of the network ($l = 1$) only transports the input information of each neuron to the next layer, it does not have any activation function. The last layer $l = N_l$ is called output layer. The remaining layers are called intermediate layers. The input neurons are constructed based on the coordinates of each sample. Thus, the expressions for the general case of intermediate layers and output $i = 2,...,N_l$ are:

$$f_i = K\left(b_i + \sum_{j=1}^{N_l} w_{ij} q_j\right) = K(a) \tag{6.15}$$

where K is the activation function, $\mathbf{q} = (q_1,...,q_{N_l})$ refers to the neuron input, w_{ij} are the input layer weights, and b_i neuron bias value. Activation functions are responsible for determining the amplitude of the output value and can be of various types, depending on the problem to which the network will be applied (HAYKIN, 2009)

The last ANN layer is defined with basis on output neurons, which are characterised by the activation function $K(a) = a$, while the hidden layers of neurons are characterised by the function:

$$K(a) = \frac{1}{1 + e^{-a}} \tag{6.16}$$

The input layer of an ANN consists of a specific number of numerical curves (force versus crack opening displacement) obtained from the 3D viscous-cohesive dipole-based BEM model, whereas the output is the surrogate model. The output of the ANN model will be further utilised to start the BUS procedure, avoiding the need to recall the numerical model a higher number of times. Three hidden layers are used with 50, 15 and 5 neurons per layer. Finally, the training process is based on the Backpropagation algorithm. In the first phase of the algorithm, the functional signal is propagated forward through the network from the input layer to the output layer, while the weights and biases remain unchanged. This forward pass is used to generate predictions based on the input data. The predicted outputs are then compared with the actual target values, producing an

error signal. In the second phase, this error signal is propagated backward through the network, layer by layer, from the output back to the input. During this backward pass, the weights and biases are iteratively updated using an optimization algorithm, with the objective of minimizing the Mean Absolute Percentage Error (MAPE). For a more detailed explanation of the Backpropagation algorithm, see Haykin (2009).

6.3 Flowchart of the BUS procedure

The flowchart of the BUS procedure is presented in Fig. 66. First, the 3D PPR viscous-cohesive dipole-based BEM formulation, is employed to achieve the predefined number of force versus displacement curves. Then, the ANN algorithm, section 6.2, is subsequently employed to calibrate a surrogate model. Next, the Bayesian updating procedure, subsection 6.1.2, is started by using the prior distributions of the parameters, which involves the subset algorithm, subsection 6.1.2. Thus, the prior distribution is updated in each intermediate domain until achieving convergence ($b_i \leqslant 0$). In each intermediate domain E_i with intermediate state function b_i, new conditional samples are generated using the MCMC algorithm (AU, 2005).

Figure 66 – Flowchart of the BUS procedure

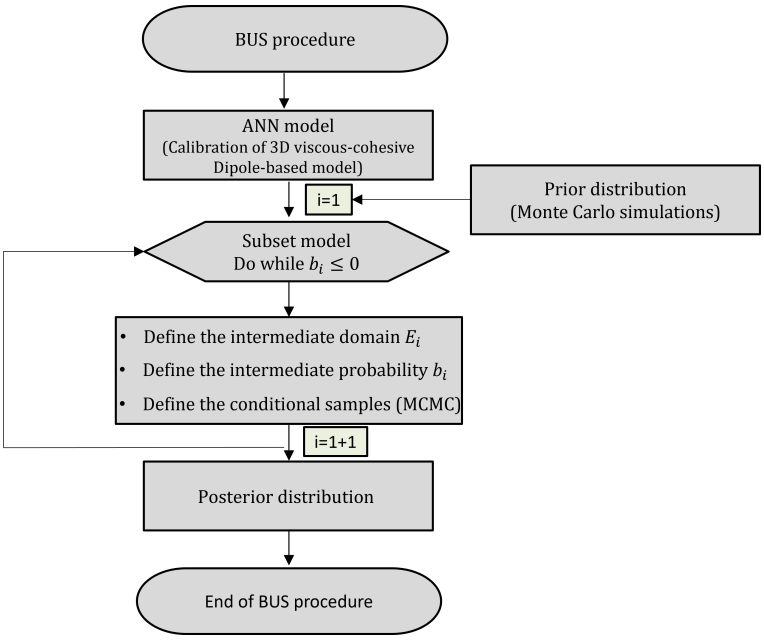

Source: The author.

6.4 Applications

Santos and Sousa (2020) analised experimentally two groups of concrete in three-point bending test including loading velocity rates. The first group is the conventional concrete, with compressive strength of $f_c = 30\ MPa$, and velocity of load application of $8.33 \cdot 10^{-3} mm/s$. The second group is an ultra-high performance concrete (UHPC), with strength of $f_c = 120\ MPa$, and $8.33 \cdot 10^{-3} mm/s$ as the loading velocity rate. For both types of concrete, the beam has $d = 400$ mm in length, depth $h = 100$ mm, thickness $t = 100$ mm and notch depth $a = 23$ mm, Fig. 67a. Three experimental load-deflection curves are available for each case, (SANTOS; SOUSA, 2020). The reference deflections of the two types of concrete were $d = [0.025, 0.05, 0.015, 0.02]\ mm$.

The system of nonlinear equations accounts for a convergence tolerance equal to 10^{-3} based on the norm of unbalanced stress values. 200 load steps apply the loading. The geometric properties and discretisation utilised are presented in Fig. 67. As illustrated in Fig. 67b, 2900 quadrilateral linear elements and 3441 collocation points compose the boundary mesh. Besides, the parameter P refers to the load applied. The dipole-based formulation requires 30.4 minutes of CPU time for the entire nonlinear analysis (one simulation) with the PPR cohesive zone model. Next, The ANN calibration and BUS inference analysis require 8.1 s and 13.3 s, respectively. The numerical curves are achieved by using the 3D PPR dipole-based BEM approach.

Figure 67 – Three point bending notched test: (a) geometric properties (b) discretisation

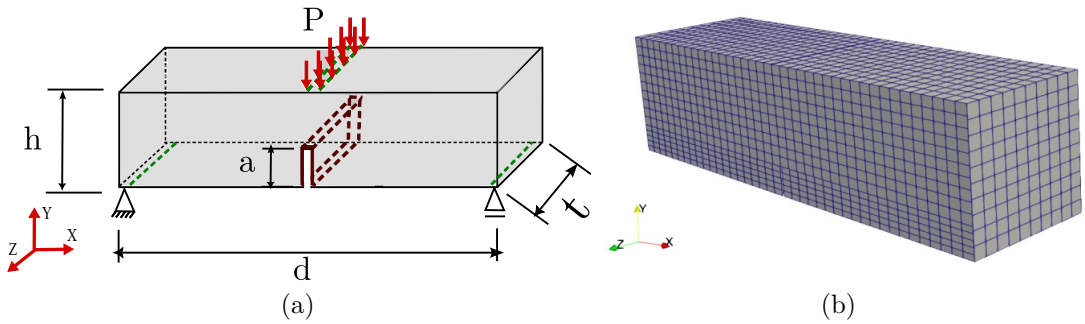

Source: The author.

6.4.1 Study case 1: Conventional concrete

6.4.1.1 Inference analysis: Conventional concrete

The inference analysis of three-point bending test (conventional concrete) is presented next. Tab. 2 lists all viscous-cohesive models analysed, and Tab. 1 the bounds of the prior distribution from all updated parameters considered. All prior distributions,

$\rho(\theta \mid \mathbf{M_k})$, are assumed as uniformly distributed and the nominal data refer to deterministic values provided by Santos and Sousa (2020). Besides, the bounds of each distribution are constructed using available information from (SANTOS; SOUSA, 2020). The Bayesian inference model class selection scheme, subsection 6.1.3 is next introduced to select the model that best fits the experimental and numerical results. A total number of 7 different parameters are updated, 11 models are considered and reviewed in Tab. 2. The updated parameters for each model used in the BUS analysis are also presented in Tab. 2. The parameters are classified as follows: (VC) viscous-cohesive: f_t, G_f, (E) elastic: E, (P) PPR model: α, Eq. 5.21, and (V) viscous: $\dot{w}_w$, $\dot{w}_0$, n_0 and n_w, Eq. 4.2 and Eq. 4.4. The number of parameters in each category, as well as the total number of parameters for each model, are specified in Tab. 2. For instance, the first model is the simplest, which only has 2 parameters (cohesive parameters). In the second model, the α parameter, which is provided by the PPR cohesive law, is added. In the third model, the Young modulus (elastic parameter) is added. The following models introduce the viscous parameters in the analysis. In all models, the viscous-cohesive parameters, G_f and f_t are included. In addition, the number of simulations used to calibrate the ANN for each model is also presented in Tab. 2.

Table 1 – Bounds of the prior distributions from study case 1

Random variable	Nominal values	Lower bound	Upper bound	Unit
E	18.67	11.196	26.124	GPa
f_t	1.904	1.142	2.665	MPa
G_f	219.6	131.760	307.440	J/m^2
α	3.15	1.3	5	mm/s
n_w	0.322	0.193	0.451	-
$\dot{w}_w$	0.529	0.3174	0.741	mm/s
n_0	0.429	0.257	0.600	-
$\dot{w}_0$	1.119	0.671	1.566	mm/s

Source: The author.

The evidence is presented in Fig. 68a. According to the results, it is noticeable that the model 2 best fits the experimental and numerical responses. The total number of adjustable parameters in model 2 is three (α, f_t, G_f). It is important mentioning that the inclusion neither of Young's modulus nor the viscous parameters appears to provide a better fit. The introduction of new random parameters may require additional experimental data information, which can lead to a more complex procedure to determine the posterior distribution. Moreover, the second simplest model (G_f, f_t and α) provides the higher evidence, with only three parameters (viscous-cohesive and α parameters). Therefore, all subsequent analyses will be carried out using model 2.

Table 2 – Model classes considered in the Bayesian updating.

Model	Updated parameters	VC	P	E	V	Total parameters	N. of simulations
1	G_f, f_t	2	0	0	0	2	100
2	G_f, f_t, α	2	1	0	0	3	200
3	G_f, f_t, α, E	2	1	1	0	4	300
4	G_f, f_t, α, n_w	2	1	0	1	4	300
5	G_f, f_t, α, $\dot{w}_w$	2	1	0	1	4	300
6	G_f, f_t, α, n_0	2	1	0	1	4	300
7	G_f, f_t, α, $\dot{w}_0$	2	1	0	1	4	300
8	G_f, f_t, α, $\dot{w}_w$, n_w	2	1	0	2	5	400
9	G_f, f_t, α, $\dot{w}_0$, $\dot{n}_0$	2	1	0	2	5	400
10	G_f, f_t, α, $\dot{w}_w$, $\dot{n}_w$, n_0	2	1	0	3	6	500
11	G_f, f_t, α, $\dot{w}_w$, n_w, n_0, $\dot{w}_0$	2	1	0	4	7	600

Source: The author.

The correlation coefficient (BECK; TAFLANIDIS, 2013) considering the adjustable variables is also presented in Fig. 68b. A strong correlation between the f_t and G_f is observed, as expected since these parameters are related through the cohesive law adopted. Moreover, the α parameters also presents correlation with f_t and a strong correlation with G_f.

Next, we briefly discuss the accuracy of the surrogate model. As shown in Fig. 69. A small portion of the samples was set aside from the training data to be later used as validation data, which resulted in the validation graph presented in Fig. 69. The output of this calibration is the force (KN) values measured in random deflection points. According to this figure, the ANN model leads to the equivalent responses in comparison to the 3D viscous-cohesive dipole BEM approach. This results proves the accuracy of ANN in describing the mechanical phenomena. It is worth mentioning that similar results to Fig. 69 were achieved considering the other 10 models. However, only the calibration output for model 2 (best model) was presented, to avoid repetitive matter.

Fig. 70a-c presents the posterior distributions of parameters $[\alpha, f_t, G_f]$. The posterior distribution is represented by the black points, whereas the prior distribution are the grey points. The apparent fracture energy, G_f, refers to the normal energy predicted in the PPR model. G_f and the apparent tensile strength, f_t, are strongly correlated, while the α parameter has medium and strong correlation between f_t and G_f, respectively. In addition, the number of samples for the posterior distribution to the updated parameters, Fig. 70d-f, and their respective histograms, are illustrated in Fig. 70g-i. According to these results, the apparent fracture energy presents the greatest importance in the analysis, which is represented by the narrow area from the posterior distribution, in both the

Figure 68 – (a) Evidence evaluation for model class selection (b) correlation among the variables from the best model (model 2)

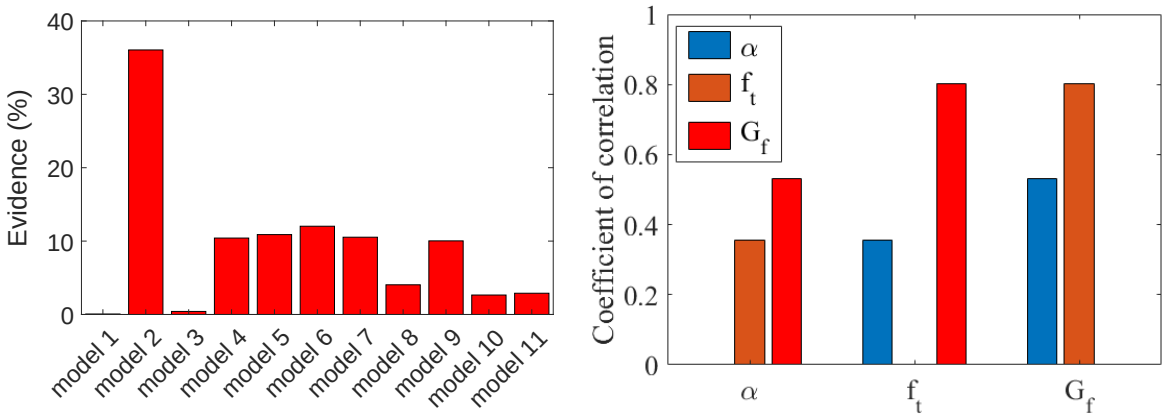

Source: The author.

Figure 69 – Quality of the fit (force - KN) between the surrogate and numerical results considering model class 2

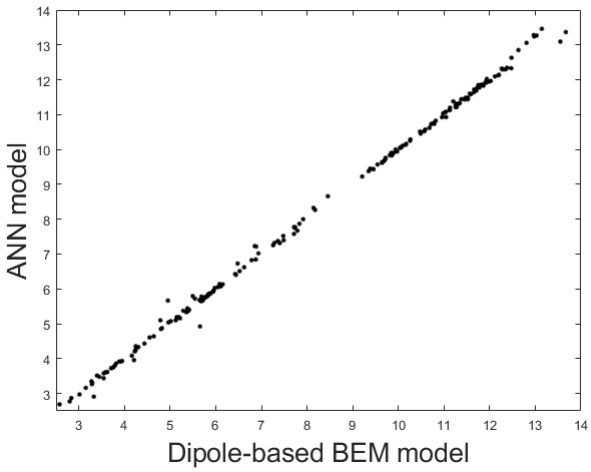

Source: The author.

number of samples and histogram results. It is also important to mention that the α parameter presented values in the interval of $\alpha = 2...5$, which is a reasonable interval for quasi-brittle materials (PARK; PAULINO, 2012). The red curve Fig. 70g-i, represents the maximum a posteriori (MAP), which corresponds to the peak (maximum) of the posterior probability density function (PDF). Finally, the PDF for the three updated parameters is also presented in Fig. 70j-i.

Finally, the posterior samples and statistical values of load versus deflection curves are presented. These curves are illustrated in Fig. 71a. It is noticeable that after the BUS updated procedure, the samples tend to assume a position closest to the experimental curves and assume a good fit in the vicinity of the reference deflection points. Besides, the

mean and standard deviation values from both prior and posterior distribution are also presented in Fig. 71b.

Figure 71 – (a) Force versus displacement curves considering prior and posterior distribution (b) and statistical values considering model 2

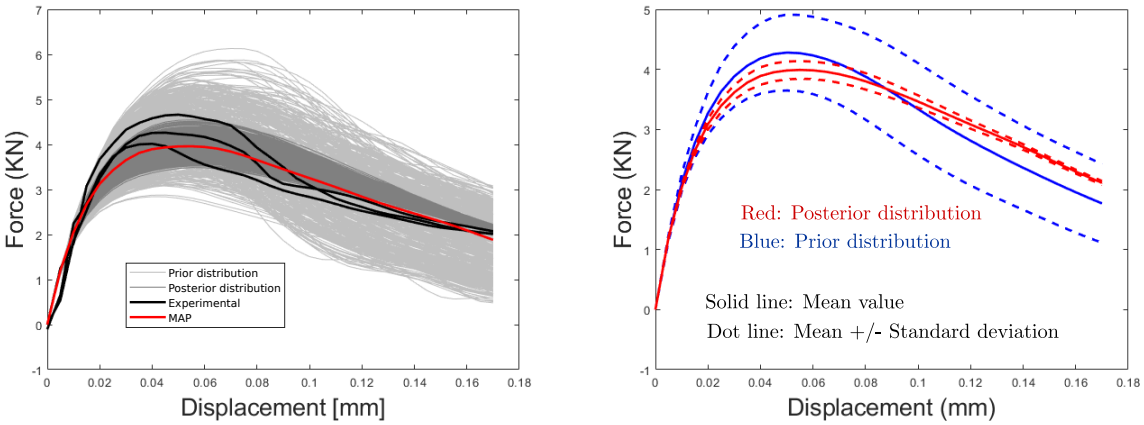

Source: The author.

Tab. 3 provides the statistical values (mean, standard deviation (s.d.), and coefficient of variation (c.v.)) from posterior distributions. The MAP values, (Fig. 70j-i), are also presented. It's worth mentioning the lowest c.v. of the apparent fracture energy. This is expected, since the choice of different G_f values from the posterior interval, Fig. 70e, can lead to inaccurate results (distant from experimental curves). This reflects the importance of G_f parameter in the analysis.

Table 3 – Statistic values from the prior and posterior distribution considering model class 2

Parameter	Posteriori mean	Prior mean	Posteriori s.d.	Posterior C.v.	MAP	Unit
α	4.1863	3.15	0.57	0.137	4.601	-
f_t	1.6962	1.904	0.11	0.0676	1.686	MPa
G_t	239.7045	219.6	3.79	0.015	239.701	J/m^2

Source: The author.

Figure 70 – Prior and posterior distributions of the parameters of model 2

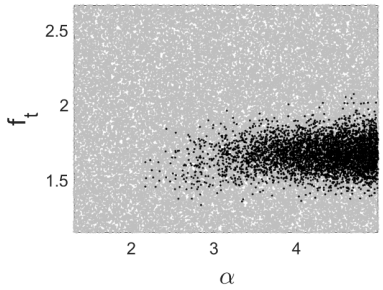

(a) Apparent tensile strength, f_t, versus α

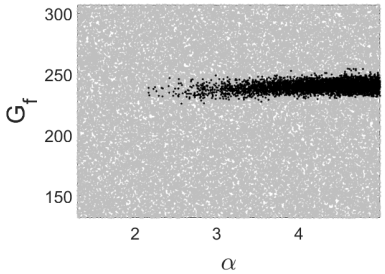

(b) Apparent fracture energy, G_f, versus α

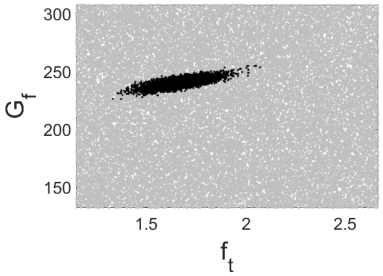

(c) Apparent tensile strength, f_t, versus apparent fracture energy, G_f

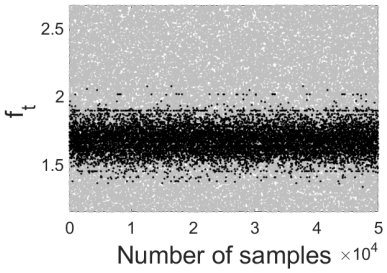

(d) Apparent tensile strength, f_t, versus number of samples

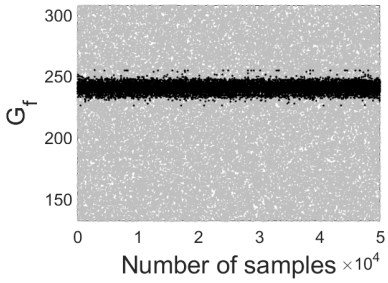

(e) Apparent fracture energy, G_f, versus number of samples

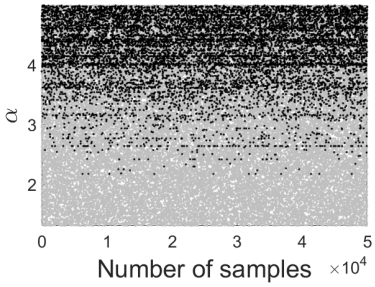

(f) α versus number of samples

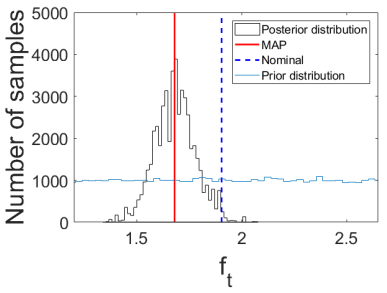

(g) Apparent tensile strength, f_t, histogram

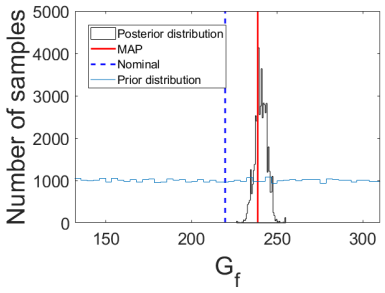

(h) Apparent fracture energy, G_f, histogram

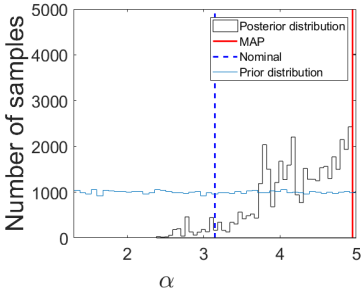

(i) α histogram

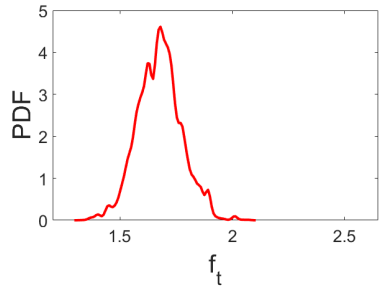

(j) Apparent tensile strength, f_t, PDF

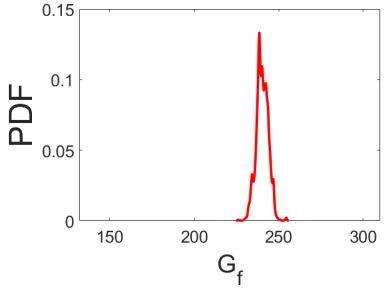

(k) Apparent fracture energy, G_f, PDF

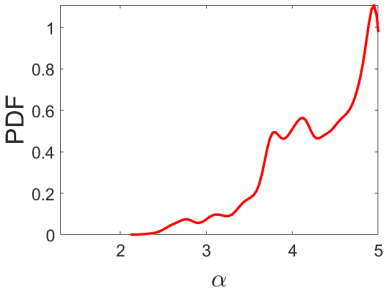

(l) α PDF

Source: The author.

6.4.2 Study case 2: Ultra-high performance concrete (UHPC)

This section deals with a case study regarding UHPC in an inference analysis. It is important to mention that UHPC has a more organised microstructure (more compact) than conventional concrete, with fewer internal flaws, lower experimental variability and longer quasi-brittle behaviour. Besides, the apparent tensile strength of this type of concrete is much higher compared to conventional concrete, causing crack initiation delay. Such differences between the two concrete types justify the analysis developed herein.

6.4.2.1 Inference analysis: Ultra-high performance concrete (UHPC)

An inference analysis of a three-point bending test for UHPC is presented in the following. The updated parameters with their lower bounds and upper bounds are provided in Tab. 4. The nominal values can be found in Santos and Sousa (2020).

Table 4 – Bounds of the prior distributions

Random variable	Nominal values	Lower bound	Upper bound	Unit
E	51.847	41.108	72.955	MPa
f_t	6.09	4.73	7.09	MPa
G_t	339.0	248.94	372.0	J/m^2
α	3.15	1.3	5	mm/s
n_w	5.245	3.14	7.34	-
$\dot{w}_w$	2004.2	1202.5	2.805	mm/s
n_0	0.474	0.284	0.663	-
$\dot{w}_0$	4.936	2.961	6.910	mm/s

Source: The author.

The bar evidence is presented in Fig. 72a. As in conventional concrete, model 2 provided the best evidence. Thus, all the subsequent analyses will be carried out by this model, Tab. 2. The coefficient of correlation (BECK; TAFLANIDIS, 2013) considering the adjustable parameters α, f_t and G_f, is presented in Fig. 72b. As in conventional concrete, a strong correlation between the f_t and G_f is noticed.

The first curve in Fig. 73 provides the accuracy of the ANN-based surrogate model. In total, 200 simulations have been used to calibrate the surrogate model, Tab. 2. According to this result, the trained model provided similar results in forces (KN) when compared to the 3D viscous-cohesive dipole-based BEM model.

The posterior distributions of the parameters, $\theta = [\alpha, f_t, G_f]$, are introduced in Fig. 74a-f regarding the UHPC. The posterior distribution is represented by the black curves, whereas the prior distribution are the grey curves. The apparent fracture energy, G_f, refers to the normal energy predicted in the PPR model. The results presented in Fig. 74a-f show the strong dependency of the viscous-cohesive and α parameters in the

Figure 72 – (a) Evidence evaluation for model class selection (b) correlation among the variables from the best model (model 2), UHPC

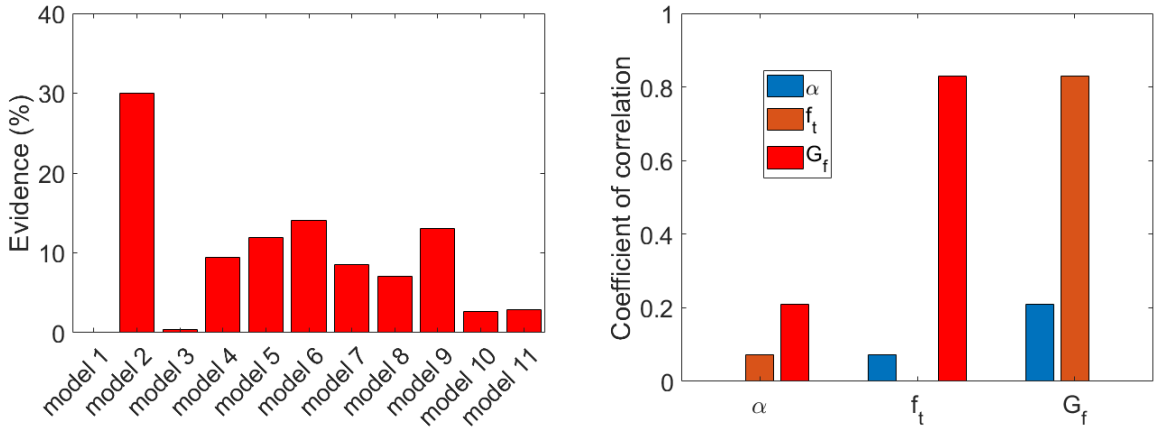

Source: The author.

Figure 73 – Fit between the surrogate model and numerical results, model 2, UHPC

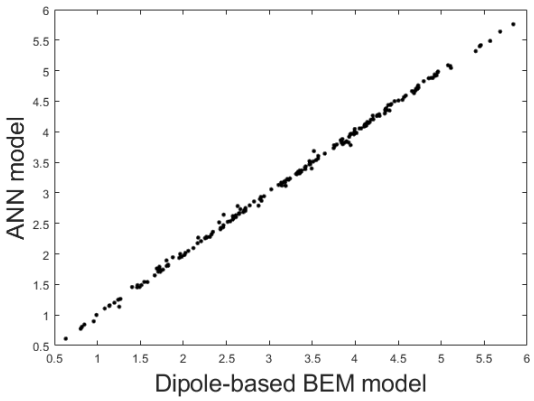

Source: The author.

crack propagation process. Besides, as in Fig. 70, the apparent fracture energy and the apparent tensile strength parameter, presented a strong correlation. In addition, their respective histograms, Fig. 74g-i and PDF, Fig. 74j-l, are also provided.

Finally, in contrast to the conventional concrete, the interval of possible values from α parameter strongly modify, with values only between $\alpha = [4 - 5]$. The prolonged quasi-brittle behaviour of UHPC is reflected in the interval of possible values from the α parameter, which was close to 5 (values closer to 5 reflect prolonged quasi-brittle/ductile behaviour, (PARK; PAULINO, 2012)).

Tab. 5 provides the statistic values (mean, standard deviation (s.d.), and coefficient of variation (c.v.)) from posterior distributions. The MAP values are also presented. Again, the apparent fracture energy provided the lowest s.d. Besides, all updated parameters presented lower s.d. when compared to the conventional concrete, Tab. 5. Such behaviour

Figure 74 – Prior and posterior distributions of the parameters for the UHPC to the model class 2

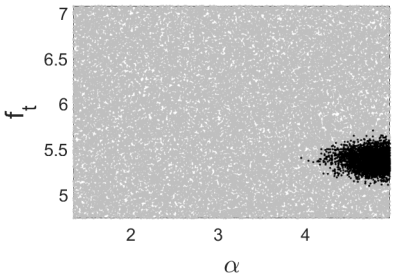

(a) Apparent tensile strength versus, f_t, α

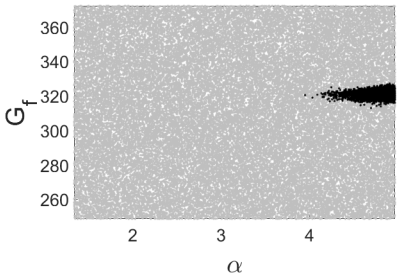

(b) Apparent fracture energy, G_f, versus α

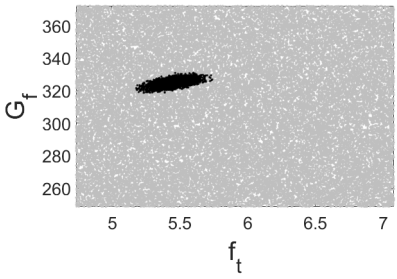

(c) Apparent tensile strength, f_t, versus apparent fracture energy, G_f

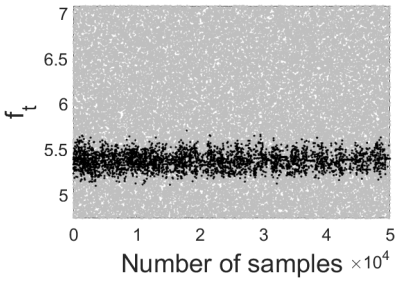

(d) Apparent tensile strength, f_t, versus number of samples

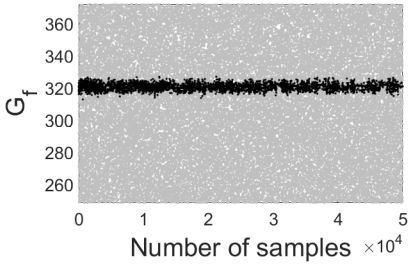

(e) Apparent fracture energy, G_f, versus number of samples

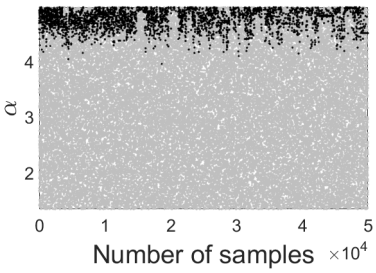

(f) α versus number of samples

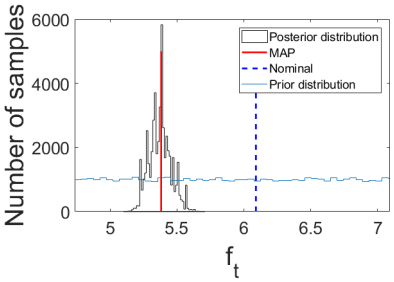

(g) Apparent tensile strength, f_t, histogram

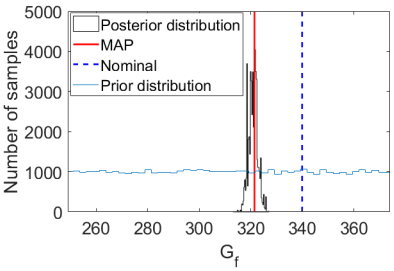

(h) Apparent fracture energy, G_f, histogram

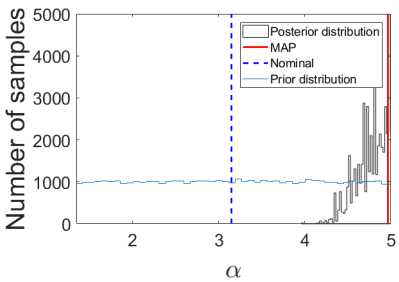

(i) α histogram

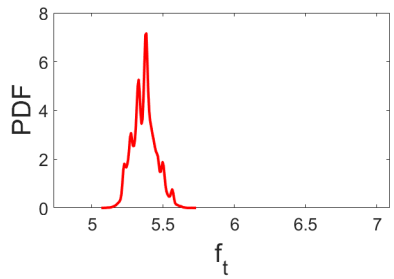

(j) Apparent tensile strength, f_t, PDF

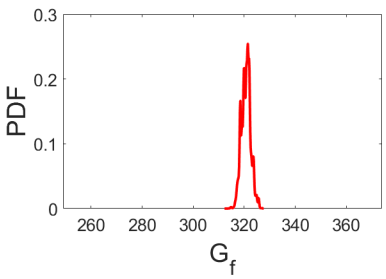

(k) Apparent fracture energy, G_f, PDF

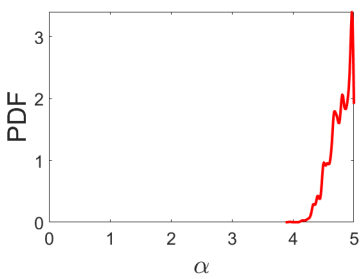

(l) α PDF

Source: The author.

is expected, since the experimental curves from the UHPC have lower variability.

Table 5 – Statistic values from posterior distributions for model class 2, UHPC

Parameter	Posteriori mean	Prior mean	Posteriori s.d.	Posterior C.V.	MAP	Unit
α	4.617	3.15	0.211	0.0458	4.949	-
f_t	5.472	5.91	0.076	0.0140	5.421	MPa
G_t	321.8	310.4	1.634	0.0051	322.9	J/m^2

Source: The author.

Finally, the posterior samples and statistical values of load versus deflection curves are provided as well as the MAP curve. These curves are presented in Fig. 75. As in Fig. 71, the samples tend to approximate the experimental curves and present a good fit in the vicinity of the reference deflection points. Finally, the MAP curve provides the best fit between the numerical and experimental curves.

Figure 75 – (a) Force versus displacement curves considering prior and posterior distribution (b) statistical values for model 2, UHPC

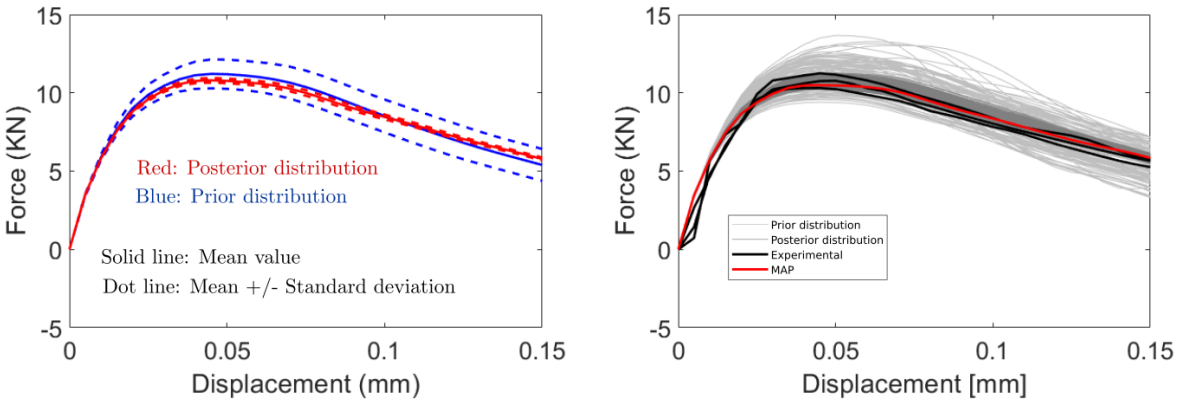

(a) (b)

Source: The author.

7 CONCLUDING REMARKS

In this thesis, an alternative dipole-based BEM formulation have been developed for the analysis of viscous-cohesive crack problems in three-dimensional domains. Besides, a new framework to quantify viscous-cohesive material parameters considering loading rate-dependent applications is proposed. Its originality is on the spot when viscous-cohesive BEM and BUS procedures are coupled. In this context, the 3D dipole-based formulation is coupled to the BUS approach, allowing an effective procedure capable of handling the inherent randomness of the viscous-cohesive process. In addition, the loading velocity rate effects are adequately represented by a time-dependent function, which updates the cohesive model. The PPR cohesive zone model proposed by Park, Paulino and Roesler (2009) is coupled to the 3D dipole-based BEM formulation enabling the nonlinear fracture modelling. Further, a modification in the PPR polynomial potential method is proposed, enabling the modelling of the quasi-brittle fracture responses and time-dependent effects. Finally, the stochastic inverse procedure provides the most representative viscous-cohesive parameter values that minimise the error between experimental and numerical solutions.

In chapter 3, the dipole-based BEM approach for cohesive crack propagation modelling in three-dimensional components have been presented. The proposed formulation utilises an initial stress field for representing the mechanical behaviour along the fracture process zone, which leads to a set of self-equilibrated forces named as dipole. The proposed approach requires three algebraic equations per source point positioned along the FPZ mesh. Besides, the formulation does not need predefined information about the crack growth path, that is, the formulation can model the nonlinear fracture process in mixed-mode problems positioned in asymmetric geometry and boundary conditions. Additionally, the formulation can be straightforwardly coupled to in-house codes based on the classical BEM. It is sufficient to incorporate the dipoles integral terms into the displacement integral equation. Five applications demonstrated the robustness of the proposed dipole-based formulation. It has been effective in all cases, in which experimental and numerical responses available in the literature have been utilised as references, see section 3.9. Besides, the results achieved are in concordance with reference results for pure and mixed fracture modes. Finally, The last application, section 3.9, demonstrates the performance of the proposed formulation in the mechanical modelling of geometrically complex specimen subjected to

fully mixed-mode fracture,that is, I-II-III. This application provides benchmark responses for further developments in nonlinear computational fracture mechanics, once experimental results in similar conditions are not available in the literature. The novelties presented herein have been published in Almeida and Leonel (2024a)

In chapter 4, a new methodology that couples the 3D dipole-based BEM formulation to the viscous-cohesive approach presented in (SANTOS; SOUSA, 2020) have been proposed. Thus, the developments herein lead to an approach capable of modelling the fracture of three-dimensional structures composed of quasi-brittle materials by a nonlinear viscous-cohesive description. The influence of the loading velocity rates has been incorporated into the classical cohesive fracture model by modifying accordingly the tensile material strength and the fracture energy. The proposed viscous-cohesive formulation has been tested in three applications, section 4.3, in which analytical and experimental results are references. As expected, the increase of the loading velocity rate leads to the growth of apparent material tensile strength and to the decrease of the apparent fracture energy. As a result, the threshold opening displacement reduces as the load velocity rate increase, Fig. 36. Thus, the physical phenomenon experimentally observed in (SANTOS; SOUSA, 2020; RUIZ *et al.*, 2010; REINHARDT; WEERHEIJM, 1991), have been achieved using the 3D viscous-cohesive dipole-based BEM formulation. The comparative results demonstrate the good performance of the proposed couple formulation and the good agreement provided by it in comparison with the references. The mechanical behaviour analysed by the curves forces x displacements and the crack propagation path are in agreement with the references. The original ideas discussed herein have been published in Almeida and Leonel (2024b)

In chapter 5, The PPR cohesive zone model proposed by Park, Paulino and Roesler (2009) have been coupled to the 3D dipole-based BEM formulation enabling the nonlinear fracture modelling of quasi-brittle materials. enabling the representation of a wide variety of materials. The intrinsic PPR CZM, Cordeiro, Daumas and Monteiro (2024), is used in this work, enabling the adjust of pre-peak curve inclination by introducing initial slope parameters. Further, a modification in the PPR polynomial potential method is developed, enabling the modelling of the quasi-brittle fracture responses and time-dependent effects. In total, 4 four applications have been proposed to demonstrate the robustness of the new couple formulation, section 6.4. The last application analyzes the couple PPR dipole-based BEM formulation considering different loading velocity rate values. The curves forces x displacements are in agreement with the reference curves presented in Santos and Sousa (2020), considering conventional and ultra-high strength concrete. The influence of the α parameter, section 5.1, have been highlighted in Fig. 59a-d. The increase of this parameter results in quasi-brittle behaviour (softening) tendency of the material, while the decrease suggests brittle behaviour tendency. In addition, higher values than $\alpha = 5$ do not change

substantially the post-peak curve. Besides, the increase of the loading velocity rate leads to the growth of apparent material tensile strength and to the decrease of the apparent fracture energy.

In chapter 6, a stochastic inverse approach for viscous-cohesive modelling was developed based on coupling the 3D dipole-based formulation to the BUS procedure. The PPR cohesive zone model have been used, which adequately represents the energy dissipation phenomena at FPZ. Besides, the quantification of the shape parameter α, section 5.1, was also investigated. In addition, the model class selection was used to enable the identification of the most plausible model according to the evidence values and experimental data information. The PPR CZM has been weighted and modified by a viscous function, which accounts for the velocity of load application. It is worth stressing that such function requires the assessment of crack opening displacement velocities, which is accurately handled by the BEM. Later, this formulation was coupled to the BUS procedure in order to quantify viscous-cohesive parameters. Two different types of concrete, conventional and UHPC, demonstrate the relevance of this coupled formulation. A total number of seven different parameters of uncertain characteristics have been updated, and eleven models considered. The second model class was the most plausible case for both types of concrete, which highlights the importance of the viscous-cohesive, f_t, G_f, and α (PPR model), section 5.1, parameters in the analysis. According to the results, the fracture energy presents the greatest importance in the analysis, which is represented by the narrow area from the posterior distribution, Fig. 74e and Fig. 70e. Any change in this range of possible values would provide unsatisfactory results. Besides, the posterior distributions of the parameters f_t, and G_f are strongly correlated, which is represented by the format of distribution assumed in Fig. 74c and Fig. 70c. In addition, the α parameter presented values in the interval of $\alpha = [2 - 5]$, for conventional concrete, and $\alpha = [4 - 5]$, for UHPC. This is expected since the UHPC presents a prolonged quasi-brittle behaviour, which is better represented by a higher-order shape function. Finally, the posterior distributions considering the UHPC provided lower coefficients of variation, which can be explained by the lower variability of experimental curves. The novelties presented herein have been published in Almeida, Atroshchenko and Leonel (2025)

Finally, several contributions in the field of three-dimensional nonlinear boundary formulations have been made, highlighting the viscous-cohesive crack growth analysis, the couple dipole-based BEM approach to PPR CZM and Bayesian updating. Besides, three papers were published (ALMEIDA; LEONEL, 2024b; ALMEIDA; LEONEL, 2024a; ALMEIDA; ATROSHCHENKO; LEONEL, 2025) with the advances made in this thesis.

7.1 Recommendations for future work

Perhaps one of the most appealing extensions of the work reported in this thesis is the extension of this formulation to the analysis of reinforced components. Nonlinear formulations via elastoplastic reinforcements and bond-slip components can be proposed. Such formulations allow to accurately model the pull-out phenomenon in 3D numerical models. The 3D dipole-based BEM represents the solid whereas the 1D approach of BEM models the reinforcements, which characterises a 3DBEM/1DBEM coupling technique. Besides, the experimental results presented in Santos and Sousa (2020) can be used to calibrate the viscous-cohesive parameters in polypropylene fiber reinforced concrete and steel fiber reinforced concrete.

Another important future contribution is the extension of this new formulation to isogeometric approach. In such case, NURBS surfaces can be used to model the fracture domain. Additionally, an outstanding contribution in this field would be the proposition of crack propagation schemes. Thus, special techniques, such as enrichment strategies, may be used to avoid the remeshing limitation in isogeometric approaches. The proposition of enriched formulations, using the Heavised function, to account the discontinuity in the displacement fields can be performed

Finally, this formulation can be extended to transient problems. In this regard, the dual reciprocity method (PARTRIDGE; BREBBIA; WROBEL, 1992b) can be used for the treatment of domain integrals, and elastic fundamental solutions can be considered in order to obtain the mass matrix. Besides, the time integrals can be analysed via Newmark algorithm.

BIBLIOGRAPHY

AGATHOS, K.; BORDAS, S.; CHATZI, E. Improving the conditioning of XFEM/GFEM for fracture mechanics problems through enrichment quasi-orthogonalization. **Computer Methods in Applied Mechanics and Engineering**, v. 346, p. 1051 – 1073, 2019.

ALIABADI, M. H. **The boundary element method, volume 2: applications in solids and structures**. [*S.l.: s.n.*]: John Wiley & Sons, 2002. v. 2.

ALMEIDA, L. P. R.; ATROSHCHENKO, E.; LEONEL, E. D. Viscous-cohesive fracture parameters quantification by the coupling of 3D dipole-based BEM formulation and bayesian updating model. **Engineering Structures**, v. 322, p. 119136, 2025.

ALMEIDA, L. P. R.; LEONEL, E. D. Dipole-based BEM formulation for three-dimensional cohesive crack propagation modelling. **International Journal for Numerical Methods in Engineering**, v. 125, n. 17, p. e7535, 2024.

ALMEIDA, L. P. R.; LEONEL, E. D. The fracture failure modelling of three-dimensional structures composed of quasi-brittle materials subjected to different loading velocities rates by the dipole-based BEM approach. **International Journal of Solids and Structures**, v. 286-287, p. 112595, 2024.

ALMEIDA, L. P. R.; LIMA JUNIOR, E.; BARBIRATO, J. C. C. Cohesive crack propagation analysis using a dipole BEM formulation with tangent operator. **Theoretical and Applied Fracture Mechanics**, v. 109, 2020.

ALMEIDA, L. P. R.; LIMA JUNIOR, E. T.; BARBIRATO, J. C. C. BEM-FORM model for the probabilistic response of circular tunnels in elastic media. **KSCE Journal of Civil Engineering**, v. 24, n. 7, p. 2244–2255, 2020.

ALMEIDA, L. P. R.; LIMA JUNIOR, E. T.; BARBIRATO, J. C. C. Probabilistic dipole BEM model for cohesive crack propagation analysis. **Journal of Brazilian Society of Mechanical Sciences and Engineering**, v. 44, 2022.

ANDRADE, H. C.; LEONEL, E. D. An enriched dual boundary element method formulation for linear elastic crack propagation. **Engineering Analysis with Boundary Elements**, Elsevier, v. 121, p. 158–179, 2020.

ASTROZA, R. *et al.* Bayesian updating of complex nonlinear fe models with high-dimensional parameter space using heterogeneous measurements and a batch-recursive approach. **Engineering Structures**, v. 201, p. 109724, 2019.

AU, S. Reliability-based design sensitivity by efficient simulation. **Computers Structures**, v. 83, n. 14, p. 1048–1061, 2005. ISSN 0045-7949. Uncertainties in Structural Mechanics and Analysis–Computational Methods.

AU, S.-K.; WANG, Y. **Engineering Risk Assessment with Subset Simulation**. [*S.l.: s.n.*]: John Willey Sons, 2008.

BARBIRATO, J. **Método dos Elementos de Contorno com a Reciprocidade Dual para a Análise Transiente Tridimensional da Mecânica do Fraturamento**. 1999. Tese (Doutorado) — Escola de Engenharia de São Carlos, Universidade de São Paulo, São Carlos, 1999.

BAZANT, Z.; GETTU, R. Rate effects and load relaxation in static fracture of concrete. **Aci Materials Journal**, v. 89, p. 456–468, 1992.

BAZAZZADEH, S.; MOSSAIBY, F.; SHOJAEI, A. An adaptive thermo-mechanical peridynamic model for fracture analysis in ceramics. **Engineering Fracture Mechanics**, v. 223, p. 1067– 08, 2020.

BECK, J. L. Bayesian system identification based on probability logic. **Structural Control and Health Monitoring**, v. 17, n. 7, p. 825–847, 2010.

BECK, J. L.; KATAFYGIOTIS, L. S. Updating models and their uncertainties. i: Bayesian statistical framework. **Journal of Engineering Mechanics**, v. 124, n. 4, p. 455–461, 1998.

BECK, J. L.; TAFLANIDIS, A. Prior and posterior robust stochastic predictions for dynamical systems using probability logic. **International Journal for Uncertainty Quantification**, v. 3, n. 4, p. 271–288, 2013. ISSN 2152-5080.

BELYTSCHKO, T.; BLACK, T. Elastic crack growth in finite elements with minimal remeshing. **International Journal of Numerical Methods in Engineering**, v. 45, n. 1, p. 601 – 620, 1999.

BENEDETTI, I.; GULIZZI, V.; MILAZZO, A. A microstructural model for homogenisation and cracking of piezoelectric polycrystals. **Computer Methods in Applied Mechanics and Engineering**, v. 357, p. 112595, 2019.

BENJAMIN, J.; CORNELL, C. A. **Probability, statistics, and decision for civil engineers**. [*S.l.: s.n.*]: McGraw Hill, New York, 1970.

BENTO, M. H. C.; PROENÇA, S. P. B.; DUARTE, C. A. Recovery strategies, a posteriori error estimation, and local error indication for second-order g/xfem and fem. **International Journal for Numerical Methods in Engineering**, v. 124, n. 13, p. 3025–3062, 2023.

BETZ, W. *et al.* Bayesian inference with reliability methods without knowing the maximum of the likelihood function. **Probabilistic Engineering Mechanics**, v. 53, p. 14–22, 2018.

BEVEN, K. **Environmental modelling: An uncertain future?** [*S.l.: s.n.*]: Oxford, U.K, 2008.

BITTENCOURT, T.; WAWRZYNEK, P.; INGRAFFEA, A. Quasi-automatic simulation of crack propagation for 2d lefm problems. **Engineering Fracture Mechanics**, v. 55, n. 1, p. 321 – 334, 1996.

BREBBIA, C. **The Boundary Element Method for Engineers**. [*S.l.: s.n.*]: Pentech Press, London, 1978.

BREBBIA, C. A.; DOMINGUEZ, J. **Boundary elements: an introductory course**. [*S.l.: s.n.*]: WIT press, 1994.

CARLONE, P. *et al.* Multiple crack growth prediction in aa2024-t3 friction stir welded joints, including manufacturing effects. **International Journal of Fatigue**, v. 90, p. 69 – 77, 2016.

CARPINTERI, A. Post-peak and post-bifurcation analysis of cohesive crack growth. **Engineering Fracture Mechanics**, v. 32, p. 265–278, 1989.

CERRONE, A. *et al.* Implementation and verification of the park–paulino–roesler cohesive zone model in 3d. **Engineering Fracture Mechanics**, v. 120, p. 26–42, 2014.

CERVERA, M.; BARBAT, G.; CHIUMENTI, M. Finite element modelling of quasi-brittle cracks in 2d and 3d with enhanced strain accuracy. **Computational Mechanics**, v. 60, 2017.

CHAVES, A.; PEIXOTO, R.; SILVA, R. Three dimensional cells with embedded strong discontinuity for material failure analysis by the boundary element method. **Eng. Anal. Bound. Elem.**, v. 133, n. 3, p. 107 – 119, 2021.

CHAVES, A.; PEIXOTO, R.; SILVA, R. Analysis of 3d quasi-brittle solids failures by crack growth using the strong discontinuity approach with the boundary element method,. **Int J Solids Struct**, v. 275, 2023.

CHEN, E. *et al.* Displacement discontinuity method for cohesive crack propagation. **Engineering Fracture Mechanics**, v. 190, 2018.

CHEN, S. *et al.* A nodal-based extrinsic cohesive/contact model for interfacial debonding analyses in composite structures. **Computers Structures**, v. 215, p. 80–97, 2019. ISSN 0045-7949.

CHEN, T.; WANG, Z.; CEN, Z. A symmetric galerkin multi-zone boundary element method for cohesive crack growth. **Engineering Fracture Mechanics**, v. 63, p. 591–609, 1999.

CHING, H.; YEN, S. Meshless local petrov-galerkin analysis for 2d functionally graded elastic solids under mechanical and thermal loads. **Composites Part B: Engineering**, v. 36, p. 223 – 240, 2005.

CISILINO, A.; ALIABADI, M.; OTEGUI, J. A three-dimensional boundary element formulation for the elastoplastic analysis of cracked bodies. **International Journal of Numerical Methods in Engineering**, v. 42, p. 237– 256, 1998.

CITARELLA, R.; BUCHHOLZ, F. Comparison of crack growth simulation by dbem and fem for sen-specimens undergoing torsion or bending loading. **Engineering Fracture Mechanics**, v. 75, p. 489 – 509, 2008.

CITARELLA, R. *et al.* Dbem crack propagation in friction stir welded aluminum joints. **Advanced Engineering Software**, v. 101, p. 50 – 59, 2016.

CORDEIRO, S.; LEONEL, E. Cohesive crack propagation modelling in wood structures using bem and the tangent operator technique. **Engineering Analysis with Boundary Elements**, v. 64, p. 111– 121, 2016.

CORDEIRO, S.; LEONEL, E. Mechanical modelling of three-dimensional cracked structural components using the isogeometric dual boundary element method. **Applied Mathematical Modelling**, v. 63, p. 415–444, 2018.

CORDEIRO, S.; LEONEL, E. An improved computational framework based on the dual boundary element method for three-dimensional mixed-mode crack propagation analyses. **Advances in Engineering Software**, v. 135, 2019.

CORDEIRO, S. G.; DAUMAS, G. O.; MONTEIRO, F. A. A general DBEM for mixed-mode cohesive crack problems. **Theoretical and Applied Fracture Mechanics**, v. 130, p. 104249, 2024.

CORDEIRO, S. G. F. **Contribuições às análises de fratura e fadiga de componentes tridimensionais pelo método dos elementos de contorno dual**. 2018. Tese (Doutorado) — Escola de Engenharia de São Carlos, Universidade de São Paulo, São Carlos, 2018.

CORDEIRO, S. G. F.; LEONEL, E. D.; BEAUREPAIRE, P. Quantification of cohesive fracture parameters based on the coupling of bayesian updating and the boundary element method. **Engineering Analysis with Boundary Elements**, v. 74, p. 49–60, 2017.

CROUCH, S. Solution of plane elasticity problems by the displacement discontinuity method. **International Journal of Numerical Methods in Engineering**, v. 10, p. 301– 342, 1976.

DIAZ, F. *et al.* Bayesian updating and model class selection with subset simulation. **Computer Methods in Applied Mechanics and Engineering**, v. 317, p. 1102–1121, 2017.

FONSECA, G. *et al.* 2-d crack propagation analysis using stable generalized finite element method with global-local enrichments. **Engineering Analysis with Boundary Elements**, v. 118, p. 70 – 83, 2020.

FREED, Y.; BANKS-SILLS, L. A new cohesive zone model for mixed mode interface fracture in bimaterials. **Engineering Fracture Mechanics**, v. 75, n. 15, p. 4583–4593, 2008.

GAO, X.-W. The radial integration method for evaluation of domain integrals with boundary-only discretization. **Engineering Analysis with Boundary Elements**, Elsevier, v. 26, n. 10, p. 905–916, 2002.

GARG, S.; PANT, M. A comprehensive review of applications. **International Journal of Computational Methods**, v. 15, p. 183 – 185, 2018.

GIANNELLA, V. *et al.* Fatigue life assessment in lateral support element of a magnet for nuclear fusion experiment "wendelstein 7-x". **Engineering Fracture Mechanics**, v. 178, p. 243 – 257, 2017.

GIANNELLA, V.; PERRELLA, M.; CITARELLA, R. Efficient fem-dbem coupled approach for crack propagation simulations. **Theoretical and Applied Fracture Mechanics**, v. 91, p. 76 – 85, 2017.

GIANNELLA, V. *et al.* Fem-dbem approach to simulate crack propagation in a turbine vane segment undergoing a fatigue load spectrum. **Procedia Structural Integrity**, v. 12, p. 479 – 491, 2018.

GOSPODINOV, G. Boundary element modelling of cohesive cracks using displacement discontinuity method. **International Journal of Solids and Structures**, 2003.

GU, Y. *et al.* An enriched radial point interpolation method (e-rpim) for analysis of crack tip fields. **Engineering Fracture Mechanics**, v. 78, p. 175 – 190, 2011.

GUIGGIANI, M.; GIGANTE, A. A general algorithm for multidimensional cauchy principal value integrals in the boundary element method. **Journal of Applied Mechanics**, v. 57, p. 906–, 1990.

GUIGGIANI, M. *et al.* A general algorithm for the numerical solution of hypersingular boundary integral equations. **Journal of Applied Mechanics**, v. 59, p. 604–, 1992.

GULIZZI, V.; BENEDETTI, I.; MILAZZO, A. A novel boundary element formulation for anisotropic fracture mechanics. **Theoretical and Applied Fracture Mechanics**, v. 104, p. 102329, 2019.

GULIZZI, V.; RYCROFT, C.; BENEDETTI, I. Modelling intergranular and transgranular micro-cracking in polycrystalline materials. **Computer Methods in Applied Mechanics and Engineering**, v. 329, p. 168–194, 2018.

HAYKIN, S. **Neural networks and learning machines**. [*S.l.: s.n.*]: New Jersey: Prentice Hall, 2009. third edit.

HILLERBORG, A.; MODEER, M.; PETERSON, P. Analysis of crack formation and crack growth in concrete by mean of failure mechanics and finite elements. **Cement and Concrete Research**, v. 6, p. 773–782, 1976.

KAVETSKI, D.; KUCZERA, G.; FRANKS, S. W. Bayesian analysis of input uncertainty in hydrological modeling: 1. theory. **Water Resources Research**, v. 42, n. 3, 2006. Available at: <https://agupubs.onlinelibrary.wiley.com/doi/abs/10.1029/2005WR004368>.

KELVIN, L. Note on the integration of the equations of equilibrium of an elastic solid. **Cambridge and Dublin Mathematical Journal**, v. 3, p. 87–89, 1848.

KENNEDY, M. C.; O'HAGAN, A. Bayesian calibration of computer models. **Journal of the Royal Statistical Society: Series B (Statistical Methodology)**, v. 63, n. 3, p. 425–464, 2001.

LEE, S.; KIM, K.; YOON, Y. Particle difference method for dynamic crack propagation. **International Journal of Impact Engineering**, v. 87, p. 132 – 145, 2016.

LEONEL, E.; VENTURINI, W. Non-linear boundary element formulation with tangent operator to analyse crack propagation in quasi-brittle materials. **Engineering Analysis with Boundary Elements**, v. 34, p. 122– 129, 2010.

LI, H.; LI, J.; YUAN, H. A review of the extended finite element method on macrocrack and microcrack growth simulations. **Theoretical and Applied Fracture Mechanics**, v. 97, n. 1, p. 236 – 249, 2018.

LIU, P.; ISLAM, M. A nonlinear cohesive model for mixed-mode delamination of composite laminates. **Composite Structures**, v. 106, p. 47–56, 2013.

LIU, W.; JUN, S.; ZHANG, Y. Reproducing kernel particle methods. **International Journal of Numerical Methods in Fluids**, v. 20, p. 1081 – 1166, 1995.

LU, Y.; BELYTSCHKO, T.; GU, L. A new implementation of the element free galerkin method. **Computer Methods in Applied Mechanics and Engineering**, v. 113, p. 397 – 414, 1994.

MAIER, G.; G., N.; CEN, Z. Symmetric galerkin boundary element method for quasi-brittle-fracture and frictional contact problems. **Computational Mechanics**, v. 13, 1993.

MI, Y.; ALIABADI, M. Dual boundary element method for three-dimensional fracture mechanics analysis. **Engineering Analysis with Boundary Elements**, v. 10, p. 161–171, 1992.

MOHAMMADI, S. **Extended Finite Element Method: For Fracture Analysis of Structures**. [*S.l.: s.n.*]: John Wiley Sons, 2008.

MORAIS, A. *et al.* Bilinear approximations to the mixed-mode I–II delamination cohesive law using an inverse method. **Composite Structures**, v. 122, p. 361–366, 2015.

MOST, T.; BUCHER, C. Energy-based simulation of concrete cracking using an improved mixed-mode cohesive crack model within a meshless discretization. **International Journal for Numerical and Analyical Methods in Geomechanics**, v. 31, p. 285–305, 2007.

NATKE, H. Updating computational models in the frequency domain based on measured data: a survey. **Probabilistic Engineering Mechanics**, v. 3, n. 1, p. 28–35, 1988. ISSN 0266-8920.

NGUYEN, V. P. Discontinuous galerkin/extrinsic cohesive zone modeling: Implementation caveats and applications in computational fracture mechanics. **Engineering Fracture Mechanics**, v. 128, p. 37–68, 2014.

OLIVEIRA, H.; LEONEL, E. Cohesive crack growth modelling based on an alternative nonlinear bem formulation. **Engineering Fracture Mechanics**, v. 111, p. 86–97, 2013.

PARK, K.; PAULINO, G. H. Computational implementation of the PPR potential-based cohesive model in abaqus: Educational perspective. **Engineering Fracture Mechanics**, v. 93, p. 239–262, 2012.

PARK, K.; PAULINO, G. H.; ROESLER, J. R. A unified potential-based cohesive model of mixed-mode fracture. **Journal of the Mechanics and Physics of Solids**, v. 57, n. 6, p. 891–908, 2009.

PARTRIDGE, P.; BREBBIA, C.; WROBEL, L. **The dual reciprocity boundary element method**. [*S.l.: s.n.*]: Southampton, CMP, 1992.

PARTRIDGE, P.; BREBBIA, C.; WROBEL, L. The dual reciprocity boundary element method. **Computational Mechanics Publications: Southampton**, 1992.

PEIXOTO, R.; RIBEIRO, G.; PITANGUEIRA, R. A boundary element method formulation for quasi-brittle material fracture analysis using the continuum strong discontinuity approach. **Engineering Fracture Mechanics**, v. 202, p. 47– 74, 2018.

PENG, X. *et al.* Isogeometric boundary element methods for three dimensional static fracture and fatigue crack growth. **Computer Methods in Applied Mechanics and Engineering**, v. 316, p. 151 – 185, 2017.

PERALTA, P.; RUIZ, R. O.; TAFLANIDIS, A. A. Bayesian identification of electromechanical properties in piezoelectric energy harvesters. **Mechanical Systems and Signal Processing**, v. 141, 2020. ISSN 0888-3270.

PORTELA, A.; ALIABADI, M. H.; ROOKE, D. P. The dual boundary element method: Effective implementation for crack problems. **International Journal for Numerical Methods in Engineering**, v. 33, n. 6, p. 1269–1287, 1992.

PRICE, R.; TREVELYAN, J. Boundary element simulation of fatigue crack growth in multi-site damage. **Engineering Analysis with Boundary Elements**, v. 43, p. 67– 75, 2014.

QIN, Y.; CHEN, S.; ASAI, M. A nodal-based lagrange multiplier/cohesive zone approach for three-dimensional dynamic crack simulations of quasi-brittle materials. **Engineering Fracture Mechanics**, Elsevier BV, v. 292, nov. 2023. ISSN 0013-7944. Publisher Copyright: © 2023 Elsevier Ltd.

RABCZUK, T.; BELYTSCHKO, T. Cracking particles: a simplified meshfree method for arbitrary evolving cracks. **International Journal of Numerical Methods in Engineering**, v. 61, p. 2316 – 2343, 2004.

REINHARDT, H. Loading rate, temperature, and humidity effects. fracture mechanics test methods for concrete. **RILEM Report of Technical Comitee 89-FMT**, 1990.

REINHARDT, H.; WEERHEIJM, J. Tensile fracture of concrete at high loading rates taking into account of inertia and crack velocity effects. **International Journal of Fracture**, v. 51, p. 31–42, 1991.

ROCHA, M.; LEONEL, E. The fracture failure of three-dimensional concrete structures subjected to concentrated loadings using the boundary element method. **Revista IBRACON Estruturas e Materiais.**, v. 15, 2022.

ROSA, A. *et al.* A loading rate dependent cohesive model for concrete fracture. **Engineering Fracture Mechanics**, v. 82, p. 195–208, 2012.

RUIZ, G. *et al.* Effect of loading rate on fracture energy of high strength concrete. **Strain**, v. 47, p. 518–524, 2010.

RUSH, H. Researches toward a general flexural theory for structural concrete. **Journal of the American Concrete Institute**, v. 57, 1960.

SALEH, A.; ALIABADI, M. Crack-growth analysis in concrete using boundary element method. **Engineering Fracture Mechanics**, v. 51, 1995.

SANTOS, F.; SOUSA, J. A viscous-cohesive model for concrete fracture in quasi-static loading rate. **Engineering Fracture Mechanics**, v. 228, p. 106893, 2020.

SOLLERO, P.; ALIABADI, M. Anisotropy analysis of cracks emanating from circular holes in composite laminates using the boundary element. **Engineering Fracture Mechanics**, v. 49, p. 213– 224, 1994.

SOMIGLIANA, C. Sopra l'equilibrio di un corpo elastico isotropo. **Il Nuovo Cimento (1877-1894)**, Springer, v. 17, n. 1, p. 140–148, 1885.

STEPHEN, S.; GETTU, R. Rate-dependence of the tensile behavior of fibre reinforced concrete in the quasi-static regime. **Materials and Structures**, v. 107, 2019.

STRAUB, D.; PAPAIOANNOU, I. Bayesian updating with structural reliability methods. **Journal of Engineering Mechanics**, v. 141, n. 3, 2015.

SUN, F.; DONG, C. Three-dimensional crack propagation and inclusion-crack interaction based on igabem. **Engineering Analysis with Boundary Elements**, v. 131, p. 1–114, 2021.

TANG, W. Probabilistic updating of flaw information. **Journal of Testing and Evaluation**, v. 1, n. 6, p. 459–467, 11 1973. ISSN 0090-3973. Available at: <https://doi.org/10.1520/JTE10051J>.

TIAN, H.-M. *et al.* Reliability-based monitoring sensitivity analysis for reinforced slopes using bus and subset simulation methods. **Engineering Geology**, v. 293, p. 106331, 2021.

TIAN, R.; WEN, L.; WANG, L. Three-dimensional improved XFEM (IXFEM) for static crack problems. **Computer Methods in Applied Mechanics and Engineering**, v. 343, p. 339 – 367, 2019.

UNGER, J.; ECKARDT, S.; KONKE, C. Modelling of cohesive crack growth in concrete structures with the extended finite element method. **Computer Methods in Applied Mechanics and Engineering**, v. 1966, n. 41-44, p. 4087 – 4100, 2007.

VEGT, I.; BREUGEL, K.; WEERHEIJM, J. Failure mechanisms of concrete under impact loading. **In: Carpinteri A, Gambarova P, Ferro G, Plizzari G, editors. Fracture mechanics of concrete structures. Taylor Francis Group**, p. 579–87, 2007.

WANG, B.; BACKER, H. D.; CHEN, A. An XFEM based uncertainty study on crack growth in welded joints with defects. **Theoretical and Applied Fracture Mechanics**, v. 86, p. 125 – 142, 2016.

WENG, J.-H.; LOH, C.-H.; YANG, J. N. Experimental study of damage detection by data-driven subspace identification and finite-element model updating. **Journal of Structural Engineering**, v. 135, n. 12, p. 1533 – 1544, 2009.

WINKLER, B. **Traglastuntersuchungen von unbewehrten und bewehrten Betonstrukturen auf der Grundlage eines objektiven Werkstoffgesetzes fu¨r Beton**. 2001. Tese (Doutorado) — University of Innsbruck, 2001.

WITTMAN, F. *et al.* Influence of age of loading, water-cement ratio and rate of loading on fracture energy of concrete. **Materials and Structures**, v. 20, p. 103–110, 1987.

XIAO, H.; YUE, Z. A three-dimensional displacement discontinuity method for crack problems in layered rocks. **International Journal of Rock Mechanics Mining Sciences**, v. 48, p. 412– 420, 2011.

XIAO, S.; YUE, Z.; XIAO, H. Dual boundary element method for analyzing three-dimensional cracks in layered and graded halfspaces. **Engineering Analysis with Boundary Elements**, v. 104, p. 135– 147, 2019.

XING, Y. *et al.* Quasi-static loading rate effects on fracture process zone development of mixed-mode (i-ii) fractures in rock-like materials. **Engineering Fracture Mechanics**, v. 240, p. 107365, 2020.

YANG, L.; YANG, Y.; ZHENG, H. A phase field numerical manifold method for crack propagation in quasi-brittle materials. **Engineering Fracture Mechanics**, v. 241, p. 1074– 27, 2021.

ZHANG, X. *et al.* Effect of loading rate on crack velocities in hsc. **International Journal of Impact Engineering**, v. 37, p. 359–370, 2010.

ZHENG, H. *et al.* Fracture analysis of functionally graded material by hybrid meshless displacement discontinuity method. **Engineering Fracture Mechanics**, v. 247, p. 1075–91, 2021.

ZHU, C.; LIN, G.; LI, J. Modelling cohesive crack growth in concrete beams using scaled boundary finite element method based on super-element remeshing technique. **Computers Structures**, v. 121, p. 76–86, 2013.

ZHU, C.; LIN, G.; LI, J. A fictitious crack XFEM with two new solution algorithms for cohesive crack growth modeling in concrete structures. **Engineering Computations**, v. 21, p. 473–497, 2015.

APPENDIX A

INITIAL STRESS TERM

Because BEM is essentially a boundary discretisation method, the domain integrals have importance in the formulations. The domain integrals can represent body or thermal forces, for instance. However, these terms can represent a huge range of nonlinear effects. The stress state of many elasticity problems can be split into elastic and initial stress origins. Then:

$$\sigma_{ij}^{\ell} = \sigma_{ij}^{t} - \sigma_{ij}^{0} \tag{A.1}$$

in which σ_{ij}^{t} indicates the total stress and σ_{ij}^{0} the initial stress.

Therefore, the stress expression above, Eq. A.1, can be utilised into the weighted residual technique for obtaining the BEM integral formulation. Then:

$$\int_{\Omega}(\sigma_{ij} + b_k)u_{lk}^{*} = 0 \rightarrow \int_{\Omega}\sigma_{kj,j}u_{lk}^{*}d\Omega + \int_{\Omega}b_k u_{lk}^{*}d\Omega = 0 \tag{A.2}$$

Integrating by parts the last equation one has:

$$\int_{\Gamma}\sigma_{kj}\eta_j u_{lk}^{*}d\Gamma - \int_{\Omega}\sigma_{kj}^{t}u_{lk,j}^{*}d\Omega + \int_{\Omega}b_k u_{lk}^{*}d\Omega = 0 \tag{A.3}$$

Rewritten Eq. A.3:

$$\int_{\Gamma}P_k u_{lk}^{*}d\Gamma - \int_{\Omega}\sigma_{kj}^{t}u_{lk,j}^{*}d\Omega + \int_{\Omega}b_k u_{lk}^{*}d\Omega = 0 \tag{A.4}$$

The Eq. A.1 enables rewriting Eq. A.4 as follows:

$$\int_{\Gamma}P_k u_{lk}^{*}d\Gamma - \int_{\Omega}u_{lk,j}^{*}\sigma_{lkj}^{*}d\Omega + \int_{\Omega}\sigma_{kj}^{0}\epsilon_{lkj}^{*}d\Omega + \int_{\Omega}b_k u_{lk}^{*}d\Omega = 0 \tag{A.5}$$

in which E indicates the constitutive elastic tensor. Integrating by parts the last equation one has:

$$\int_{\Gamma} P_k u^*_{lk} d\Gamma - \int_{\Gamma} u_{lk} \eta_j \sigma^*_{lkj} d\Gamma + \int_{\Omega} u_{lk} \sigma^*_{lk,j} d\Omega + \int_{\Omega} \sigma^0_{kj} \epsilon^*_{lkj} d\Omega + \int_{\Omega} b_k u^*_{lk} d\Omega = 0 \qquad \text{(A.6)}$$

Rewritten Eq. A.6:

$$\int_{\Gamma} P_k u^*_{lk} d\Gamma - \int_{\Gamma} u_{lk} P^*_k d\Gamma + \int_{\Omega} u_{lk} (-\Delta_k) d\Omega + \int_{\Omega} \sigma^0_{kj} \epsilon^*_{lkj} d\Omega + \int_{\Omega} b_k u^*_{lk} d\Omega = 0 \qquad \text{(A.7)}$$

where Δ indicates the Dirac's delta function, which appears from the fundamental problems statements. Applying the sifting property of this function one has:

$$u_{lk}(source) + \int_{\Gamma} u_{lk} P^*_k d\Gamma = \int_{\Gamma} P_k u^*_{lk} d\Gamma + \int_{\Omega} \sigma^0_{kj} \epsilon^*_{lkj} d\Omega + \int_{\Omega} b_k u^*_{lk} d\Omega = 0 \qquad \text{(A.8)}$$

Eq. A.8 is the Somigliana's equation including the initial stress term. In material nonlinearity problems, for instance, the initial stress term can be manipulated properly and leads to the effective approaches. The initial stress term provides the corrector stress values during the iterative process (Newton-Raphson), which is required in material nonlinear modelling. Thus, in such problems, the stress state must obey to the constitutive models. In the present formulation, the cohesive laws govern the mechanical material behaviour. Then, the equilibrium state evaluated during the try step must be verified in accordance with the cohesive laws. When, the constitutive model is violated, the corrector step is triggered. It leads to an iterative process, in which the stresses values are corrected iteratively. In the present formulation, the initial stress field has been manipulated and non-nil solely at the energy dissipation zone. As a result of this manipulation (presented in details in the manuscript), the variable dipoles appear, which provides the corrector stresses.

The proposed formulation is elegant and requires less integral equations per source point at the crack surface in comparison to well-known DBEM. Besides, the singularities involved in integral kernels are of same intensity. Therefore, the integration efforts in both formulations are equivalent.

APPENDIX B

EXPRESSIONS OF TENSOR G_{lj}^{ℓ} AND MATRIX K

The dipoles contributions for displacements, G_{lj}^{ℓ} ,can be defined as illustrated in Eq. B.1, accounting for the Kelvin fundamental solution, u_{lj}^{*},

$$G_{lj}^{\ell} = \frac{\partial u_{lj}^{*}}{\partial X_{\ell}} = \frac{\partial}{\partial X_{\ell}} \left\{ \frac{1}{16\pi \left(1-\upsilon\right)\mu} \left[\frac{(3-4\upsilon)}{r}\delta_{lj} + \frac{1}{r} r_{,l} r_{,j} \right] \right\} \tag{B.1}$$

Then, the tensor G_{lj}^{ℓ} can be expressed using the constant, K_1, K_2 e C_1: where K_1, K_2 and C_1 are as follows:

$$\begin{aligned} K_1 &= \frac{\partial}{\partial X_{\ell}} \left\{ \frac{(3-4\upsilon)}{r}\delta_{lj} \right\} \\ K_2 &= \frac{\partial}{\partial X_{\ell}} \left\{ \frac{1}{r} r_{,l} r_{,j} \right\} \\ C_1 &= \frac{1}{16\pi \left(1-\upsilon\right)\mu} \end{aligned} \tag{B.2}$$

The expression resulting from the derivatives of the first part is as follows:

$$K_1 = \frac{\partial}{\partial X_{\ell}} \left\{ \frac{(3-4\upsilon)}{r}\delta_{lj} \right\} = -\frac{1}{r^2} r_{,\ell} \left(3-4\upsilon\right)\delta_{lj} \tag{B.3}$$

The second part of Eq. B.1 results in:

$$\begin{aligned} K_2 = \frac{\partial}{\partial X_{\ell}} \left\{ \frac{1}{r} r_{,l} r_{,j} \right\} = \frac{\partial}{\partial X_{\ell}} \left(\frac{1}{r} \right) r_{,l} r_{,j} + \frac{1}{r} \frac{\partial^2 r}{\partial X_{\ell} \partial X_{l}} r_{,j} + \frac{1}{r} \frac{\partial^2 r}{\partial X_{\ell} \partial X_{j}} r_{,l} \quad \Rightarrow \\ K_2 = \frac{\partial}{\partial X_{\ell}} \left\{ \frac{1}{r} r_{,l} r_{,j} \right\} = \left(-\frac{1}{r^2} r_{,\ell} \right) r_{,l} r_{,j} + \frac{1}{r} \left[\frac{1}{r} \left(\delta_{\ell l} - r_{,\ell} r_{,l} \right) \right] r_{,j} \\ + \frac{1}{r} \left[\frac{1}{r} \left(\delta_{\ell j} - r_{,\ell} r_{,l} \right) \right] r_{,l} \end{aligned} \tag{B.4}$$

Thus:

$$G_{lj}^{\ell} = \frac{\partial u_{lj}^{*}}{\partial X_{\ell}} = \frac{K_1 + K_2}{C_1} \Rightarrow$$
$$G_{lj} = \frac{1}{16\pi\,(1-\upsilon)\,\mu r^2}\left\{-\,(3-4\upsilon)\,r_{,\ell}\delta_{lj} + r_{,j}\delta_{\ell l} + r_{,l}\delta_{\ell j} - 3r_{,l}r_{,j}r_{,\ell}\right\} \tag{B.5}$$

The tensor G_{lj}^{ℓ} components are as follows:

$$\begin{aligned}
G_{i1}^{1} &= \frac{1}{16\pi(1-\upsilon)\mu r^2}\left\{-(3-4\upsilon)r_{,1}\delta_{i1} + r_{,1}\delta_{1i} + r_{,i} - 3r_{,1}^2 r_{,i}\right\} \\
G_{i2}^{1} &= \frac{1}{16\pi(1-\upsilon)\mu r^2}\left\{-(3-4\upsilon)r_{,1}\delta_{i2} + r_{,2}\delta_{1i} - 3r_{,1}r_{,2}r_{,i}\right\} \\
G_{i3}^{1} &= \frac{1}{16\pi(1-\upsilon)\mu r^2}\left\{-(3-4\upsilon)r_{,1}\delta_{i3} + r_{,3}\delta_{1i} - 3r_{,1}r_{,3}r_{,i}\right\} \\
G_{i1}^{2} &= \frac{1}{16\pi(1-\upsilon)\mu r^2}\left\{-(3-4\upsilon)r_{,2}\delta_{i1} + r_{,1}\delta_{2i} - 3r_{,2}r_{,i}r_{,1}\right\} \\
G_{i2}^{2} &= \frac{1}{16\pi(1-\upsilon)\mu r^2}\left\{-(3-4\upsilon)r_{,2}\delta_{i2} + r_{,2}\delta_{2i} + r_{,i} - 3r_{,2}^2 r_{,i}\right\} \\
G_{i3}^{2} &= \frac{1}{16\pi(1-\upsilon)\mu r^2}\left\{-(3-4\upsilon)r_{,2}\delta_{i3} + r_{,3}\delta_{2i} - 3r_{,2}r_{,i}r_{,3}\right\} \\
G_{i1}^{3} &= \frac{1}{16\pi(1-\upsilon)\mu r^2}\left\{-(3-4\upsilon)r_{,3}\delta_{i1} + r_{,1}\delta_{3i} - 3r_{,3}r_{,i}r_{,1}\right\} \\
G_{i2}^{3} &= \frac{1}{16\pi(1-\upsilon)\mu r^2}\left\{-(3-4\upsilon)r_{,3}\delta_{i2} + r_{,2}\delta_{3i} - 3r_{,3}r_{,i}r_{,2}\right\} \\
G_{i3}^{3} &= \frac{1}{16\pi(1-\upsilon)\mu r^2}\left\{-(3-4\upsilon)r_{,3}\delta_{i3} + r_{,3}\delta_{3i} - 3r_{,3}^2 r_{,i}\right\}
\end{aligned} \tag{B.6}$$

The formulation proposed in this study utilises the tensor G_{lj}^{ℓ} components into a condensed form. Then:

$$\begin{aligned}
K_{i1} &= G_{i3}^{1} + G_{i1}^{3} \\
K_{i2} &= G_{i3}^{2} + G_{i2}^{3} \\
K_{i1} &= \frac{\upsilon}{1-\upsilon}(G_{i1}^{1} + G_{i2}^{2}) + G_{i3}^{3}
\end{aligned} \tag{B.7}$$

The expressions in Eq. B.6 enable the influence terms of K matrix, which are as follows:

$$
\begin{aligned}
K_{11} &= \frac{1}{16\pi(1-v)\mu r^2} 2r_{,3}\left[-(1-2v)-3r_{,1}^2\right] \\
K_{12} &= \frac{1}{16\pi(1-v)\mu r^2}(-6r_{,1}r_{,2}r_{,3}) \\
K_{13} &= \frac{1}{16\pi(1-v)\mu r^2} r_{,1}\frac{r_{,1}}{(1-v)}\left[1-(1-v)v-3v(r_{,1}^2+r_{,2}^2-r_{,3}^2)-3r_{,3}^2\right] \\
K_{21} &= \frac{1}{16\pi(1-v)\mu r^2}(-6r_{,1}r_{,2}r_{,3}) \\
K_{22} &= \frac{1}{16\pi(1-v)\mu r^2} 2r_{,3}\left[-(1-2v)-3r_{,2}^2\right] \\
K_{23} &= \frac{1}{16\pi(1-v)\mu r^2}\frac{r_{,2}}{(1-v)}\left[1-(1-v)v-3v(r_{,1}^2+r_{,2}^2-r_{,3}^2)-3r_{,3}^2\right] \\
K_{31} &= \frac{1}{16\pi(1-v)\mu r^2} 2r_{,1}\left[-(1-2v)-3r_{,3}^2\right] \\
K_{32} &= \frac{1}{16\pi(1-v)\mu r^2} 2r_{,2}\left[-(1-2v)-3r_{,3}^2\right] \\
K_{33} &= \frac{1}{16\pi(1-v)\mu r^2}\frac{r_{,3}}{(1-v)}\left[-1+(7-4v)v-3v(r_{,1}^2+r_{,2}^2-r_{,3}^2)-3r_{,3}^2\right]
\end{aligned}
\tag{B.8}
$$

APPENDIX C

EXPRESSIONS OF TENSOR G_{ij}^{ml} AND MATRIX KS KS

This appendix demonstrates the dipole contributions to the stresses components. G_{ij}^{ml} can be expressed from Eq. 3.23 and Eq. 3.34, as follows:

$$G_{ij}^{ml} = \lambda\delta_{lj}\frac{\partial G_{wj}^{l}}{\partial X_w} + \mu\left(\frac{\partial G_{ij}^{l}}{\partial X_m} + \frac{\partial G_{mj}^{l}}{\partial X_i}\right) \tag{C.1}$$

The derivatives of Equation Eq. C.1 lead to:

$$\frac{\partial G_{ij}^{l}}{\partial X_m} = \frac{1}{16\pi(1-v)\mu}\left\{\begin{array}{c} -(3-4v)\frac{\partial}{\partial X_m}\left(\frac{r_{,l}}{r^2}\right)\delta_{ij} + \frac{\partial}{\partial X_m}\left(\frac{r_{,j}}{r^2}\right) + \\ +\frac{\partial}{\partial X_m}\left(\frac{r_{,i}}{r^2}\right)\delta_{lj} - 3\frac{\partial}{\partial X_m}\left(\frac{1}{r^2}\right)r_{,i}r_{,j}r_{,l} - \frac{3}{r^2}\frac{\partial r_{,i}}{\partial X_m}r_{,j}r_{,l} + \\ -\frac{3}{r^2}\frac{\partial r_{,j}}{\partial X_m}r_{,i}r_{,l} - \frac{3}{r^2}\frac{\partial r_{,l}}{\partial X_m}r_{,i}r_{,j} \end{array}\right\} \tag{C.2}$$

in which:

$$\begin{aligned} \frac{\partial}{\partial X_m}\left(\frac{r_{,\ell}}{r^2}\right) &= \frac{\partial}{\partial X_m}\left(\frac{1}{r^2}\right) + \frac{1}{r^2}\frac{\partial r_{,\ell}}{\partial X_m} \\ \frac{\partial}{\partial X_m}\left(\frac{r_{,\ell}}{r^2}\right) &= -\left(-\frac{2r_{,m}r_{,\ell}}{r^3} + \frac{1}{r^2}\left[\frac{1}{r}\left(\delta_{m\ell} - r_{,m}r_{,\ell}\right)\right]\right) \\ \frac{\partial}{\partial X_m}\left(\frac{r_{,j}}{r^2}\right) &= \frac{1}{r^3}\left(3r_{,m}r_{,j} - \delta_{mj}\right) \\ \frac{\partial}{\partial X_m}\left(\frac{r_{,i}}{r^2}\right) &= \frac{1}{r^3}\left(3r_{,m}r_{,i} - \delta_{mi}\right) \\ \frac{\partial}{\partial X_m}\left(\frac{1}{r^2}\right) &= \frac{2r_{,m}}{r^3} \\ \frac{\partial r_{,i}}{\partial X_m} &= \frac{1}{r}\left(r_{,m}r_{,i} - \delta_{mi}\right) \\ \frac{\partial r_{,j}}{\partial X_m} &= \frac{1}{r}\left(r_{,m}r_{,j} - \delta_{mj}\right) \\ \frac{\partial r_{,\ell}}{\partial X_m} &= \frac{1}{r}\left(r_{,m}r_{,\ell} - \delta_{m\ell}\right) \end{aligned} \tag{C.3}$$

Eq. C.1 and Eq. C.2, lead to:

$$\frac{G_{lj}^{\ell}}{\partial X_m} = \frac{1}{16\pi\left(1-\upsilon\right)\mu r^3}\left\{\begin{array}{c} -\left(3-\upsilon\right)\left(\delta_{ij}\delta_{m\ell}-3\delta_{lj}r_{,m}r_{,\ell}\right)-\left(\delta_{mj}\delta_{\ell i}+\delta_{mi}\delta_{lj}\right)+ \\ +3\left(\delta_{j\ell}r_{,m}r_{,\ell}+\delta_{ij}r_{,m}r_{,i}+\delta_{i\ell}r_{,m}r_{,j}+\delta_{mj}r_{,i}r_{,\ell}+\delta_{mi}r_{,j}r_{,\ell}\right)+ \\ -15r_{,l}r_{,j}r_{,m}r_{,\ell} \end{array}\right\} \tag{C.4}$$

In addition:

$$\frac{G_{lj}^{\ell}}{\partial X_m} = \frac{1}{16\pi\left(1-\upsilon\right)\mu r^3}\left\{\begin{array}{c} \left(3-\upsilon\right)\left(\delta_{ij}\delta_{m\ell}-3\delta_{lj}r_{,m}r_{,\ell}\right)-\left(\delta_{mj}\delta_{\ell i}+\delta_{mi}\delta_{lj}\right)+ \\ +3\left(\delta_{j\ell}r_{,m}r_{,\ell}+\delta_{ij}r_{,m}r_{,i}+\delta_{i\ell}r_{,m}r_{,j}+\delta_{mj}r_{,i}r_{,\ell}+\delta_{mi}r_{,j}r_{,\ell}\right)+ \\ -15r_{,l}r_{,j}r_{,m}r_{,\ell} \end{array}\right\} \tag{C.5}$$

as,

$$\frac{G_{wj}^{\ell}}{\partial X_w} = \frac{\left(1-2\upsilon\right)}{16\pi\left(1-\upsilon\right)\mu r^3}\left(2\delta_{\ell j-6r_{,j}r_{,\ell}}\right) \tag{C.6}$$

Finally, the tensor $G_{lj}^{m\ell}$ is as follows:

$$G_{lj}^{m\ell} = \frac{1}{8\pi\left(1-\upsilon\right)r^3}\left\{\begin{array}{c} \left(1-2\upsilon\right)\left(\delta_{mj}\delta_{l\ell}+\delta_{lj}\delta_{\ell m}-\delta_{ml}\delta_{\ell j}\right)+ \\ 3\left(1-2\upsilon\right)\left(\delta_{mj}r_{,l}r_{,\ell}+\delta_{lj}r_{,m}r_{,\ell}-\delta_{lm}r_{,j}r_{,\ell}\right)- \\ 3\left(\delta_{\ell j}r_{,l}r_{,m}+\delta_{m\ell}r_{,j}r_{,l}+\delta_{\ell l}r_{,m}r_{,j}\right)-15r_{,l}r_{,j}r_{,m}r_{,\ell} \end{array}\right\} \tag{C.7}$$

The proposed formulation condensates the dipoles contributions as demonstrated in Eq. 3.29. This procedure leads to the KS matrix, which is as follows:

$$\begin{aligned} KS_{i1}^{m} &= G_{i3}^{m1}+G_{i1}^{m3} \\ KS_{i2}^{m} &= G_{i3}^{m2}+G_{i2}^{m3} \\ KS_{i3}^{m} &= \frac{\upsilon}{1-\upsilon}(G_{i1}^{m1}+G_{i2}^{m2})+G_{i3}^{m3} \end{aligned} \tag{C.8}$$

These terms can be presented explicitly as follows:

$$KS^1_{11} = \frac{1}{8\pi(1-v)r^3} 6 r_{,1} r_{,3} \left[1 - 5 r^2_{,1}\right]$$

$$KS^1_{12} = \frac{1}{8\pi(1-v)r^3} 6 r_{,2} r_{,3} \left[(1-2v) - 5 r^2_{,1}\right]$$

$$KS^1_{13} = \frac{1}{8\pi(1-v)r^2} \frac{1}{(1-v)} \left[\begin{array}{c} -(1-3v+2v^2) + 3(r^2_{,1} + r^2_{,3} - 5 r^2_{,1} r^2_{,3}) + \\ -3v(-2r^2_{,1} + 5 r^4_{,1} - r^2_{,2} + 5 r^2_{,1} r^2_{,2} + 3 r^2_{,3} - 5 r^2_{,1} r^2_{,3}) - \\ 6v^2(-r^2_{,1} + r^2_{,2} - r^2_{,3}) \end{array} \right]$$

$$KS^1_{21} = \frac{1}{8\pi(1-v)r^3} 6 r_{,2} r_{,3} \left[1 - 5 r^2_{,1}\right]$$

$$KS^1_{22} = \frac{1}{8\pi(1-v)r^3} 6 r_{,1} r_{,3} \left[1 - 5 r^2_{,2}\right]$$

$$KS^1_{23} = \frac{1}{8\pi(1-v)r^3} \frac{3 r_{,1} r_{,2}}{(1-v)} \left[(1+v+4v^2) - 5(r^2_{,3} + r^2_{,1} v + r^2_{,2} v - r^2_{,3} v\right]$$

$$KS^1_{31} = \frac{1}{8\pi(1-v)r^3} \left[2(1-2v) + 6(-5 r^2_{,1} r^2_{,3} + r^2_{,1} v + r^2_{,3} v\right]$$

$$KS^1_{32} = \frac{1}{8\pi(1-v)r^3} 6 r_{,1} r_{,2} \left[v - 5 r^2_{,3}\right]$$

$$KS^1_{33} = \frac{1}{8\pi(1-v)r^3} \frac{3 r_{,1} r_{,2}}{(1-v)} \left[(1+3v) - 5(r^2_{,3} + r^2_{,1} v + r^2_{,2} v - r^2_{,3} v)\right]$$

$$KS^2_{11} = \frac{1}{8\pi(1-v)r^3} 6 r_{,2} r_{,3} \left[v - 5 r^2_{,1}\right]$$

$$KS^2_{12} = \frac{1}{8\pi(1-v)r^3} 6 r_{,1} r_{,3} \left[v - 5 r^2_{,2}\right] \quad \text{(C.9)}$$

$$KS^2_{13} = \frac{1}{8\pi(1-v)r^3} \frac{3 r_{,1} r_{,2}}{(1-v)} \left[(1+v+4v^2) - 5(r^2_{,3} + r^2_{,1} v + r^2_{,2} v - r^2_{,3} v\right]$$

$$KS^2_{21} = \frac{1}{8\pi(1-v)r^3} 6 r_{,1} r_{,3} \left[(1-2v) - 5 r^2_{,2}\right]$$

$$KS^2_{22} = \frac{1}{8\pi(1-v)r^3} 6 r_{,2} r_{,3} \left[v - 5 r^2_{,2}\right]$$

$$KS^2_{23} = \frac{1}{8\pi(1-v)r^2} \frac{1}{(1-v)} \left[\begin{array}{c} -(1-3v+2v^2) + 3(r^2_{,2} + r^2_{,3} - 5 r^2_{,2} r^2_{,3}) - \\ -3v(-2r^2_{,2} + 5 r^4_{,2} - r^2_{,1} + 5 r^2_{,1} r^2_{,2} + 3 r^2_{,3} - 5 r^2_{,2} r^2_{,3} - \\ 6v^2(-r^2_{,1} - r^2_{,2} - r^2_{,3}) \end{array} \right]$$

$$KS^2_{31} = \frac{1}{8\pi(1-v)r^3} 6 r_{,1} r_{,2} \left[v - 5 r^2_{,3}\right]$$

$$KS^2_{32} = \frac{1}{8\pi(1-v)r^3} \left[2(1-2v) + 6(-5 r^2_{,2} r^2_{,3} + r^2_{,2} v - r^2_{,3} v\right]$$

$$KS^2_{33} = \frac{1}{8\pi(1-v)r^3} \frac{3 r_{,2} r_{,3}}{(1-v)} \left[(1+3v) - 5(r^2_{,3} + r^2_{,1} v + r^2_{,2} v - r^2_{,3} v\right]$$

$$KS^3_{11} = \frac{1}{8\pi(1-v)r^3} \left[2(1-2v) + 6(-5 r^2_{,1} r^2_{,3} + r^2_{,1} v - r^2_{,3} v\right]$$

$$KS^3_{12} = \frac{1}{8\pi(1-v)r^3} 6 r_{,1} r_{,2} \left[v - 5 r^2_{,3}\right]$$

$$KS^3_{13} = \frac{1}{8\pi(1-v)r^3} \frac{3 r_{,1} r_{,3}}{(1-v)} \left[(1+3v) - 5(r^2_{,3} + r^2_{,1} v + r^2_{,2} v - r^2_{,3} v\right]$$

$$
\begin{aligned}
KS^3_{21} &= \frac{1}{8\pi(1-v)r^3} 6 r_{,1} r_{,2} \left[v - 5 r^2_{,3} \right] \\
KS^3_{22} &= \frac{1}{8\pi(1-v)r^3} \left[(2-4v) + 6(-5 r^2_{,2} r^2_{,3} + r^2_{,2} v + r^2_{,3} v) \right] \\
KS^3_{23} &= \frac{1}{8\pi(1-v)r^3} \frac{3 r_{,2} r_{,3}}{(1-2v)} \left[(1+3v) - 5(r^2_{,3} + r^2_{,1} v + r^2_{,2} v - r^2_{,3} v) \right] \\
KS^3_{31} &= \frac{1}{8\pi(1-v)r^3} 6 r_{,1} r_{,3} \left[1 - 5 r^2_{,3} \right] \\
KS^3_{32} &= \frac{1}{8\pi(1-v)r^3} 6 r_{,2} r_{,3} \left[1 - 5 r^2_{,3} \right] \\
KS^2_{33} &= \frac{1}{8\pi(1-v)r^2} \frac{1}{(1-v)} [-(1 + 5v - 6v^2) + 3(2 r^2_{,3} - 5 r^4_{,3}) - \\
&\quad -3v(-r^2_{,1} - r^2_{,2} + 5 r^2_{,1} r^2_{,3} - 2 r^2_{,3} - 5 r^4_{,3} + 5 r^2_{,2} r^2_{,3}) - \\
&\quad -6v^2 (r^2_{,1} + r^2_{,2} + r^2_{,3})]
\end{aligned}
\tag{C.10}
$$

APPENDIX D

EVALUATION OF HYPERSINGULAR KERNELS

This appendix demonstrates the regularisation terms of the dipoles integral kernel associated to the stresses values. This procedure is necessary for integrating the singular boundary elements, that is, the boundary elements containing the source point. Eq. 3.37 presents this kernel, which contains a hypersingularity, that is, of order $O(1/r^3)$. This kernel can be regularised with the techniques proposed by Guiggiani and Gigante (1990), Guiggiani *et al.* (1992).

The regularisation starts with the collocation point y at a smooth boundary element Γ_e, Fig. 76. One accounts for an additional/auxiliary circular region along Γ_ε with radius ε (CORDEIRO, 2018). In the parametric space $\xi_1 \times \xi_2$, the source point y and the additional/auxiliary circular region can be represented by $\Upsilon = \{\xi_1^0,\xi_2^0\}$ and σ_ε, in which the latter is not necessarily circular after the mapping process. The procedures in the following transforms the description into Cartesian coordinates to Polar coordinates. Then, the boundary of the region σ_ε can be represented in polar coordinates, $\alpha(\rho,\theta)$, and $\widehat{\rho}(\theta)$ is the upper limit of ρ for a given θ.

Figure 76 – Mapping of the boundary element that contains the collocation point

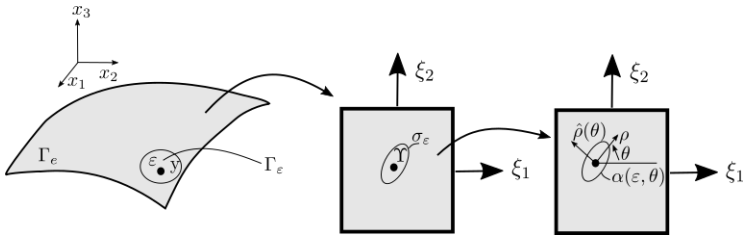

Source: The author.

Because of the hypersingularity in the kernel $G_{lj}^{m\ell}$, the integration of the singular element must be carried out along the boundary $\Gamma_e - \Gamma_\varepsilon$ in the limit of $\varepsilon \to 0$.The treatment of the hypersingular kernel involves the analytical evaluation of this integral within the Hadamard finite part, as follows:

$$\int_{\Gamma_e} G_{lj}^{m\ell}(y,x) q_j^{\ell}(x) d\Gamma^C = \lim_{\varepsilon \to 0^+} \left\{ \int_{(\Gamma_e - \Gamma_\varepsilon)} G_{lj}^{m\ell}(y,x) q_j^{\ell}(x) d\Gamma^C + q_j^{\ell}(y) \frac{b_{kij}(y)}{\varepsilon} \right\} \tag{D.1}$$

Eq. D.1 can be expressed in the parametric space as follows:

$$I_S = \lim_{\varepsilon \to 0^+} \left\{ \int_{(R_e - \sigma_\varepsilon} G_{lj}^{m\ell}(y,x(\xi)) N^{\alpha}(\xi) J(\xi) d\xi + N^{\alpha}(\Upsilon) \frac{b_{kij}(y)}{\varepsilon} \right\} \tag{D.2}$$

Then, Eq. D.2 can be rewritten in polar coordinates as follows:

$$I_S = \lim_{\varepsilon \to 0^+} \left\{ \int_0^{2\pi} \int_{\alpha(\varepsilon,\theta)}^{\widehat{\rho}(\theta)} G(\rho,\theta) d\rho d\theta + N(Y) \otimes \frac{b_{kij}(y)}{\varepsilon} \right\} \tag{D.3}$$

The transformation to the Polar coordinates introduces a jacobian ρ jacobian, which reduces the kernel singularity in one order, that is $O(1/\rho^3)$ to $O(1/\rho^2)$. As presented by Guiggiani and Gigante (1990), Guiggiani *et al.* (1992), the kernel $G(\rho,\theta)$ can be expanded into a Laurent series as follows:

$$G(\rho,\theta) = \frac{G\_2(\theta)}{\rho^2} + \frac{G\_1(\theta)}{\rho} + O(1) \tag{D.4}$$

The asymptotic behaviour of G when ρ tends to zero can be represented by the first two terms of this expansion, Eq. D.4. Then, the concept of univariate singularity subtraction presented in reference Guiggiani *et al.* (1992) can be applied straightforwardly. Then:

$$\begin{aligned} I_S = \lim_{\varepsilon \to 0^+} & \left\{ \left\{ \int_0^{2\pi} \int_{\alpha(\varepsilon,\theta)}^{\bar{\rho}(\theta)} \left[G(\rho,\theta) - \left(\frac{G\_2(\theta)}{\rho^2} + \frac{G\_1(\theta)}{\rho} \right) \right] d\rho d\theta \right\} \right. \\ & \left\{ + \int_0^{2\pi} \int_{\alpha(\varepsilon,\theta)}^{\bar{\rho}(\theta)} \frac{G\_1(\theta)}{\rho} d\rho d\theta \right\} \\ & \left. \left\{ + \int_0^{2\pi} \int_{\alpha(\varepsilon,\theta)}^{\bar{\rho}(\theta)} \frac{G\_2(\theta)}{\rho^2} d\rho d\theta + N(Y) \otimes \frac{b(y)}{\varepsilon} \right\} \right. \\ & = I_{S\_0} + I_{S\_1} + I_{S\_2} \end{aligned} \tag{D.5}$$

The integral I_{S_0} is now regular, since the subtraction of the hypersingularity has been guaranteed by the asymptotic behaviour of the Laurent expansion, Eq. D.4. Therefore, treating each term separately one has:

$$I_{S\_0} = \int_0^{2\pi} \int_{\alpha(\varepsilon,\theta)}^{\overline{\rho}(\theta)} \left[G(\rho,\theta) - \left(\frac{G\_2(\theta)}{\rho^2} + \frac{G\_1(\theta)}{\rho} \right) \right] d\rho d\theta \tag{D.6}$$

The term $\alpha(\varepsilon,\theta)$ appears due to the limiting process in the integrals I_{S_1} and I_{S_2}:

$$\alpha(\varepsilon,\theta) = \varepsilon\beta(\theta) + \varepsilon^2\gamma(\theta) + O(\varepsilon^3) \tag{D.7}$$

In the case of integrals I_{S_1} and I_{S_2}, the limit process requires special attention. It is possible to isolate the asymptotic behaviour of $\alpha(\varepsilon,\theta)$ when ε tends to zero. The term I_{S_1} can be rewritten as follows:

$$\begin{aligned}
I_{S_1} &= \lim_{\varepsilon\to 0^+} \int_0^{2\pi} \int_{\alpha(\varepsilon,\theta)}^{\overline{\rho}(\theta)} \frac{G_1(\theta)}{\rho} d\rho d\theta = \lim_{\varepsilon\to 0^+} \int_0^{2\pi} G_1(\theta) \left[\ln|\widehat{\rho}(\theta)| - \ln|\alpha(\varepsilon,\theta)| \right] d\theta \\
I_{S_1} &= \lim_{\varepsilon\to 0^+} \int_0^{2\pi} G_1(\theta) \ln|\widehat{\rho}(\theta)| d\theta - \lim_{\varepsilon\to 0^+} \int_0^{2\pi} G_1(\theta) \ln|\varepsilon\beta(\theta)| d\theta \\
I_{S_1} &= \lim_{\varepsilon\to 0^+} \int_0^{2\pi} G_1(\theta) \ln\left| \frac{\widehat{\rho}(\theta)}{\beta(\theta)} \right| d\theta - \lim_{\varepsilon\to 0^+} \ln|\varepsilon| \int_0^{2\pi} G_1(\theta) d\theta \\
I_{S_1} &= \lim_{\varepsilon\to 0^+} \int_0^{2\pi} G_1(\theta) \ln\left| \frac{\widehat{\rho}(\theta)}{\beta(\theta)} \right| d\theta
\end{aligned} \tag{D.8}$$

The term I_{S_2}presents the highest singularity, $O(1/\rho^2)$, and can be expressed as:

$$\begin{aligned}
I_{S_2} &= \lim_{\varepsilon\to 0^+} \left\{ \int_0^{2\pi} \int_{\alpha(\varepsilon,\theta)}^{\overline{\rho}(\theta)} \frac{G_2(\theta)}{\rho^2} d\rho d\theta + N(Y) \otimes \frac{b(y)}{\varepsilon} \right\} \\
I_{S_2} &= \lim_{\varepsilon\to 0^+} \left\{ \int_0^{2\pi} G_2(\theta) \left[-\frac{1}{\widehat{\rho}(\theta)} + \frac{1}{\alpha(\varepsilon,\theta)} \right] d\theta + N(Y) \otimes \frac{b(y)}{\varepsilon} \right\} \\
I_{S_2} &= \lim_{\varepsilon\to 0^+} \left\{ \int_0^{2\pi} \frac{G_2(\theta)}{\varepsilon\beta(\theta)} \left[1 - \varepsilon\frac{\gamma(\theta)}{\beta(\theta)} \right] d\theta + N(Y) \otimes \frac{b(y)}{\varepsilon} \right\} - \int_0^{2\pi} \frac{G_2(\theta)}{\widehat{\rho}(\theta)} d\theta \\
I_{S_2} &= \lim_{\varepsilon\to 0^+} \frac{1}{\varepsilon} \left\{ \int_0^{2\pi} \frac{G_2(\theta)}{\beta(\theta)} d\theta + N(Y) \otimes b(y) \right\} - \int_0^{2\pi} G_2(\theta) \left[\frac{\gamma(\theta)}{\beta^2(\theta)} + \frac{1}{\widehat{\rho}(\theta)} \right] d\theta \\
I_{S_2} &= -\int_0^{2\pi} G_2(\theta) \left[\frac{\gamma(\theta)}{\beta^2(\theta)} + \frac{1}{\widehat{\rho}(\theta)} \right] d\theta
\end{aligned} \tag{D.9}$$

Finally, during the limit process, the term $N(Y) \otimes b(y)/\varepsilon$, cancels the term G_2, and the final equation can be represented as follows:

$$I_S = \int_0^{2\pi} \int_0^{\widehat{\rho}(\theta)} \left[G\left(\rho,\theta\right) - \left(\frac{G_{\_2}(\theta)}{\rho^2} + \frac{G_{\_1}(\theta)}{\rho} \right) \right] d\rho d\theta$$
$$I_S = \int_0^{2\pi} \left[G_{\_1}\left(\theta\right) \ln \left| \frac{\widehat{\rho}(\theta)}{\beta(\theta)} \right| - G_{\_2}\left(\theta\right) \left(\frac{\gamma(\theta)}{\beta^2} + \frac{G_{\_1}(\theta)}{\widehat{\rho}(\theta)} \right) \right] d\theta \tag{D.10}$$

APPENDIX E

EXPLICIT EXPRESSIONS OF HYPERSINGULAR KERNELS

This appendix presents explicit expressions for the dipoles kernels regularisation. These expressions account for the Taylor expansion of variables centred at the singular point $\Upsilon = \{\xi_1^0,\xi_2^0\}^T$.

E.1 Variables expansion

The regularisation of the hypersingular kernel $G_{lj}^{m\ell}$ requires the Taylor's expansion of the kernel terms around $\Upsilon = \{\xi_1^0, \xi_2^0\}^T$. In this case, the expansions of $x_i - y_i$, r^n and $r_{,i}$ in the parameterised space ρ,θ are of interest. Furthermore, it is possible to express the expansion $x_i - y_i$ as follows:

$$\begin{aligned} x_i - y_i = \Bigg[& \left.\frac{\partial x_i}{\partial \xi_1}\right|_{\xi=Y} (\xi_1 - \xi_1^0) + \left.\frac{\partial x_i}{\partial \xi_2}\right|_{\xi=Y} (\xi_2 - \xi_2^0) \\ & + \left.\frac{\partial^2 x_i}{\partial \xi_1^2}\right|_{\xi=Y} \frac{(\xi_1 - \xi_1^0)^2}{2} + \left.\frac{\partial^2 x_i}{\partial \xi_1 \partial \xi_2}\right|_{\xi=Y} (\xi_1 - \xi_1^0)(\xi_2 - \xi_2^0) + \left.\frac{\partial^2 x_i}{\partial \xi_2^2}\right|_{\xi=Y} \frac{(\xi_2 - \xi_2^0)^2}{2} \\ & + \ldots \end{aligned} \tag{E.1}$$

Besides, in polar coordinates, the expansion Eq. E.1 leads to:

$$x_i - y_i = \rho A_i(\theta) + \rho^2 B_i(\theta) + O(\rho^3) \tag{E.2}$$

where:

$$A_i(\theta) = \left[\left.\frac{\partial x_i}{\partial \xi_1}\right|_{\xi=Y} \cos(\theta) + \left.\frac{\partial x_i}{\partial \xi_2}\right|_{\xi=Y} \sin(\theta) \right]$$
$$B_i(\theta) = \left[\left.\frac{\partial^2 x_i}{\partial \xi_1^2}\right|_{\xi=Y} \frac{\cos^2(\theta)}{2} + \left.\frac{\partial^2 x_i}{\partial \xi_1 \partial \xi_2}\right|_{\xi=Y} \cos(\theta)\sin(\theta) + \left.\frac{\partial^2 x_i}{\partial \xi_2^2}\right|_{\xi=Y} \frac{\sin^2(\theta)}{2} \right] \tag{E.3}$$

The distance r can be expanded as follows:

$$r^n = \rho^n A^n + n\rho^{n+1} \frac{A_k B_k}{A^{2-n}} + O(\rho^{n+2}) \tag{E.4}$$

in which $A = \|A_i\|$, $A_k B_k$ indicates the inner product between the vectors defined in Eq.Eq. E.3. For $n = 1$, the derivative $r_{,i}$ can be expressed as follows:

$$r_{,i} = \frac{A_i}{A} + \rho \left(\frac{B_i}{A} - A_i \frac{A_k B_k}{A^3} \right) + O(\rho^2) \tag{E.5}$$

Finally, the expansion of Lagrangian basis functions N^α leads to:

$$N^\alpha = N_0^\alpha + \rho N_1^\alpha(\theta) + O(\rho^2) \tag{E.6}$$

where $N_0^\alpha = N^\alpha(s)$ is a constant and $N_1^\alpha(\theta)$ is a function of θ,

$$N_1^\alpha = \left.\frac{\partial N^\alpha}{\partial \xi_1}\right|_{\xi=Y} \cos(\theta) + \left.\frac{\partial N^\alpha}{\partial \xi_2}\right|_{\xi=Y} \sin(\theta) \tag{E.7}$$

E.2 Explicit values for G_1 and G_2 :

The regularisation of the hypersingular terms G_1 and G_2 requires the linear expansion of the following variables r^n , r_j N^α and η_k. Besides, G_{kij} j can be rewritten in polar coordinates as follows Eq.Eq. E.8:

$$G_{kij} J\rho = C_2 \frac{1}{r^3} \rho \left\{ E(\rho,\theta) + F(\rho,\theta) + D(\rho,\theta) + H(\rho,\theta) \right\} \tag{E.8}$$

where $C_2 = 1/8\pi\,(1-\upsilon)$ and the other terms are as follows:

$$\begin{aligned} E(\rho,\theta) &= (1-2\upsilon)\left(\delta_{mj}\delta_{l\ell} + \delta_{lj}\delta_{\ell m} - \delta_{ml}\delta_{\ell j}\right) \\ F(\rho,\theta) &= 3\,(1-2\upsilon)\left(\delta_{mj} r_{,l} r_{,\ell} + \delta_{lj} r_{,m} r_{,\ell} - \delta_{lm} r_{,j} r_{,\ell}\right) \\ D(\rho,\theta) &= -3\left(\delta_{\ell j} r_{,l} r_{,m} + \delta_{m\ell} r_{,j} r_{,l} + \delta_{\ell l} r_{,m} r_{,j}\right) \\ H(\rho,\theta) &= -15 r_{,l} r_{,j} r_{,m} r_{,\ell} \end{aligned} \tag{E.9}$$

For $n = 3$ in Eq.Eq. E.4 one has:

$$\begin{aligned}\frac{1}{r^3}\rho &= \left[\frac{1}{\rho^3 A^3} - \frac{3A_k B_k}{\rho^2 A^5} + O\left(\frac{1}{\rho}\right)\right]\rho \\ \frac{1}{r^3}\rho &= \frac{F\_2(\theta)}{\rho^2} + \frac{F\_1(\theta)}{\rho} + O(1)\end{aligned} \tag{E.10}$$

Then, the tensors E, F,D and H can be rewritten as follows:

$$\begin{aligned}E(\rho,\theta) &= \rho E_1(\theta) + O(\rho^2) \\ F(\rho,\theta) &= F_0(\theta) + \rho F_1(\theta) + O(\rho^2) \\ D(\rho,\theta) &= D_0(\theta) + \rho D_1(\theta) + O(\rho^2) \\ H(\rho,\theta) &= H_0(\theta) + \rho H_1(\theta) + O(\rho^2)\end{aligned} \tag{E.11}$$

where $E_1(\theta)$, $F_0(\theta)$, $F_1(\theta), D_0(\theta)$, $D_1(\theta)$, $H_0(\theta)$ and $H_1(\theta)$ are:

$$E_1(\theta) = (1-2\upsilon)\left(\delta_{mj}\delta_{l\ell} + \delta_{lj}\delta_{\ell m} - \delta_{ml}\delta_{\ell j}\right) \tag{E.12}$$

$$F_0(\theta) = 3(1-2\upsilon)\left(\delta_{mj}\frac{A_l A_\ell}{A^2} + \delta_{lj}\frac{A_m A_l}{A^2} + \delta_{lm}\frac{A_j A_\ell}{A^2}\right) \tag{E.13}$$

$$\begin{aligned}F_1(\theta) = 3(1-2\upsilon)\delta_{mj}&\left[\frac{A_l}{A}\left(B_\ell - \frac{A_\ell A_k B_k}{A^3}\right) + \frac{A_\ell}{A}\left(B_l - \frac{A_l A_k B_k}{A^3}\right)\right] \\ +\delta_{lj}&\left[\frac{A_\ell}{A}\left(B_m - \frac{A_m A_k B_k}{A^3}\right) + \frac{A_m}{A}\left(B_\ell - \frac{A_\ell A_k B_k}{A^3}\right)\right] \\ +\delta_{lm}&\left[\frac{A_j}{A}\left(B_\ell - \frac{A_\ell A_k B_k}{A^3}\right) + \frac{A_\ell}{A}\left(B_j - \frac{A_j A_k B_k}{A^3}\right)\right]\end{aligned} \tag{E.14}$$

$$D_0(\theta) = -3\left(\delta_{\ell j}\frac{A_l A_m}{A^2} + \delta_{m\ell}\frac{A_j A_l}{A^2} + \delta_{\ell l}\frac{A_m A_j}{A^2}\right) \tag{E.15}$$

$$\begin{aligned}D_1(\theta) = -3\Bigg(&\delta_{\ell j}\left[\frac{A_l}{A}\left(B_m - \frac{A_m A_k B_k}{A^3}\right) + \frac{A_m}{A}\left(B_l - \frac{A_l A_k B_k}{A^3}\right)\right] \\ &+\delta_{m\ell}\left[\frac{A_j}{A}\left(B_l - \frac{A_l A_k B_k}{A^3}\right) + \frac{A_l}{A}\left(B_j - \frac{A_j A_k B_k}{A^3}\right)\right] \\ &+\delta_{\ell l}\left[\frac{A_m}{A}\left(B_j - \frac{A_j A_k B_k}{A^3}\right) + \frac{A_j}{A}\left(B_n - \frac{A_m A_k B_k}{A^3}\right)\right]\end{aligned} \tag{E.16}$$

$$H_0(\theta) = -15\frac{A_l A_j A_m A_\ell}{A^4} \tag{E.17}$$

$$H_1(\theta) = -15\left\{\frac{A_l A_j A_m}{A^3}\left(\frac{B_\ell}{A} - \frac{B_\ell A_k B_k}{A^3}\right) + \frac{A_l A_j A_\ell}{A^3}\left(\frac{B_m}{A} - \frac{B_m A_k B_k}{A^3}\right)\right.$$
$$\left. + \frac{A_l A_m A_\ell}{A^3}\left(\frac{B_j}{A} - \frac{B_j A_k B_k}{A^3}\right) + \frac{A_j A_m A_\ell}{A^3}\left(\frac{B_i}{A} - \frac{B_i A_k B_k}{A^3}\right)\right. \tag{E.18}$$

Furthermore, the term $G_{lj}^{m\ell} J\rho$ results in:

$$G_{lj}^{m\ell} J\rho = C_3\left(\frac{F\_2}{\rho^2} + \frac{F\_1}{\rho} + O(1)\right)\left[(F_0 + D_0 + H_0) + (E_1 + F_1 + D_1 + H_1)\,\rho + O(\rho^2)\right]$$
$$G_{lj}^{m\ell} J\rho = \left(\frac{F\_2}{\rho^2} + \frac{F\_1}{\rho} + O(1)\right)\left[S_0 + S_1\rho + O(\rho^2)\right]$$
$$G_{lj}^{m\ell} J\rho = \left(\frac{F\_2 S_0}{\rho^2} + \frac{(F\_2 S_1 + F\_1 S_0)}{\rho} + O(1)\right) \tag{E.19}$$

where $S_0(\theta) = F_0(\theta) + D_0(\theta) + H_0(\theta)$ e $S_1(\theta) = E_1(\theta) + F_1(\theta) + D_1(\theta) + H_1(\theta)$. Because $N = N_0 + \rho N_1 + O(\rho^2)$, $G_{lj}^{m\ell} J\rho$ can be expressed in polar coordinates as follows:

$$G_{lj}^{m\ell} J\rho = C_3\left(\frac{F\_2}{\rho^2} + \frac{F\_1}{\rho} + O(1)\right)\left[(F_0 + D_0 + H_0) + (E_1 + F_1 + D_1 + H_1)\,\rho + O(\rho^2)\right]$$
$$G_{lj}^{m\ell} J\rho = \left(\frac{F\_2}{\rho^2} + \frac{F\_1}{\rho} + O(1)\right)\left[S_0 + S_1\rho + O(\rho^2)\right]$$
$$G_{lj}^{m\ell} J\rho = \left(\frac{F\_2 S_0}{\rho^2} + \frac{(F\_2 S_1 + F\_1 S_0)}{\rho} + O(1)\right) \tag{E.20}$$

Finally, the terms $R\_2(\theta)$ and $R\_1(\theta)$ can be expressed explicitly as follows:

$$R\_2(\theta) = C_3 F\_2(\theta) S_0(\theta) \otimes N_0$$
$$R\_1(\theta) = C_3\left[(F\_2(\theta) S_1(\theta) + F\_1(\theta) S_0(\theta)) \otimes N_0 + F\_2(\theta) S_0(\theta) \otimes N_1(\theta)\right] \tag{E.21}$$